CHARACTERIZATION OF AMINO ACID AND PEPTIDE RADICALS AND RADICAL CATIONS AND THEIR USE AS PROBES FOR THE AQUEOUS MICROENVIRONMENT

Ryan Coleman White

A dissertation submitted to the faculty of the University of North Carolina at Chapel Hill in partial fulfillment of the requirements of the degree of Doctor of Philosophy in the Department of Chemistry.

Chapel Hill

2006

Approved by:

Malcolm D. E. Forbes

Marcey L. Waters

Maurice S. Brookhart

ABSTRACT

Ryan Coleman White

Characterization of Amino Acid and Peptide Radicals and Radical Cations and Their Use as Probes for the Aqueous Microenvironment
(Under the Direction of Malcolm D. E. Forbes)

Amino acid radicals and radical cations formed through oxidation are characterized by Time-resolved Electron Paramagnetic Resonance (TREPR) spectroscopy. These oxidation processes occur through single-electron transfer events to excited triplet state anthraquinone photo-sensitizers, and by hydrogen atom transfer to hydroxyl radicals created in situ. The identity of the radicals formed by electron transfer is strongly dependent on the pH of the solution. In particular, a previously hypothesized cyclic methionine radical cation structure is directly observed on the sub-microsecond timescale. The uncharged carbon radicals formed by hydroxyl attack in oxygenated environments are found to form peroxyl adducts with molecular oxygen. The structures of these radicals are deduced by computer simulation of magnetic parameters. The radical intermediates created upon oxidation of diglycine by anthraquinone photosensitizers are used as probes for microscopic water pools formed in reverse micelles. A new "micro-reactor" model is used to simulate the chemically induced dynamic electron polarization of the TREPR radical signals. Radical diffusion coefficients are generated from these simulations from which the viscosities of the water pools can be calculated. Also, radicals formed from direct oxidation of the reverse micelle surfactant are observed and characterized by TREPR, the products are analyzed by chemically induced dynamic nuclear polarization.

ACKNOWLEDGEMENTS

To Mom, Dad, Malcolm, Denise, Eddie, and Grandma Quinn, Thank You.

TABLE OF CONTENTS

Page

LIST OF TABLES AND GRAPHS viii

LIST OF FIGURES ix

LIST OF SCHEMES xii

LIST OF CHARTS xiii

LIST OF ABBREVIATIONS AND SYMBOLS xiv

I. INTRODUCTION 1

1.1 General Introduction 1

1.2 Experimental Overview of TREPR 5

1.3 CIDEP 7

1.4 Photo-sensitizers for TREPR 15

1.4.1 Anthraquinone Sulfonate Sodium Salts 15

1.4.2 Hydrogen Peroxide 17

II. METHIONINE RADICAL CATION 21

2.1 Introduction 22

2.2 Background 22

2.3 Results and Discussion 28

2.3.1 The pH Dependent Formation of Radicals from L-Methionine Analogs 28

2.3.2 The pH Dependent Formation of Radicals from N-acetyl-L-Methionine Analogs 36

2.3.3 Polarization Transfer to the Aminyl Radical 50

2.4 Conclusions and Outlook 59

2.5 Experimental 60

III. AMINO ACID AND PEPTIDE RADICALS FORMED BY ONE-ELECTRON OXIDATION 63

3.1 Introduction 64

3.2 Results and Discussion 66

3.2.1 pH Dependent Oxidation of N-acetylglycine and Diglycine Analogs 66

3.3 Conclusions 72

3.4 Experimental 72

IV. AMINO ACID AND PEPTIDE CARBON AND PEROXYL RADICALS FORMED BY H-ABSTRACTION BY HYDROXYL RADICAL… 75

4.1 Introduction 76

4.2 Results and Discussion 79

4.2.1 Studies of Carbon Radicals Formed in De-oxygenated Solutions 79

4.2.2 Studies of Peroxyl Radicals Formed in Oxygen Saturated Solutions 89

4.3 Conclusions 100

4.4 Experimental 100

V. PEPTIDE RADICALS AS PROBES FOR THE AQUEOUS MICROENVIRONMENT 103

5.1 Introduction 104

5.2 Background 105

5.3 Micro-reactor Model 109
5.4 Results and Discussion 112
5.4.1 Reverse Micelle Parameters 112
5.4.2 Time Dependence 113
5.4.3 AQS vs. AQDS 117
5.4.4 Reverse Micelle Size Dependence 120
5.4.5 Temperature Dependence 123
5.4.6 Simulation of TREPR Spectra and Extraction of D Values 123
5.5 Conclusions 129
5.6 Experimental 129
VI. TREPR AND CIDNP STUDIES OF THE OXIDATION OF AOT 131
6.1 Introduction 132
6.2 Results and Discussion 139
6.2.1 TREPR Spectra at Room Temperature 139
6.2.2 CIDNP Studies 145
6.2.3 Summary of Radical Structures 154
6.2.4 TREPR Time Dependence 156
6.2.5 Reverse Micelle Size Dependence 156
6.2.6 Temperature Dependence 161
6.3 Conclusions 162
6.4 Experimental 162
BIBLIOGRAPHY 165

LIST OF TABLES AND GRAPHS

Table 2.1: All observed Met^{+}• structures and magnetic parameters obtained from computer simulation.....30

Table 3.1: All observed glycine derivative radical structures and magnetic parameters obtained from computer simulation.....73

Table 4.1: Carbon-centered radicals and magnetic parameters obtained from computer simulation.....82

Table 4.2: Peroxyl adduct structures and magnetic parameters obtained from computer simulation.....94

Table 5.1: Diffusion coefficients in different Size RM's 127

Graph 5.1: Diffusion coefficients as a function of RM size 128

Table 6.1: Radicals formed from oxidation of AOT with magnetic parameters 153

LIST OF FIGURES

(all TREPR spectra are at X-band microwave frequency and shown with simulations unless otherwise noted)

Figure 1.1: Neurotoxicity in the presence of various Amyloid β peptides 3

Figure 1.2: TREPR timing sequence 8

Figure 1.3: Triplet Mechanism 9

Figure 1.4: Radical Pair Mechanism 11

Figure 1.5: CFN model of SCRP 14

Figure 2.1: Time dependence of X-band TREPR spectra taken after irradiation of AQS and L-methionine in aqueous solution at pH 2.0 29

Figure 2.2: pH dependence of TREPR spectra taken after irradiation of an aqueous solution of AQS and L-methionine 32

Figure 2.3: TREPR spectra taken after irradiation of AQS and L-methionine in H_2O and D_2O at high pH/pD 35

Figure 2.4: pH dependence of TREPR spectra taken after irradiation of an aqueous solution of AQS and NAM 39

Figure 2.5: TREPR spectra taken after irradiation of AQS and NAM in H_2O and D_2O at low pH/pD 40

Figure 2.6: TREPR spectra taken after irradiation of AQS and NAM in H_2O and D_2O at high pH/pD 43

Figure 2.7: High pH TREPR spectra taken after irradiation of AQS and A) NAM and B) NAM-d_3 in H_2O 44

Figure 2.8: Q-band TREPR spectra taken after irradiation of AQS and NAM in H_2O at different pH values 46

Figure 2.9: Aminyl radical spectrum with various TM/RPM simulations 52

Figure 2.10: X- and Q-band aminyl radical TREPR spectra 53

Figure 2.11: Polarization transfer and deprotonation of aminyl radical cation 56

Figure 2.12: TREPR spectrum and simulation for aminyl radical.....58

Figure 3.1: pH dependent TREPR spectra taken after irradiation of AQS and GG in H_2O.....67

Figure 3.2: High pH/pD TREPR spectra taken after irradiation of AQS and GG in H_2O and D_2O.....70

Figure 3.3: TREPR spectra taken after irradiation of solutions of NAG, NAG-^{13}C, NAG-d_3, and L-Ala-gly in the presence of AQS 71

Figure 4.1: TREPR spectrum taken after irradiation of H_2O_2 and GG in deoxygenated aqueous solution 80

Figure 4.2: Generation of observed spectrum from the superposition of spectra from 2 F-pairs 85

Figure 4.3: TREPR spectra taken after photolysis of H_2O_2 with alanine and valine in deoxygenated aqueous solution.....87

Figure 4.4: TREPR spectrum taken after photolysis of H_2O_2 with serine and threonine in deoxygenated aqueous solution 88

Figure 4.5: TREPR spectrum taken after photolysis of H_2O_2 with methionine in deoxygenated aqueous solution 91

Figure 4.6: TREPR spectra taken after photolysis of H_2O_2 with L-methionine-$^{13}C(2)$ and L-methionine-d_3 in deoxygenated aqueous solution 92

Figure 4.7: TREPR spectra taken upon photolysis of H_2O_2 with NAG and NAG-d_2 in oxygen-saturated aqueous solution.....95

Figure 4.8: TREPR spectra taken upon photolysis of H_2O_2 with serine and GG in oxygen-saturated solution aqueous solution 97

Figure 4.9: Time dependence of TREPR spectra taken upon irradiation of H_2O_2 and serine in oxygen-saturated solution.....99

Figure 5.1: Time dependent TREPR spectra taken upon irradiation of AQDS and GG inside an RM water pool 114

Figure 5.2: TREPR spectra taken after irradiation of AQDS/GG and AQS/GG inside an RM water pool 118

Figure 5.3: TREPR spectra taken after irradiation of AQDS/GG inside RM's of different sizes....122

Figure 5.4: TREPR spectra taken after irradiation of AQDS/GG inside of an RM obtained at different temperatures....124

Figure 5.5: Simulations obtained using the micro-reactor model for TREPR spectra taken after irradiation of AQDS/GG on the interior or RM's of different sizes....125

Figure 6.1: TREPR spectrum taken after irradiation of AQDS inside of a RM with an R_c = 30 Å....140

Figure 6.2: TREPR spectrum with same parameters as in Figure 6.1, with a 50 G sw and slower field sweep....141

Figure 6.3: Same as Figure 6.2, but with 20 G sw....143

Figure 6.4: NMR and CIDNP spectra taken before and after irradiation of AQDS inside of AOT RM's....147

Figure 6.5: CIDNP signals attributed to AOT reformation....151

Figure 6.6: TREPR spectrum and simulation of AOT radicals formed by oxidation by ^{3}AQDS*....155

Figure 6.7: Time dependent TREPR spectra taken after irradiation of AQDS inside AOT RM's....157

Figure 6.8: TREPR spectra taken after irradiation of AQDS inside of AOT RM's of different sizes....158

Figure 6.9: Temperature dependence of TREPR spectra taken after irradiation of AQDS in AOT RM's....160

LIST OF SCHEMES

Scheme 1.1: AQ(D)S photo-oxidation chemistry 16

Scheme 1.2: Photolysis of H_2O_2 to produce hydroxyl radicals and H-atom transfer from substrate 20

Scheme 2.1: One-electron oxidation of methionine and NAM 23

Scheme 2.2: Suggested one-electron oxidation pathways for methionine 25

Scheme 2.3: Simplified NAM one-electron oxidation reaction scheme at different pH values 38

Scheme 3.1: Possible one-electron oxidation pathways for NAG and GG 65

Scheme 4.1: General peroxylation mechanism of amino acid residues at the side-chain and backbone of peptides 78

Scheme 4.2: Formation of F-pairs from •OH and substrate 83

Scheme 4.3: Thermal oxidation of methionine by H_2O_2 and subsequent addition of hydroxyl radical 90

Scheme 4.4: Summary of peroxylation of NAG, serine, and diglycine 101

Scheme 5.1: Diagram of an AOT reverse micelle 106

Scheme 5.2: Oxidation of GG by AQDS to form α-amidomethylene radical 108

Scheme 5.3: Possible AOT radicals created upon oxidation by ^{3}AQDS* 119

Scheme 6.1: Possible oxidation and photolytic pathways of AOT 136

Scheme 6.2: Desulfonation of AOT 146

Scheme 6.3: Radical elimination from AOT radical to form alkene and oxo-acyl radical 150

LIST OF CHARTS

Chart 1.1: AQ(D)S radical structures at different pH values 19

Chart 2.1: Isotopically labeled cyclic radical cations formed from the oxidation of NAM analogs 42

Chart 2.2: R-N-H and R-S-N-H nitrogen hyperfine coupling constant comparison 51

Chart 2.3: Deprotonation of amine radical cation to aminyl radical 55

Chart 6.1: AOT and AQDS structures 133

LIST OF ABBREVIATIONS AND SYMBOLS

Abbreviations

A	absorptive TREPR transition
AOT	Aerosol OT
AQDS	2,6-anthraquinone disulfonate sodium salt
AQS	2-anthraquinone sulfonate sodium salt
APS	anti-phase structure
CIDEP	chemically induced dynamic electron polarization
CIDNP	chemically induced dynamic nuclear polarization
CW	continuous wave
E	emissive TREPR transition
E/A	combination of low field emissive and high field absorptive TREPR transitions
E/A*	combination of low field emissive and high field enhanced absorptive TREPR transitions
E*/A	combination of low field enhanced emissive and high field absorptive TREPR transitions
EPR	electron paramagnetic resonance
FT	Fourier transform
G	Gauss
GG	diglycine
ISC	intersystem crossing
MeOH	methanol
Met^{+}•	methionine radical cation
NAG	N-acetylglycine
NAG-d_3	N-acetyl-d_3-glycine
NAG-^{13}C	N-acetylglycine-^{13}C(2)
NAM	N-acetyl-L-methionine
NAM-d_3	N-acetyl-L-methionine-(methyl-d_3)
NMR	nuclear magnetic resonance
RM	reverse micelle
RP	radical pair
RPM	radical pair mechanism
SCRP	spin correlated radical pair (mechanism)
SDS	sodium dodecyl sulfate
S/N	signal to noise ratio
sw	sweep width
SSEPR	steady state electron paramagnetic resonance
TM	triplet mechanism
TREPR	time-resolved electron paramagnetic resonance
UV	ultraviolet

Symbols

a_H	hyperfine coupling constant
B_0	applied magnetic field
D	diffusion coefficient
g	isotropic electronic g-factor
Δg	difference in g-factors in a radical pair
h	Planck's constant
H	Hamiltonian operator
I	nuclear spin angular momentum operator
J	Heisenberg spin exchange parameter
J_0	J at r_0
k_b	Boltzmann constant
k_{re}	re-encounter rate constant
r_0	distance of closest approach of two radical centers
R_c	RM water pool radius
S	electron spin angular momentum operator
T_1	spin-lattice relaxation time
T_2	spin-spin relaxation time
β	Bohr magneton
λ	fall off parameter
ω_0	spectrometer frequency
Ψ	wave function
η	viscosity

CHAPTER I

INTRODUCTION

1.1 General Introduction

The oxidation of biologically relevant molecules such as proteins, DNA, and lipids has become an important topic of interest with regards to cellular function and disease. While the controlled oxidation of substrates occurs in a myriad of enzymatic processes and is necessary for life, uncontrolled oxidation can degrade these biological substrates, causing cellular malfunction and death. These uncontrolled oxidative processes are also thought to be the major pathways through which cells age. Of the three general classes of molecules listed above, proteins make up a vast majority of the cellular bulk (50-60 % of the dry weight of the cell,[1] and hence react the most often with oxidative species en vivo. To determine the origins of disease and aging it is important to understand the specific pathways of oxidation of proteins by all the various oxidants present within the cell.

The random oxidation events that occur with proteins often leads to aggregation or condensation of proteins that eventually lead to a number of serious disease states including Alzheimer's Disease,[2-4] as well as cataractogenesis[5] and glaucoma formation[6]. To investigate the root causes of these diseases, scientists have focused in on side- and main-chain oxidation of individual amino acid residues. For example, there is considerable evidence linking the oxidation of a single methionine-35 residue on the αβ-amyloid protein located in human brain cells to the formation of Alzheimer 's disease plaques. Figure 1.1 shows cell toxicity studies performed by Varadarajan et al.[7] in which the Met-35 residue was replaced in the protein sequence by structurally similar norleucine or valine via site directed mutagenesis. It shows that in the native full sequence protein Aβ(1-40) and protein fragments Aβ(25-35) containing Met-35, the levels of neuronal survival are much less than in the Aβ(1-40)M35Nle or Aβ(1-40)M35V analogs. While these studies implicate the

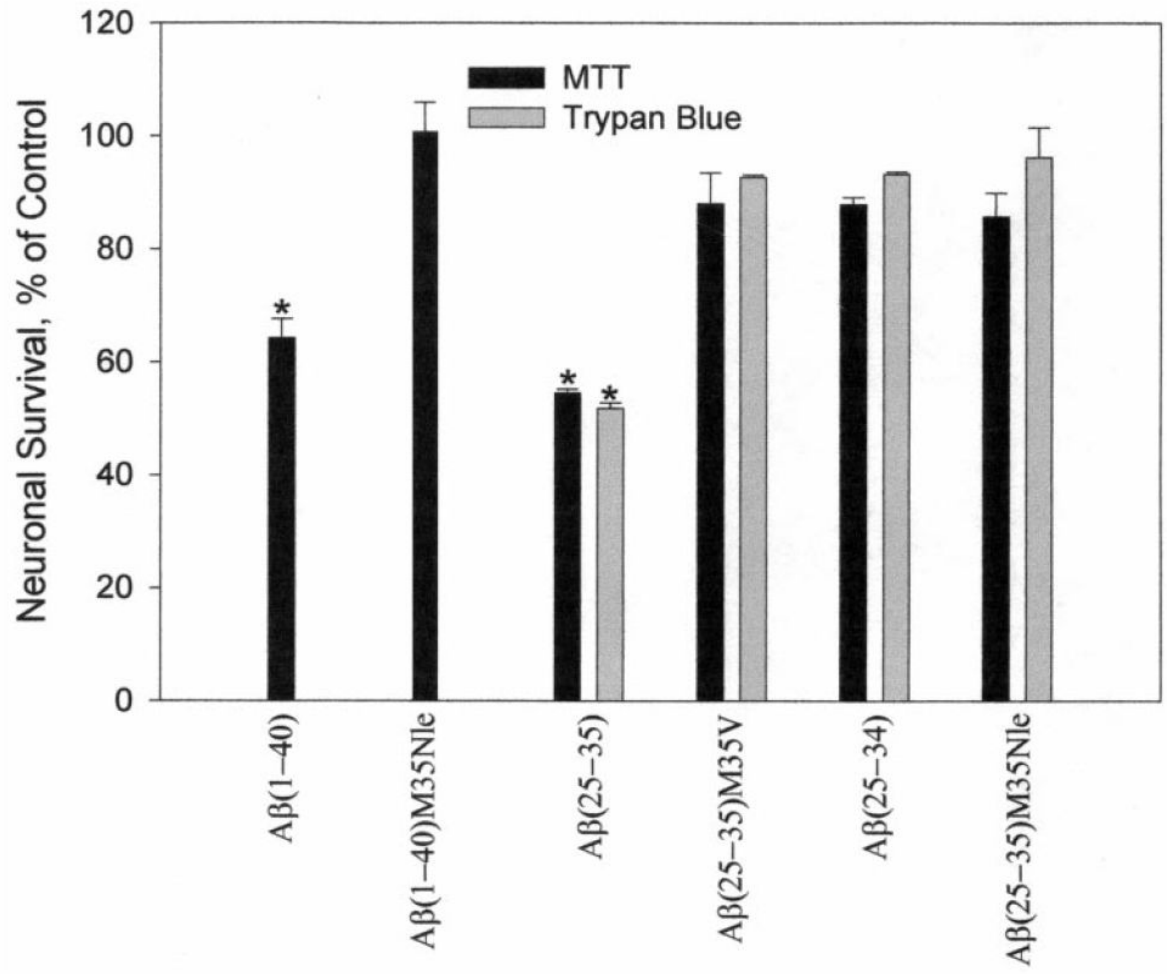

Figure 1.1: Neurotoxicity in the presence of various Amyloid β peptides. (Figure taken directly from reference #2.)

methionine residue as a key player in the mechanism of plaque formation, the primary chemical steps that occur are not known. In addition to protein aggregation, oxidative chemical reactions can lead to protein degradation[8] and loss of enzymatic activity and structure[9].

To understand the exact mechanisms of protein oxidation, extensive studies have been performed on smaller peptides, and amino acid model systems. Kinetics of these types of reactions have been investigated using pulse radiolysis and transient absorption techniques. As these types of reactions occur initially through radical intermediates, electron paramagnetic resonance (EPR) has yielded excellent structural information allowing for characterization of these species. Product analysis is also a useful tool by which to infer the exact mechanisms of oxidation.

While these experiments yield a wealth of information on radical reaction kinetics, radical structure, and products, there are some inherent drawbacks to these techniques that should be noted. For instance, due to the low resolution of transient optical spectra it is often difficult to link the broad featureless signals precisely to a unique intermediate. Although Steady-state EPR (SSEPR) techniques can be used to observe steady-state concentrations of radicals, the slow time response of the experiment (> 40 μs) means that any primary radicals that may be formed are undetectable. Product analysis also does not give direct evidence for the primary oxidation steps that occur in radical reactions.

Often described as a cross between laser flash photolysis and EPR, Time-resolved EPR (TREPR)[10] has been developed to observe radicals on the sub-microsecond timescale. This experiment allows for the observation of amino acid radical substrates that have previously been unobservable by previous methods. In addition to structural information that

can be obtained by analysis of the hyperfine splitting patterns, the phase and intensities of TREPR transitions give important information about radical precursors that aid in the elucidation of mechanism.

This dissertation describes the utilization of TREPR to structurally characterize the radicals and radical cations created upon oxidation of amino acids and peptides by both triplet photo-sensitizers and hydroxyl radicals in aqueous solution. The radical species presented here have not been previously observed and provide insight into key mechanisms of oxidation of biologically relevant species. To mimic the enclosed cellular environment, these reactions have also been used to generate radical ions within the aqeuous interior of reverse micelles (RM). By using the micro-reactor model to simulate the TREPR spectra taken upon photooxidation of these species in these water pools, information about radical diffusion can be obtained. This RM project represents the convergence of two different areas of EPR research: the photooxidation of amino acids and peptides and diffusion of radical pairs. Over the course of these investigations of oxidation in the interior of RM's it was also found that considerable photo-oxidation of the surfactant occurs. The resulting radicals are characterized here for the first time using both TREPR and the use of chemically induced dynamic nuclear polarization (CIDNP).

1.2 Experimental Overview of TREPR

Over the past 60 years, SSEPR has arisen as the most popular way to unambiguously characterize radical structure. The spectral transitions observed in EPR for unpaired electrons are directly analogous to nuclear magnetic resonance (NMR) for spin active protons. Like protons, electrons have a total spin value of S = ½, or two spin states, α and β.

When unpaired electrons are put in an external magnetic field B_0, the β spin state goes down in energy while the α state energy increases. The difference in energy between the two states is known as the Zeeman splitting. The absolute position of the signal with respect to the B_0 field is deterimined by the radical's g-factor (analogous to the chemical shift for NMR). While the g-factor is unique to each different radical, it is approximately 2.0030 for most organic radicals. Like the J coupling in NMR, the electron can couple to other near-by spin active nuclei via hyperfine coupling. It does this via hyperfine coupling. The magnitude of the hyperfine interactions (a_H) vary according to nucleus type and proximity to the unpaired electron. They are extrememly useful in determining radical structure. To generate spin transitions, excitation with microwave frequency, normally ~ 9.5 GHz (known as X-band), electromagnetic radiation is supplied by a microwave generator into a resonant cavity in which the sample is placed. In SSEPR, a 100 kHz magnetic field modulation is used to lock in the microwave frequency. While this greatly increases the signal to noise ratio (S/N), it limits the time resolution of these types of experiments to > 40 μs. The TREPR experiment does not utilize this field modulation, and therefore benefits from much faster time response (up to 60 ns). Without field modulation the signal to noise ratio (S/N) is lower in comparison to SSEPR techniques. However, this is compensated for by chemically induced dynamic electron polarization (CIDEP) mechanisms that populate spin states with non-Boltzmann distributions. This means that TREPR transitions can be both absorptive and emissive. These polarization mechanisms will be elaborated upon in the next section. On a fast timescale, there is also an appreciable difference from SSEPR spectra. Smaller hyperfine splittings (< 2 G) are often unobservable at short time delays (< 1 μs) to uncertainty

broadening on timescales faster than the Larmour frequency of the nucleus. Only after this time delay can hyperfine couplings below this limit be resolved.

In the continuous wave (CW) TREPR experiment, radicals are initially created by a pulse of UV laser light of 5 to 20 ns in duration. The TREPR signal is detected using a gated boxcar signal averager. The boxcar samples the signal from the microwave bridge before (dark gate) and after (light gate) the laser flash, then subtracts the two signals and then outputs the difference to the computer (see Figure 1.2). The width of the two gates are normally 100-300 ns depending on the desired time resolution. Additionally, the radical time profile can be collected at each field point during the sweep, and then the field dependent spectrum can be constructed afterwards.

Unlike other magnetic resonance techniqes such as NMR or SSEPR, the signals observed via TREPR do not represent a normal Boltzmann distribution of spin states induced by the magnetic field, and are therefore not always absorptive. Rather, the TREPR signals can have both emissive and absorptive character due to non-Boltzmann population of spin states created by CIDEP mechanisms which will be described in further detail in the next section.

1.3 CIDEP

There are three well established CIDEP mechanisms that will be important to the interpretation of the spectra presented in this thesis: 1) Triplet Mechanism[11] (TM), 2) Radical Pair Mechanism[12] (RPM), and 3) Spin-Correlated Radical Pair Mechanism[13] (SCRP). A qualitative description of the TM spin polarization process is depicted in Figure 1.3. For unsymmetric molecules, in the molecular frame, spin orbit coupling (the intersystem crossing

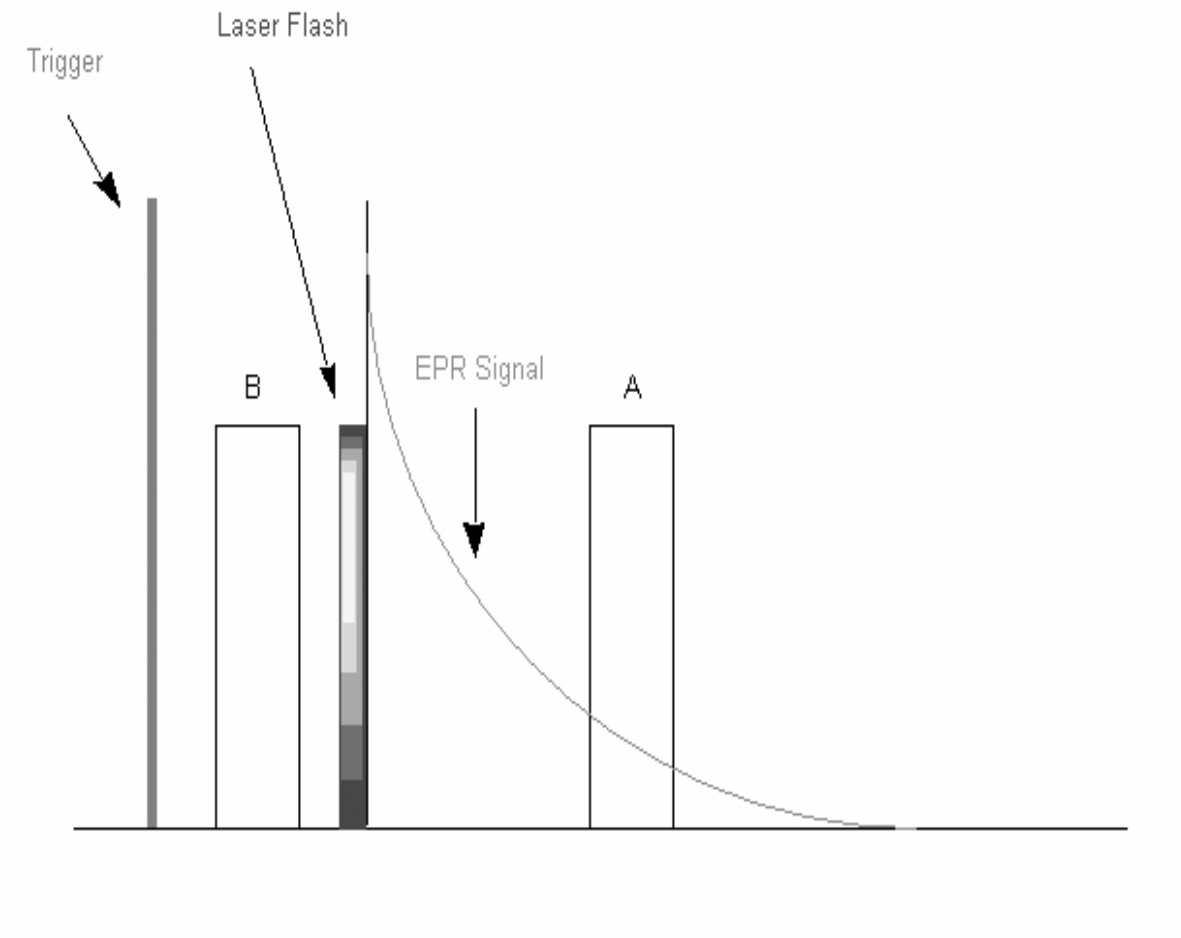

Figure 1.2: TREPR experiment timing sequence. B: Dark Gate A: Light Gate

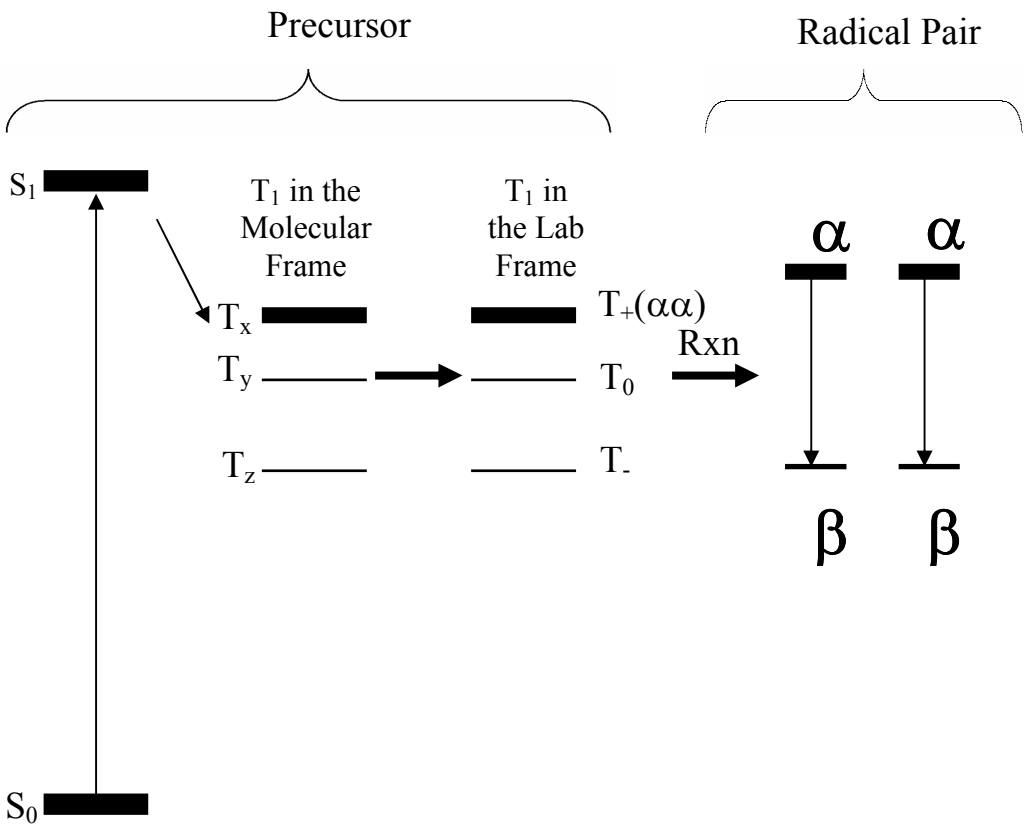

Figure 1.3: The Triplet Mechanism

process (ISC)) is anisotropic, and the result is preferential population of the zero-field triplet states. This polarization is transferred to the laboratory frame ($T_-(\beta\beta)$, $T_+(\alpha\alpha)$, and $T_0((\alpha\beta + \beta\alpha)/\sqrt{2})$ spin states), and then to the product radicals. In Figure 1.3, for example, the $T_-(\alpha\alpha)$ state is selectively populated. It generates radicals in the α spin state and therefore emissive TREPR transitions are observed. In general, TM can generate net emissive (E) or net absorptive (A) transitions depending on the symmetry of the triplet precursor (the sign of the zero field splitting) and the solvent environment. Viscous sovents tend to favor the production of TM polarization as it allows more distinction between T_x, T_y, and T_z during ISC.

The RPM polarization is generated by S-T_0 mixing as the radicals re-encounter in solution. Initially upon creation, radicals are close together and the magnitude of the Heisenberg spin exchange interaction (J) is high. The two unpaired electrons undergo spin exchange, or J coupling, and are essentially locked into either a singlet ($(\alpha\beta-\beta\alpha)/\sqrt{2}$) or T_0 spin state. The magnitude of this J coupling is dependent upon inter-radical distance. Figure 1.4 shows a qualitative picture of the distance dependence of J. As the radicals diffuse apart, the value of J diminishes, and the mixing of spin states based on g-factor and hyperfine coupling differences occurs. As the radicals re-approach and diffuse apart continously, the S-T_0 mixing process effectively depletes the population of a given spin state. As the radicals diffuse towards infinite dilution, the result is an over- or under-population of spin states that are detected. For a two radicals (R_1 and R_2) ($g_{R1} > g_{R2}$) generated from a triplet precursor, R_1 will E and while the R_2 transitions will be A. For radicals generated from a singlet precursor, the situation is reversed. This model applies to radicals that have, at the time of

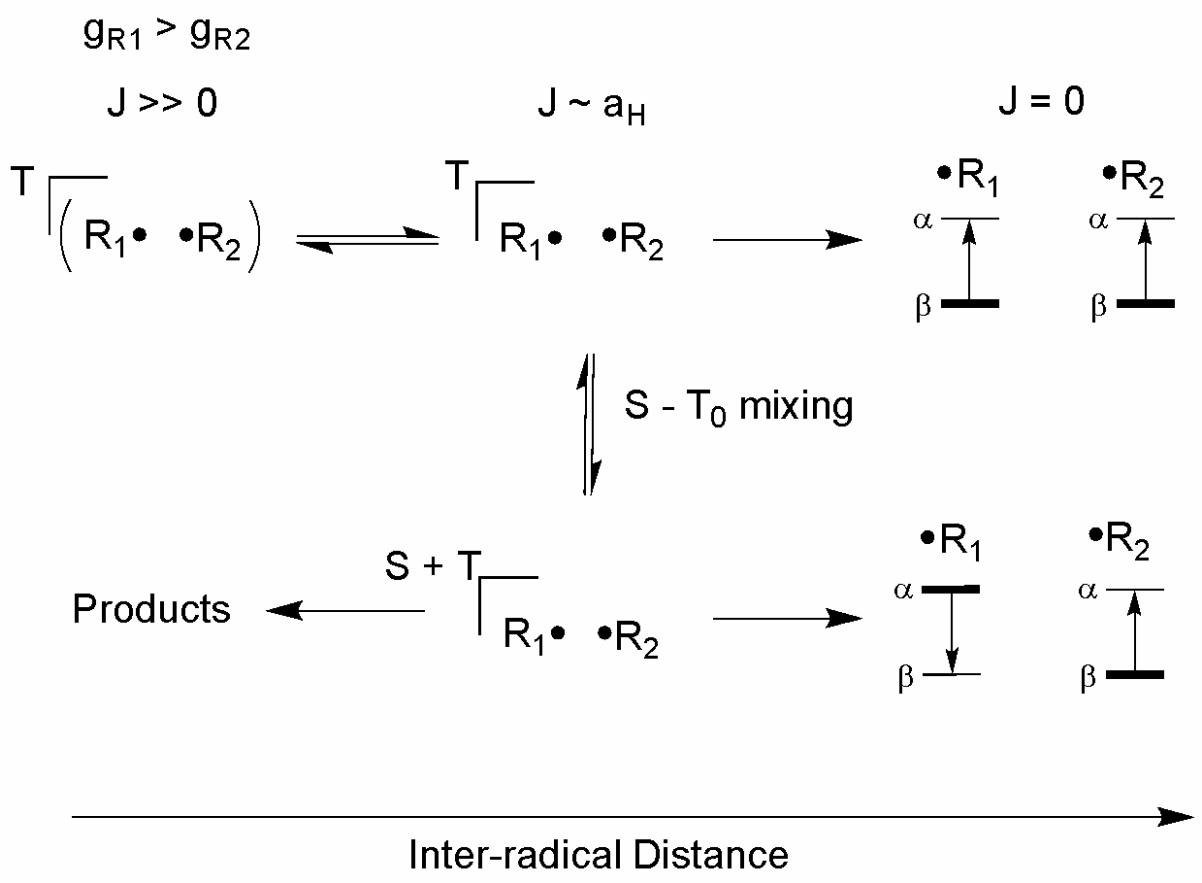

Figure 1.4: The Radical Pair Mechanism

spectroscopic observation, already diffused far enough away so that they can be considered true doublet states where J = 0.

If the radicals are observed while $J \neq 0$ this S-T_0 mixing process results in a different polarization mechanism known as SCRP. SCRP occurs when radicals are confined to a limited space in which the spin states of the radical pair are described in the triplet basis. This theory was first presented by Closs et al.[13] to explain the spectra generated from radicals confined within sodium dodecyl sulfate (SDS) micelles and non-conjugated biradicals connected with alkyl chain tethers. Figure 1.5 qualitatively outlines the process by which the spin levels are populated. As applied to the molecular systems described in this dissertation, the radical pair is intially generated from a triplet state precursor, thereby populating the T_+, T_-, and T_0 levels equally while leaving the singlet state unpopulated. At distances in which J ~ a_H or Δg, S-T_0 mixing occurs in which new wavefunctions, Ψ_2 and Ψ_3, are created. The Ψ_2 and Ψ_3 develop directly from the S and T_0 states, respectively. These new wave functions get depopulated by chemical reaction to form diamagnetic products resulting in a greater spin population in the T_+ and T_- states. The spectral transitions for such a radical pair are shown in Figure 1.5 and are known as anti-phase structure (APS). The appropriate Spin Hamiltonian for this 2 spin system is shown in equation 1.1.

$$H = \frac{h}{2\pi}\beta B_0(g_1\mathbf{S_{1z}} + g_2\mathbf{S_{2z}}) - J(\frac{1}{2} + \mathbf{S_{1z}}\cdot\mathbf{S_{2z}}) + \sum_i a_{1i}\cdot\mathbf{S_{1z}}\cdot\mathbf{I_{1i}} + \sum_j a_{2j}\cdot\mathbf{S_{2z}}\cdot\mathbf{I_{2j}} \qquad (1.1)$$

The bold symbols refer to the spin angular momentum operators (**S** for electrons, **I** for nuclei). The first term is the Zeeman interaction. The second term represents the electronic spin-spin coupling between the unpaired spins and is written to produce a splitting of -2J

between the singlet and triplet levels at zero applied magnetic field. The third term represents the electron-nuclear hyperfine interactions. As seen in Figure 1.5, each line that would correspond to the single transition attributed to the mono-radical turns into an E/A or A/E doublet dependent on whether J is positive or negative, respectively. In recent years, there have been improvements to SCRP theory with regard to diffusion and the distance dependence of J. This will be discussed in more detail in Chapter 5 as a means to simulate TREPR data acquired for radical pairs in reverse micelles (RM).

The phases of transitions are determined by the CIDEP mechanism, which is in turn dependent on the identity of the radical pair (RP). Once a RP is produced, three different processes can occur. A singlet born RP can recombine to form diamagnetic products. If the RP has triplet character, recombination is not allowed and the radicals are considered a geminate pair. On the timescale of the TREPR experiment, geminate RP's are only observed in very special situations, like inside of micro-environments. In bulk solution, after ~1 ns the geminate radicals have escaped and diffused completely away from each other. The radicals are then free to interact with other radicals in solution, to form Free or Random Pairs (F-pairs). Geminate radicals with triplet character are most likely to escape to form F-pairs. Therefore, the F-pairs are formed with a majority of triplet character. The radicals observed by TREPR will be polarized by RPM and will exhibit E/A character. This concept will be expanded upon further in Chapter 4 when H_2O_2 is used as a radical precursor.

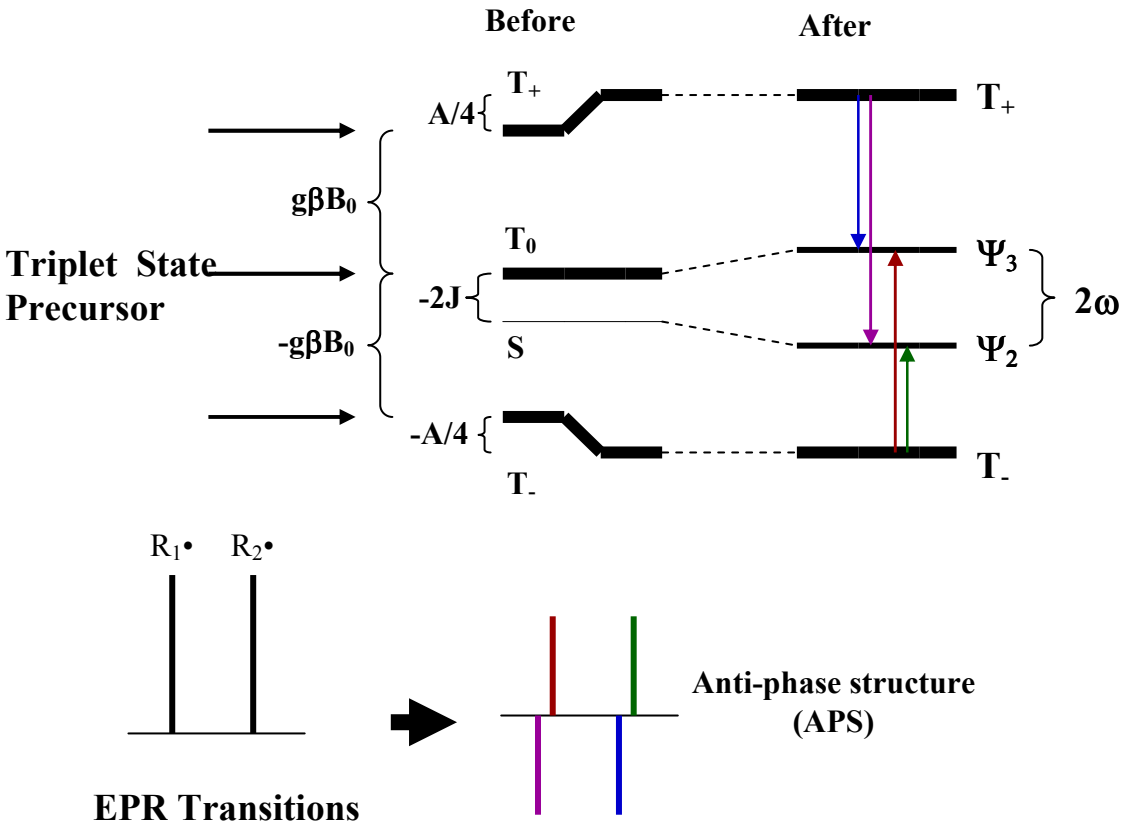

Figure 1.5: The CFN Model of SCRP

1.4 Photo-sensitizers for TREPR

1.4.1 Anthraquinone Sulfonate Salts

In this dissertation, water-soluble anthraquinone sulfonate salts, anthraquinone-2-sulfonate (AQS) and anthraquinone-2,6-disulfonate (AQDS) are the main photo-sensitizers that are utilized for the production of spin polarized radicals and radical cations. These anthraquinone species allow for the production of these radicals in high yield in aqueous solutions over a wide pH range. Excitation of AQ(D)S at 308 nm (XeCl excimer laser) leads cleanly and quickly to triplet excited states which are quenched by good electron donors. AQS and AQDS are excellent sensitizers for this chemistry, with a high extinction coefficient at 308 nm, a high quantum yield for formation of the triplet, and both triplet states are excellent electron acceptors.[14] Scheme 1.1 shows the structures of AQ(D)S as well as the general oxidation scheme observed. Photo-excited anthraquinones also produce intense triplet mechanism spin polarization[15] in the inter–system crossing process, which leads to good signal-to-noise ratios in our experiment (as discussed above). An additional advantage of these sensitizers is that their radical anions $AQS^{-}\bullet$, and $AQDS^{-}\bullet$, have very small hyperfine couplings and in almost all of our experiments appears as a single sharp line. Therefore these radicals do not interfere or overlap very much with signals from radicals whose structural characterization is desired.

The AQ(D)S photochemistry is occuring in aqueous solution and the effect of solution pH on these photosensitizers deserves comment. In low pH solutions the $AQS^{-}\bullet$ radical anion is expected to be protonated rapidly to form the AQSH•, and AQDSH• radicals. This is based on the fact that the pK_a of the conjugate acid of the closed shell anion is 3.9,[16,17] and the assumption that the conjugate acid of the open shell radical ion should have

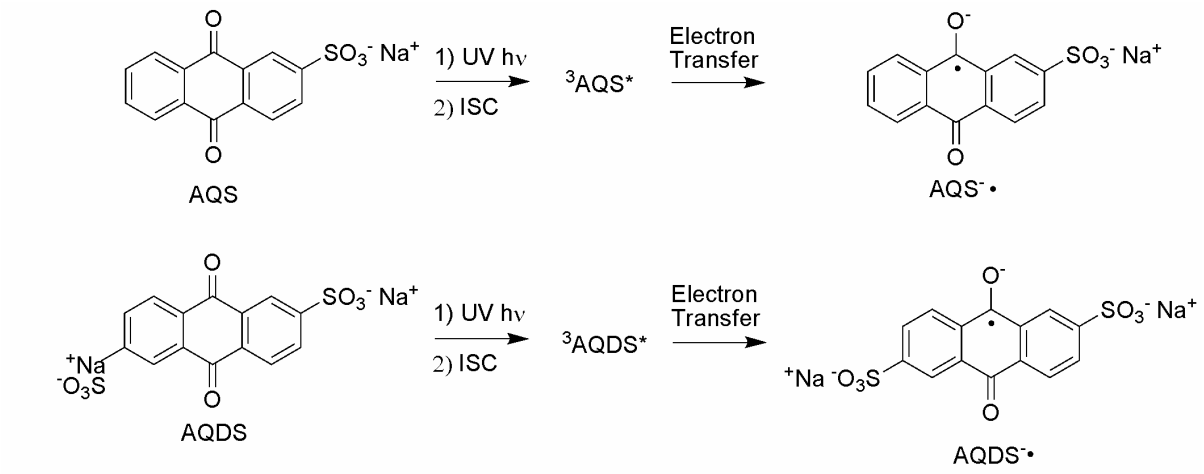

Scheme 1.1: AQ(D)S photo-oxidation chemistry

approximately the same acidity. If anything it should even be more acidic as it is more electron deficient as an open shell molecule. The neutral AQSH• radical is also strongly polarized by the triplet mechanism and has a very narrow spectral width, although it is broader than the AQS^{-}• signal due to a small hyperfine coupling to the extra H atom. For this reason it appears as a narrow, sharp doublet in our experiments (at least at later delay times, *vide infra*), and slightly upfield from AQS^{-}• due to its smaller g-factor. The AQ(D)S-• radicals, along with their conjugate acids, are shown in Chart 1.1.

1.4.2 Hydrogen Peroxide

In order to create product radicals through H-abstraction processes, hydroxyl radicals are used as precursors. Hydroxyl radicals have been shown to be very reactive and to oxidize substrates unselectively with near diffusional rate constants.[18] The most convenient method for the creation of hydroxyl radicals is the direct photolysis of hydrogen peroxide. The general mechanism for this process is shown in Scheme 1.2. While the extinction coefficient of H_2O_2 at UV wavelengths is very low, this reaction creates 2 equivalents of hydroxyl radicals per photon absorbed. Hydroxyl radicals are EPR silent due to extremely fast spin relaxation from spin rotation interaction. This means that only the counter-radicals are observed spectroscopically without signal overlap. Hydroxyl radicals are formed directly from cleavage of $^{1}H_2O_2$* and therefore do not transfer any TM polarization over to the radical products. However, RPM spin polarization occurs from F-pairs formed in solution, thereby generating the necessary polarization to observe the product radicals. Unlike normal RPM emissive/absorptive (E/A) spectral patterns, hydroxyl radical spectra generate emissive/enhanced absorptive (E/A*) signal patterns. This process is discussed briefly in the

the previous section and will be focused on in detail in Chapter 4. The polarization generated from this radical chemistry enables us to observe oxygen adduct product radicals that will be discussed further in Chapter 4.

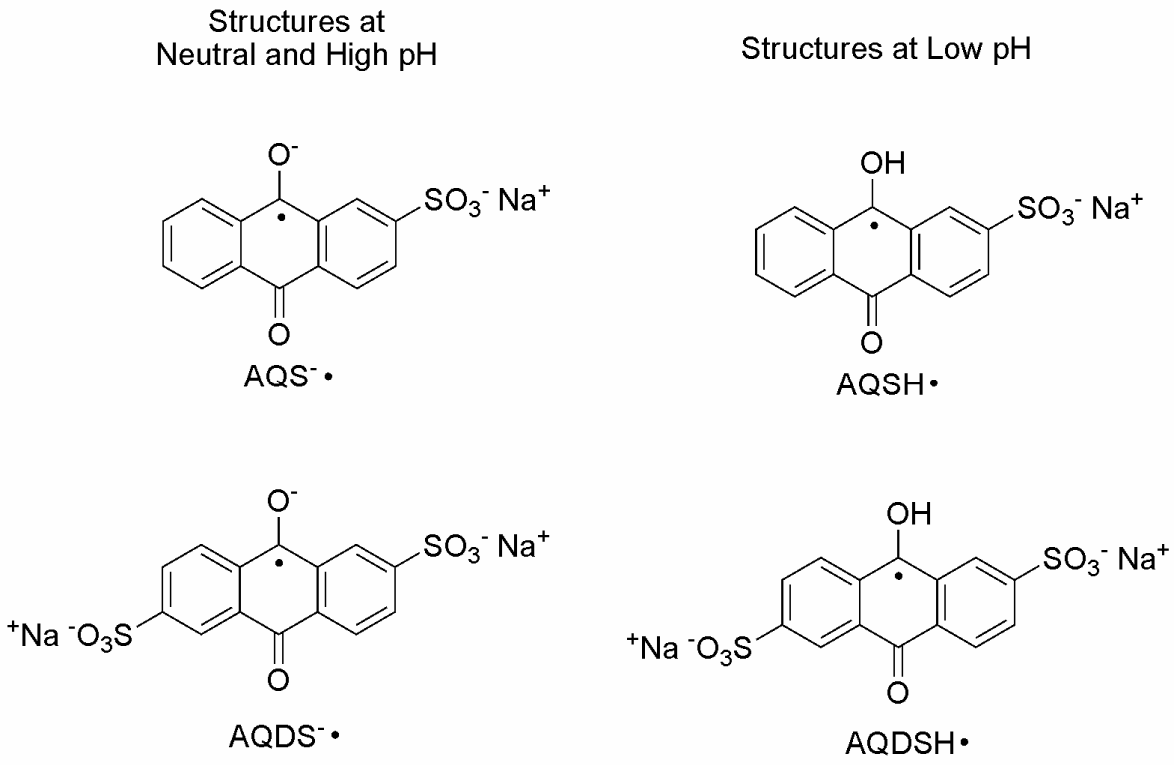

Chart 1.1: AQ(D)S radical structures at different pH values

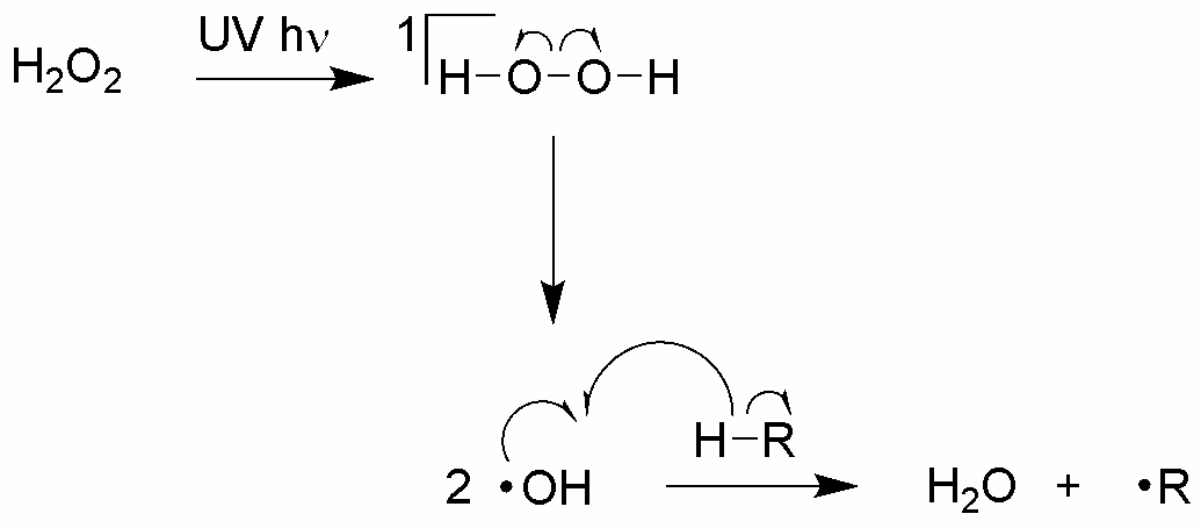

Scheme 1.2: Photolysis of H_2O_2 to produce hydroxyl radicals and H-abstraction from substrate

CHAPTER II

METHIONINE RADICAL CATION

2.1 Introduction

Amino acid side chain redox chemistry and free radical chemistry are critical to many biological reaction mechanisms,[5] and a detailed characterization of the reactive intermediates involved is highly desirable. The process of oxidation at sulfur in methionine to give a radical cation (**2.1**, Scheme 2.1, top), has been implicated in several important biochemical reaction pathways, notably glycation of proteins and subsequent disease development such as glaucoma.[6] The redox chemistry of methionine within proteins is currently a topic of great interest. Much of this attention stems from the fact that oxidation of methionine has been directly linked to amyloid fibril formation in neurological biochemistry. This process is suspected to be the first in a cascade of many chemical reactions leading to symptoms of Alzheimer's disease.[2-4]

2.2 Background

Methionine radical cation is therefore a paramagnetic reactive intermediate of great importance, whose structure and reactivity need to be clearly understood. The cation itself and several model systems have been investigated indirectly by several different physical methods in solution, and in glassy matrices or single crystals by electron paramagnetic resonance (EPR) spectroscopy. However, high resolution EPR characterization of **2.1** and its N-acetylmethionine derivative (**2.2**, Scheme 2.1, bottom right) in aqueous solution has not been reported to date. Our research groups have had a long-standing interest in the redox chemistry of amino acids[19] and short peptides,[20,21] and in this paper we turn our attention to the radical chemistry of methionine as a function of pH at room temperature.

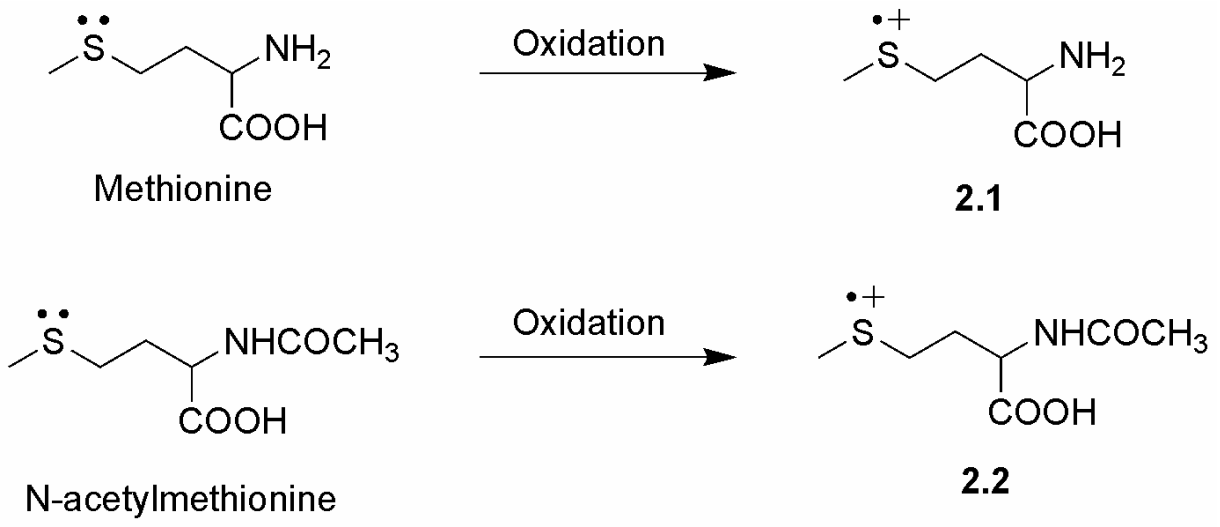

Scheme 2.1: One-electron oxidation of methionine and NAM

Scheme 2.2 shows the spectrum of reactivity that has been proposed in the literature during the past 30 years for cations such as **2.1**. The first magnetic resonance spectra of such cations were recorded by Kominami[22] and Kawatsura, et al.,[23] who reported EPR parameters from γ–irradiated single crystals of DL–methionine. Along with Naito et al.'s EPR work on ^{33}S substituted methionine in 1977,[24] these early papers clearly established that oxidation occurs preferentially at sulfur. Later, pulse radiolysis experiments by Asmus et al.,[25] along with further work by Naito and coworkers,[26] provided evidence for dimeric structures such as **2.5a** containing S–S three electron bonds, as well as neighboring group effects with heteroatoms such as nitrogen and oxygen. Such neighboring group effects led these researchers to postulate 6– and 5–membered ring intermediate structures with S–O and S–N three electron bonds (e.g. **2.6** and **2.7** in Scheme 2.2), whose formation was dependent on the pH of the solution. Bobrowski and coworkers have done extensive studies of the oxidation chemistry of methionine and have proposed similar cyclic structures,[27] as well as the possibility that hydroxyl radical, at pH > 10, can assist decarboxylation of the radical cation in certain short peptide sequences.[28] In the case of a single methionine molecule the decarboxylation reaction would lead to an α–amino radical such as **2.8**. There is also some evidence for the existence of hydroxy sulfuranyl radicals (e.g. **2.9**) in the solution chemistry of this amino acid.[29] The majority of the early literature reports on this topic have provided at least circumstantial evidence for the dimeric S–S bonded structure **2.5a** at pH < 7 and the 5–membered ring S–N bonded structure **2.7a** at pH > 10.

The low temperature steady–state EPR experiments of Champagne et al. showed that the cyclic structure **2.7a** is formed in the solid state.[30] Their data lacked the resolution available in liquid solution experiments, and for this reason their g–factor measurements

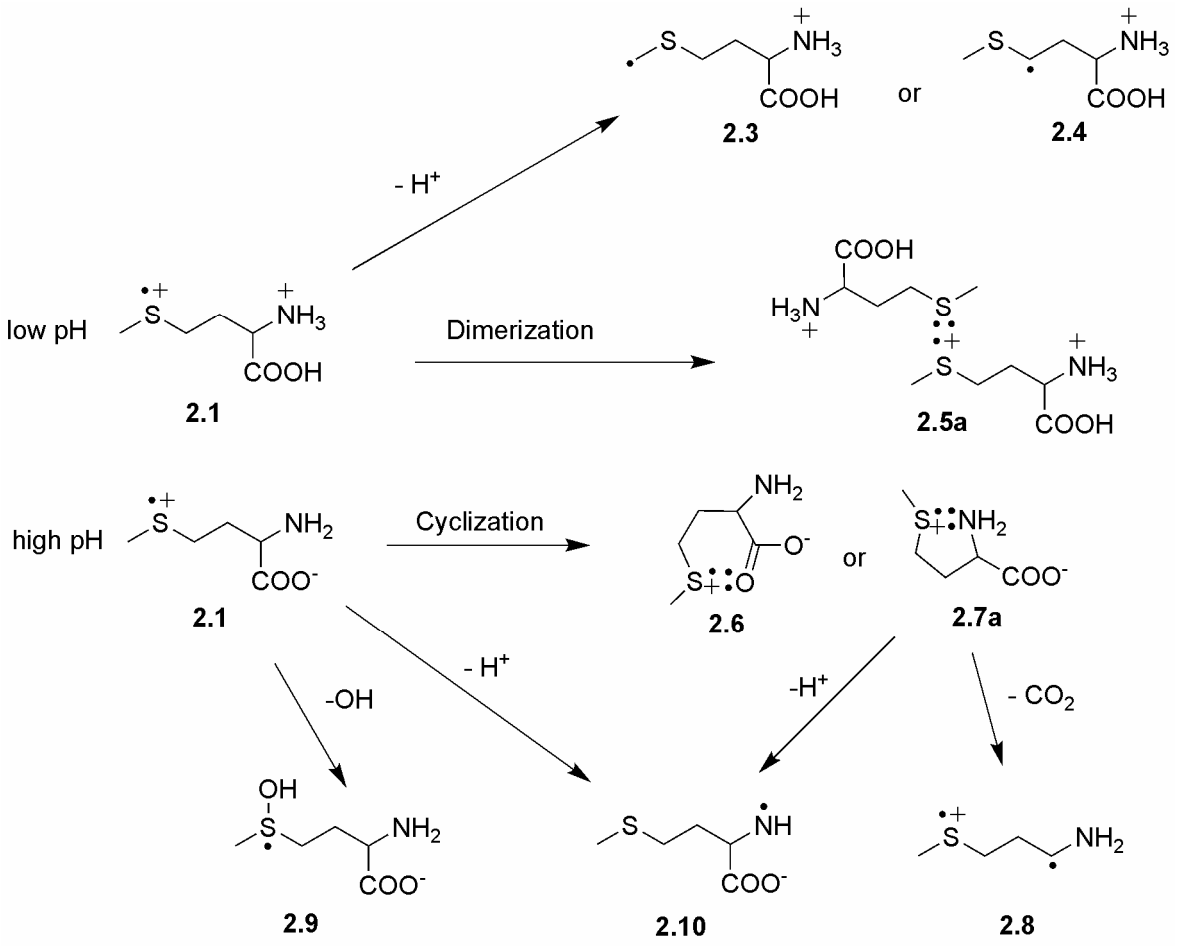

Scheme 2.2: Suggested one-electron oxidation pathways for methionine

were reported to only 3 significant figures. Resonance Raman experiments on (3–(methylthio)propylamine), a model compound for **2.1**, by Tripathi and Tobien[31] also supported the existence of the 5–membered ring structure. They suggested that it is formed through an –SOH type intermediate such as **2.9**. Recent papers by Schoeneich and coworkers have suggested that the 6–membered ring structure **2.6** with an S–O three electron bond is an important intermediate with regard to the β–amyloid fibril formation reaction.[32] It should be noted that this reaction is limited to cases where the methionine residue is part of a protein or short peptide, and not a free standing amino acid. They have also reported evidence for its existence in product analysis studies using hydroxyl radical as the oxidant.[33] However, those experiments were carried out with the amide of methionine, and not the amino acid itself. There may be subtle steric or electronic factors that favor and S–O bond over an S–N bond in some derivatives of methionine. New *ab initio* calculations by both the Schoeneich group[34] and by Huang and Rauk[35] support this. The latter paper also suggests that the deprotonation reaction of the non–cyclic structure to give α-thio alkyl radicals (**2.3** or **2.4**) may also be a possible reaction pathway. In this regard, deprotonation of the 5–membered ring structure to give the linear aminyl radical **2.10** may also be important.

In other experiments using magnetic resonance detection, there have been several reports offering indirect evidence for some of the structures shown in Scheme 2.2. An interesting study of this chemistry was reported by Goez et al.,[36] who used steady-state chemically induced dynamic nuclear polarization (CIDNP) measurements of products formed from the S–N bonded 5–membered ring structure. They discussed their results in terms of a dynamic equilibrium between the linear and cyclic species, and concluded that formation of the cyclic cation was "not strongly exergonic".[37] A study by Korchak, et al.[38]

reported the magnetic field dependence of the CIDNP signals, which led to estimates of some of the hyperfine interactions in the cyclic structure; we will comment further on those results in the discussion section below. These CIDNP experiments represent the only high resolution magnetic resonance characterization of methionine-related redox intermediates to date. A precise map of the spin density distribution in cations **2.5a** and **2.7a** has remained elusive.

Several of the reactions described in Scheme 2.2 may be fast at room temperature and therefore the concentration of **2.1**, **2.5a,** or **2.7a** in such solutions may be too low to detect by conventional steady–state EPR methods. This is to be expected especially for the decarboxylation and deprotonation reactions. This problem is circumvented in two ways. First, by using the TREPR method we detect the cation when there are large concentrations of it present. Second, when the amide nitrogen is acetylated, the secondary reactions are retarded to such an extent that the lifetime of the cyclic structure in solution may be extended significantly. Another major focus of these studies is the radical cation of N-acetyl methionine (**2.2**), which is a good small molecule model compound for Met–containing proteins because of the amide bond at the N–terminus.

This chapter presents high resolution TREPR spectra of cations and other free radicals produced from reactions of methionine and N-acetylmethionine with photoexcited AQS. Characterization data in the form of electron chemical shifts (free radical g–factors) and isotropic hyperfine coupling constants will be put forward and discussed. With this particular system it is advantageous to conduct the TREPR experiment at the Q–band microwave frequency (35 GHz), where chemical shift resolution is higher than the standard X–band spectrometer. Our experimental strategy is to use isotopic substitution to confirm

hyperfine coupling constants, and to use spectra acquired at two different frequencies to improve the precision of our g–factor measurements. In some cases, running the experiment at a higher frequency also leads to more accurate hyperfine coupling constants because it can eliminate the problem of spectral overlap than often plagues EPR analysis at lower frequencies.

2.3 Results and Discussion

2.3.1 pH Dependent Formation of Radicals from L-Methionine

Figure 2.1 shows X–band TREPR spectra obtained at room temperature in aqueous solution of pH = 2 when AQS is irradiated in the presence of L–methionine. In Figure 2.1A the spectrum obtained at a delay time of 700 ns after the laser flash is shown, with a simulation overlaid. The spectra exhibit strongly emissive transitions due to the triplet mechanism of chemically induced electron spin polarization (CIDEP),[15] a well understood phenomenon and typical for radicals or radical ions produced from excited states of quinones.[39] The simulation in Figure 2.1A uses two sets of hyperfine coupling constants resulting from interaction of the unpaired electron with 6 equivalent methyl protons and 4 equivalent methylene protons, respectively. Such a hyperfine coupling pattern can only arise from a dimer type structure such as **2.5a** in Scheme 2.2. The concentration dependence of this TREPR signal also supports this conclusion: The signal intensities are proportional to the square of the concentration, however we were never able to go low enough in concentration to see the monomeric cation before going below the sensitivity of the apparatus. The g-factor and coupling constants used for the simulation are listed in Table 2.1. They are in good agreement with those found in model systems by other research groups.[40] The AQS–

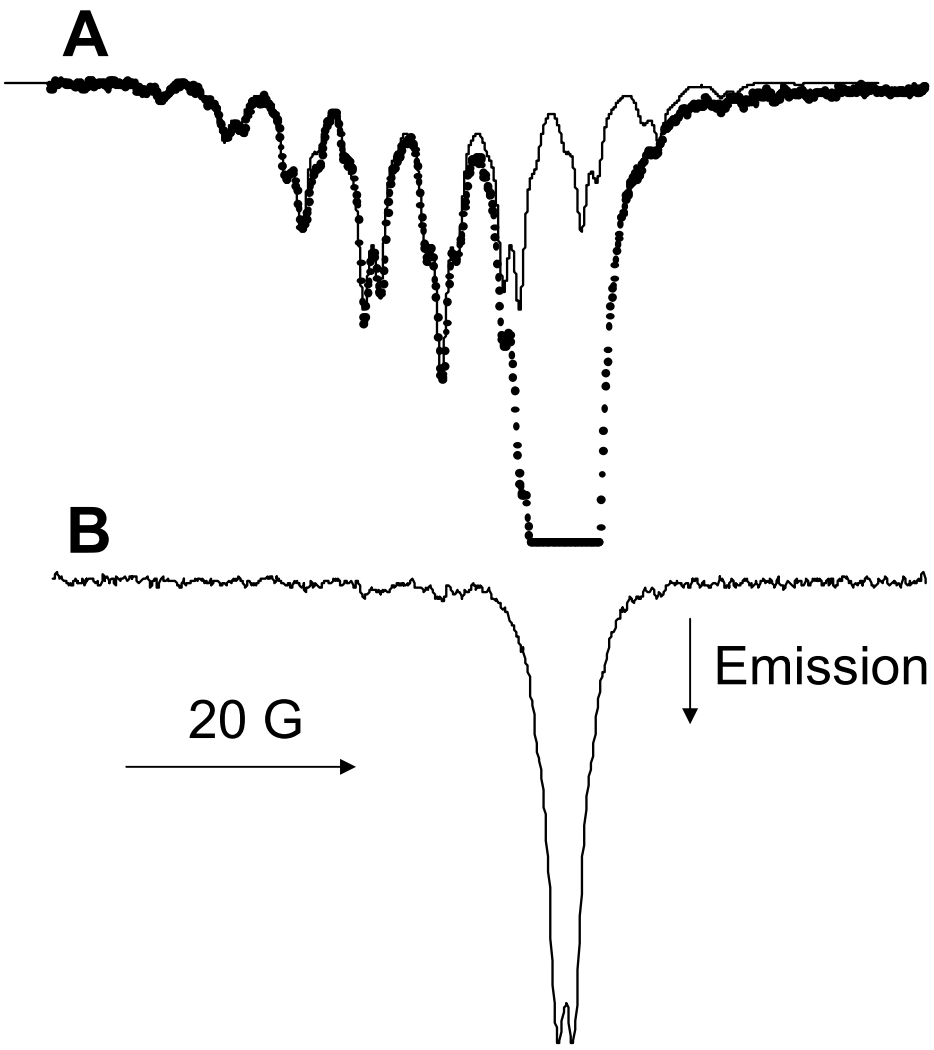

Figure 2.1: Time dependence of the X-band TREPR spectra taken upon irradiation of L-methionine and AQS in H_2O (pH 2.0) at: A) 0.7 μs (dotted line) B) 2.0 μs. Simulation of A is overlaid (solid line) on the experimental spectrum. See Table 2.1 (radical **2.5a**) for magnetic parameters. The magnetic field sweep width is 80 G. The TREPR intensity (y-axis) is in arbitrary units. In this and all subsequent spectra, lines below the baseline are in emission, while those above the baseline are in enhanced absorption.

Substrate	Radical	Structure	g-factor	alpha-H(D) (G)	beta-H(D) (G)	Other (G)
AQS	**AQSH•**	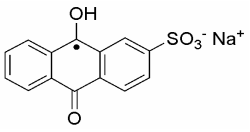	2.0038	1.8 (O-H)		
Methionine in H_2O (low pH)	**2.5a**	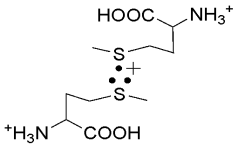	2.0101		7.12 (6H) 5.66 (4H)	
NAM in H_2O (low pH)	**2.5b**	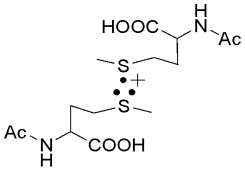	2.0101		6.92 (6H) 6.05 (4H)	
Methionine in H_2O (high pH)	**2.1**	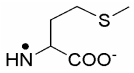	2.0043	21.92 (H_N)	33.30 (H_C)	13.36 (N)
Methionine in D_2O (low pH)	**2.10-d**	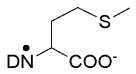	2.0043	3.32 (D_N)		13.36 (N)
NAM in H_2O (high pH)	**2.7**	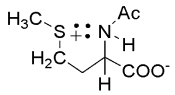	2.0073	9.57 (H_N)	8.30 (3H) 7.38 (2H) 1.35 (H)	
NAM-d_3 in H_2O (high pH)	**2.7-d_3**	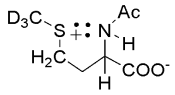	2.0073	9.57 (H_N)	1.27 (3D) 7.38 (2H) 1.35 (H)	
NAM in D_2O (high pH)	**2.7-N-d**	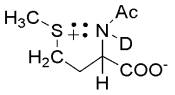	2.0073	1.47 (D_N)	8.30 (3H) 7.38 (2H) 1.35 (H)	

Table 2.1

signal was simulated using a single broad line as no hyperfine splittings were resolved at this delay time (due to uncertainty broadening effects discussed in Chapter 1).

Figure 2.1B shows the same system detected at 2 μs after the laser flash, where only the AQSH• radical is observed (large emissive doublet). The disappearance of the methionine dimer radical cation on this time scale is most likely due to two processes: spin–lattice relaxation and degenerate electron exchange. It is reasonable to expect that the dimer will relax faster than the AQSH• radical due to the heavy atom effect of the sulfurs. The exchange reaction, while not a chemical decay process in itself, will quench polarization due to scrambling of the nuclear spin systems.

Figure 2.2 shows the pH dependence of the methionine/AQS system as detected by TREPR 200 ns after flash photolysis at 308 nm. Clearly there is an evolution of the dimer signal to a different carrier at about pH 9, which is at approximately the pK_a value of the protonated nitrogen of the amino group. The higher pH spectra are at first glance a bit confusing to decipher because of the intensities of the transitions, which do not appear to be all emissive (E) or absorptive (A), nor do they follow any familiar pattern of CIDEP such as low field E, high field A, which would be expected from the radical pair mechanism. The intensities will be commented on below, but note here that there are not many transitions and they are well spaced, indicating that only a few hyperfine coupling constants are present. This does not fit the expected pattern for the cyclic structure **2.7**, which leads us to suggest that either the cyclic structure is not formed, or that once formed it has another chemical decay pathway available to it such as deprotonation at nitrogen. Our simulations, presented and discussed below, support the latter hypothesis.

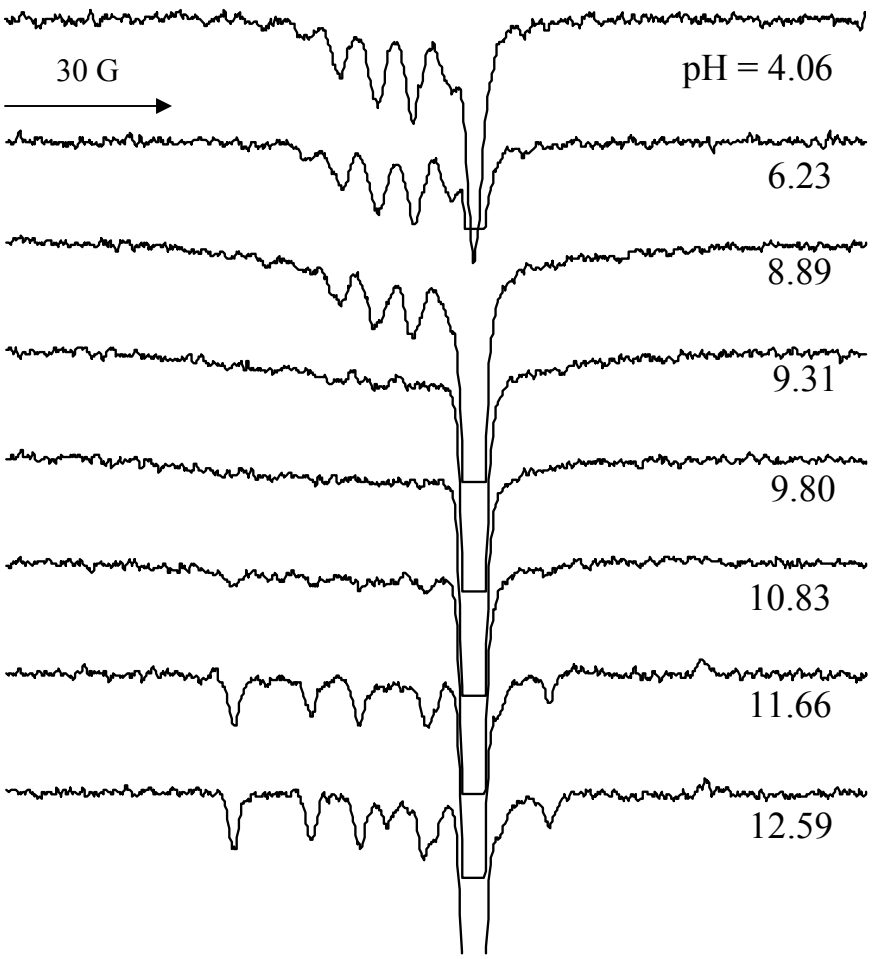

Figure 2.2: pH dependent X-band TREPR spectra taken of L-methionine and irradiated AQS in H_2O at 0.2 μs delay time. The pH values are shown directly below the spectra. The sweep width for all spectra is 150 G.

The spin polarization pattern observed in Figures 2.1 and 2.2 is dominated by the triplet mechanism, which is strongly emissive as expected for photochemical reactions from quinone triplet states.[39] The AQS–• radical formed in basic solution has a g-factor of 2.0040 and appears as a broad single line due to unresolved hyperfine interactions on the aromatic ring. In acid solution the AQSH• radical is observed due to rapid protonation at oxygen, and the signal appears as an emissive doublet with a g-factor of 2.0034, slightly upfield from AQS–•. We have expanded the spectra vertically to show the detailed hyperfine structure of the other radicals, therefore the g-factor difference in the two AQS-based radicals is not visible. However, in our Q-band spectra reported below it will be very obvious that there are two different counter-radical signal carriers as a function of pH. The advantage of using AQS as a sensitizer is clearly seen here as it does not overlap much with the other radicals, allowing for their more precise characterization. It is a better choice for EPR studies than 4-carboxybenzophenone, for example, which has been used by other researchers for amino acid oxidation studies,[38,41] but has multiple hyperfine interactions that overlap to a large extent with the other radicals' signals at g = 2.

Figure 2.3A shows the TREPR spectrum acquired at pH > 12 from Figure 2.2, along with a simulation in Figure 2.3B using literature parameters for a typical aminyl radical **2.10**.[42-44] At these pH values, deprotonation of the cyclic methionine radical cation to the aminyl radical is fast. Here the y-axis is expanded and the spectra have been signal averaged slightly longer to show all the TREPR transitions. Examination of Scheme 2.2 shows that there are two pathways by which the aminyl radical can be produced: 1) loss of a proton from the cyclic structure **2.7**, or 2) electron transfer from nitrogen to sulfur after the initial creation of the non–cyclic cation **2.1**, followed by loss of a proton. In fact there is a third pathway

(not shown in the Scheme) involving direct photo-oxidation of the nitrogen followed by proton loss,[41] but we rule this out based on the much lower ionization potential for the sulfur lone pair electrons. This difference in ionization potentials also leads us to rule out the second pathway described above, as it is unlikely that an uphill electron transfer event will occur on this time scale, especially with a flexible spacer between the donor and the acceptor. We conclude that the most likely pathway for production of the aminyl radical at room temperature from methionine above pH 9 is loss of a proton from the cyclic radical cation, which then no longer remains in the cyclic geometry because the stabilization of the positive charge on the sulfur atom is not necessary. In some of the broader spectra in Figure 2.2, at about pH 7 or 8, the cyclic structure may be present but significantly lifetime broadened by this process or by the cyclization process itself, which may be dynamic on this time scale. This possibility will be commented on below.

It is important to note that the simulation in Figure 2.3B only attempts to reproduce line positions and chemical shift information and not the intensities. As noted above, the intensities of the transitions in Figure 2.3A are quite unusual, with some lines nearly being cancelled out and others appearing in absorption where one would predict emission. We suggest that this pattern arises because of what is known as a spin "memory effect."[45-47] The initially formed cation contains two protons on the amine nitrogen, both of which are coupled to the unpaired electron. The radical pair mechanism spin polarization is created in this radical. Deprotonation takes place mostly after this polarization has formed, but the resulting aminyl radical has one less proton and therefore it carries the splitting pattern of the second radical but each transition "remembers" the spin polarization obtained in the first radical. This is an interesting phenomenon in its own right which has been observed many times in

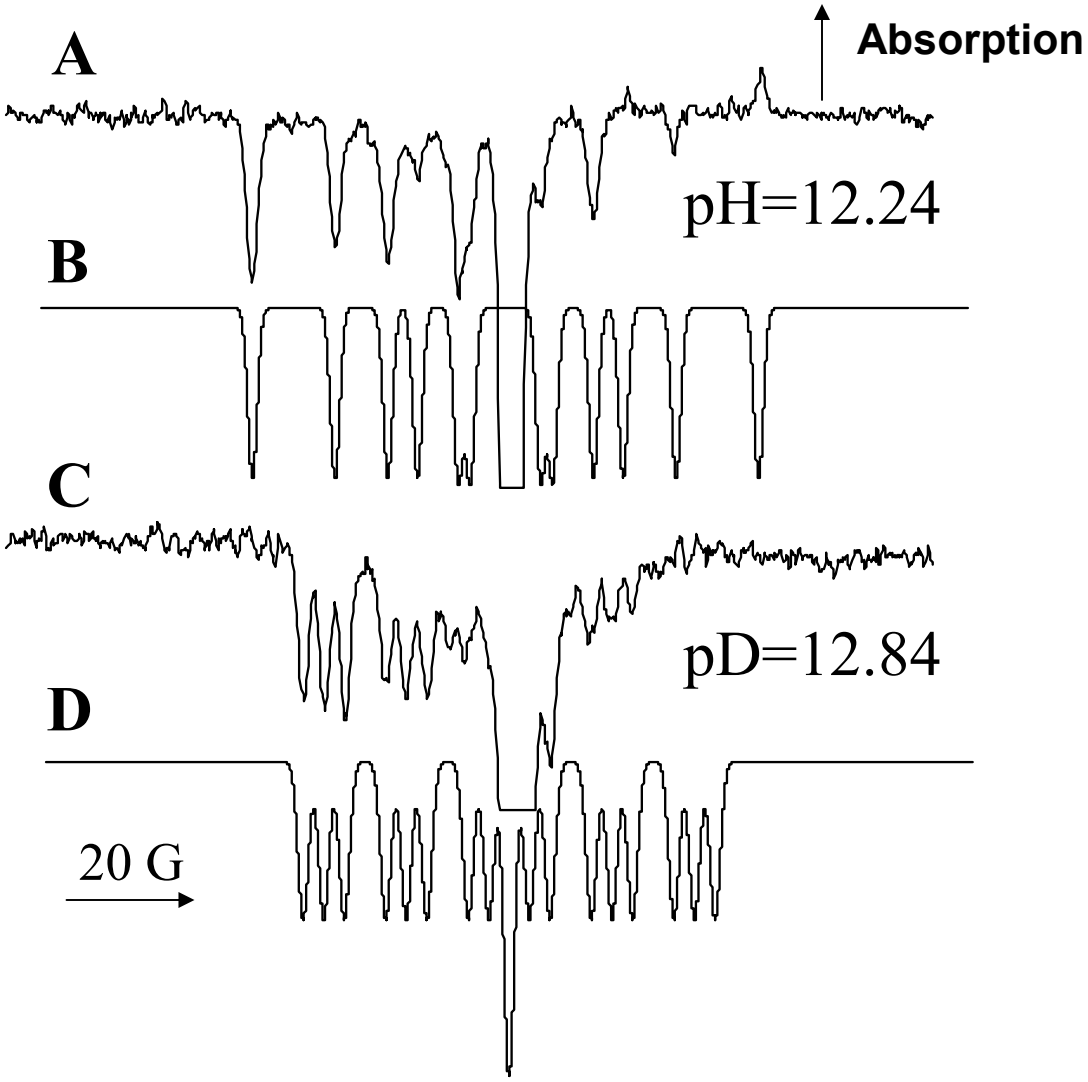

Figure 2.3: High pH/pD X-band TREPR spectra of L-methionine and irradiated AQS taken at 0.2 μs delay time in: A) H_2O C) D_2O. Exact pH/pD values are shown below corresponding spectra. B) and D) simulations of A and C, respectively. See Table 2.1 (radical **2.10a**) for parameters. The sweep width for both spectra is 150 G.

solution phase CIDNP experiments[48] and in solid-state TREPR experiments on, for example, photosynthetic reaction centers.[45-47] This memory effect for non-interacting monoradicals in liquid solution by TREPR has not been reported previously. Our model for the phenomenon and more precise simulations will be presented in Section 2.3.3.

To further support the assignment of the spectrum in Figure 2.3A to the aminyl radical, the experiment was run in D_2O instead of H_2O. This is expected to result in efficient deuterium exchange at nitrogen, which should give radicals with different spectral patterns for either the cyclic structure or the aminyl radical. The resulting experimental TREPR spectrum is shown in Figure 2.3C along with a simulation (Figure 3D) that uses the same hyperfine coupling constants as for the simulation in Figure 2.3B except that the aminyl proton now has I = 1 and a coupling constant of 6.5 less than its protonated analog. It is interesting to note that the spectral intensities in Figure 2.3C follow the same deviation in intensities as the protonated analog. This follows in a manner consistent with our model for sequential radicals and a memory effect discussed above. Again it should be noted that no effort is made in these simulations to account for the deviations from "normal" CIDEP intensities; only the line positions have been used to make the structural assignment.

2.3.2 The pH Dependent Formation of Radicals from N-acetyl-L-Methionine Analogs

In order to better characterize the cyclic radical cation **2.7**, it was recognized that the deprotonation reaction leading to the aminyl radical **2.10** had to be slowed down so that the cyclic structure could be observed directly by TREPR. To accomplish this, we used N-acetylmethionine (**2.2**), which changes the N-terminus of the amino acid from an amine to an amide. This increases the pK_a of the proton on the N terminus by almost fifteen units and

deprotonation at nitrogen will not occur.[49] In this case the cyclic structure, once formed, should have a much longer lifetime than for methionine. Scheme 2.3 shows how acetylation simplifies the possible redox chemistry with AQS. Figure 2.4 shows the pH dependence of the X–band TREPR spectra acquired after irradiation of the N–acetylmethionine/AQS system. At low pH, an 11 line pattern is observed from 10 nearly equivalent protons as in Figure 2.1A, therefore this signal is assigned to the dimer radical cation. A new signal carrier grows in at high pH that is different from the dimer spectrum. Furthermore this new signal is not due to the aminyl radical observed in Figures 2.2 and 2.3, as it has a completely different hyperfine pattern (cf. Figure 2.2, bottom, and Figure 2.3, top).

Figure 2.5A shows the pH = 5.8 spectrum from Figure 2.4, next to a spectrum run in D_2O as the solvent instead of H_2O (Figure 5B). It is clear that there is no isotope effect upon deuterium substitution at the N–terminus of this derivative of methionine radical cation. The simulation in Figure 5C reproduces both spectra extremely well, and we assign both spectra to the dimer of the radical cation of N-acetylmethionine. We will comment further on the absent isotope effect when the high pH data from Figure 2.4 is considered below. Parameters used in the simulation are listed in Table 2.1. The hyperfine coupling constants are slightly different than those for methionine radical cation, decreasing for the methyl protons while increasing slightly for the methylene protons. This is an expected result as the carbonyl moiety of the acetyl group is electron withdrawing and so the shift in electron density for this species is in the predicted direction.

Figure 2.6A shows the TREPR spectrum from Figure 2.4 acquired at pH = 12.2. Immediately below it in Figure 2.6B is a simulation, using parameters listed in Table 2.1, that is consistent with the 5–membered ring, S–N three electron bonded, cyclic radical cation of

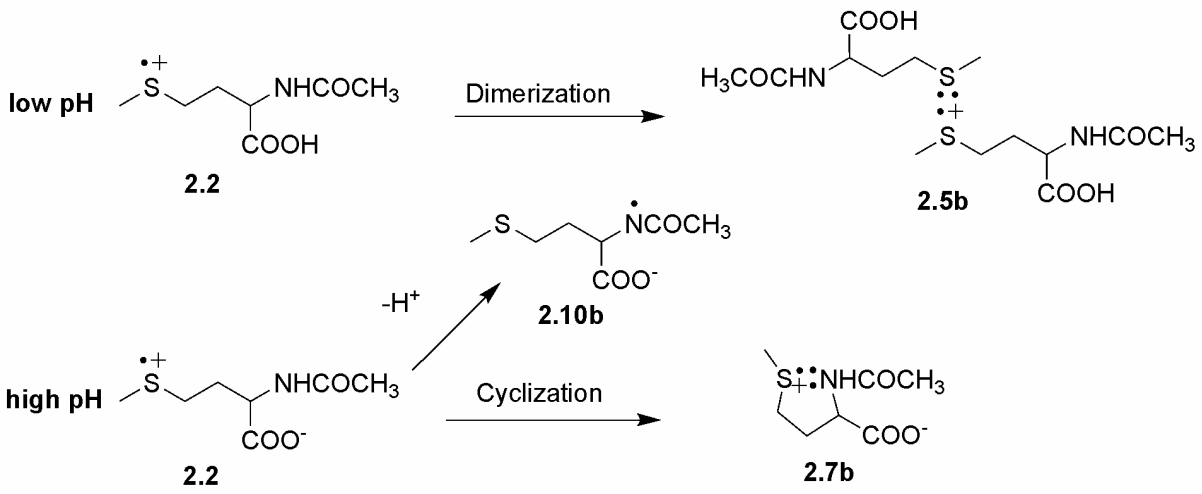

Scheme 2.3: Formation of NAM radicals at different pH values

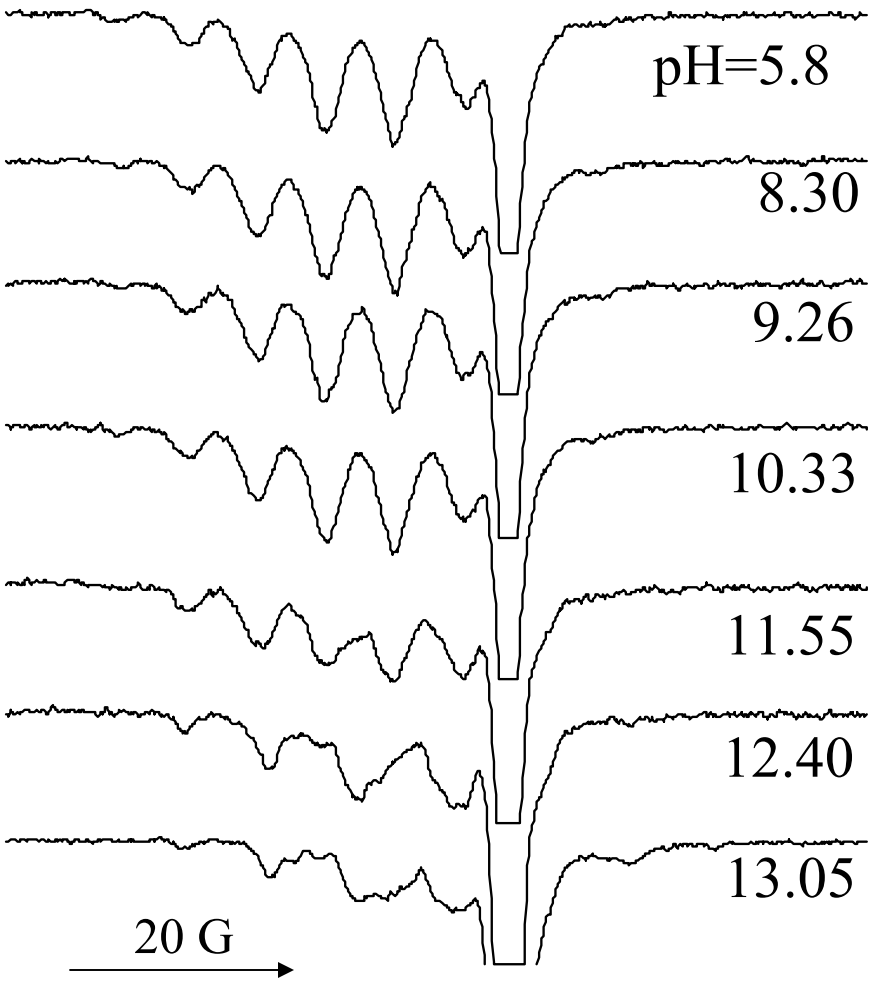

Figure 2.4: pH dependent X-band TREPR spectra of N-acetyl L-methionine and irradiated AQS in H_2O at 0.2 μs delay time. Exact pH values are shown directly below the spectra. The sweep width for all spectra is 80 G.

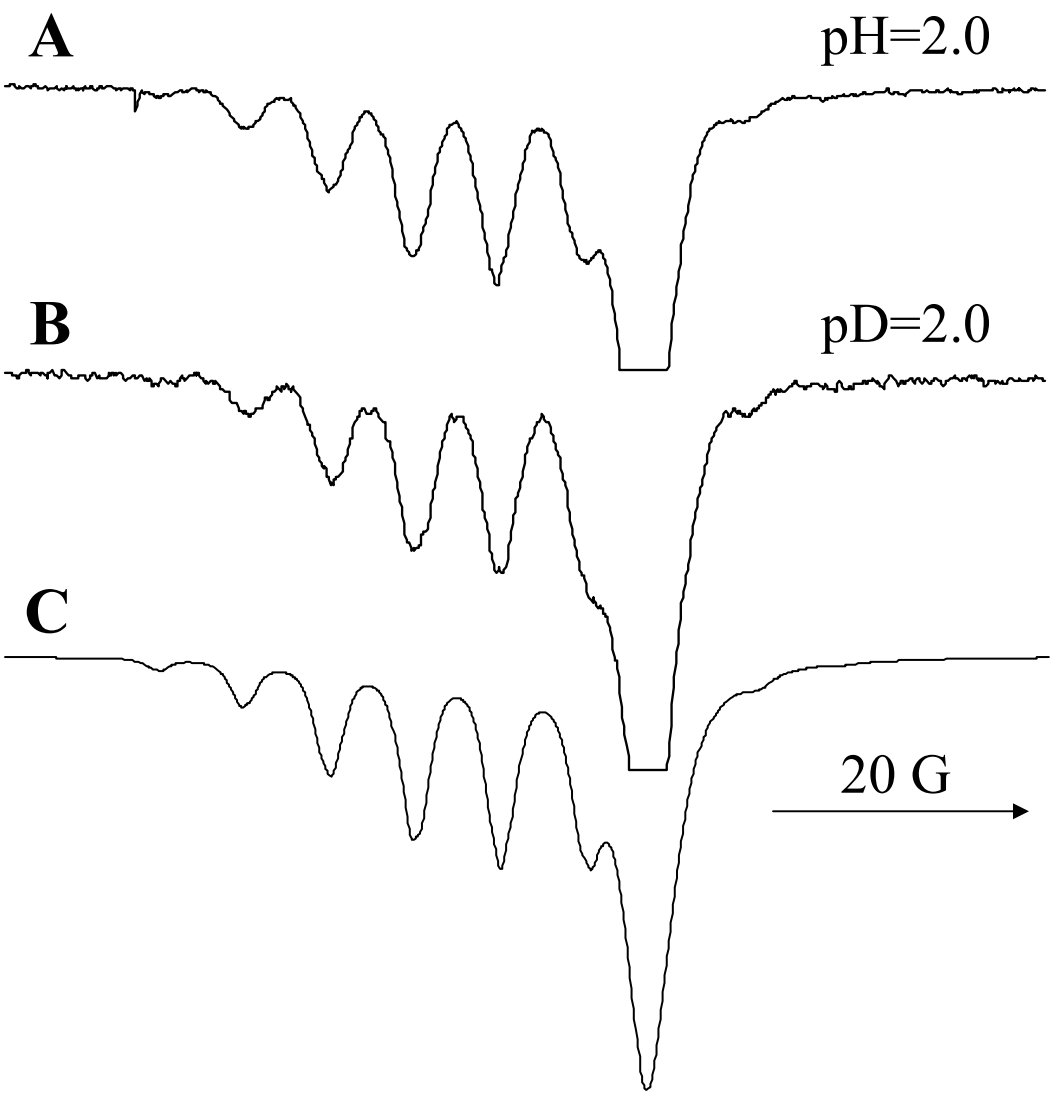

Figure 2.5: Low pH/pD X-band TREPR spectra of N-acetyl L-methionine and irradiated AQS taken at 0.2 μs delay time in: A) H_2O B) D_2O. Exact pH/pD values are shown above the corresponding spectra. C) simulation of A using parameters shown in Table 2.1 (radical **2.5a**). The sweep width for both spectra and simulation is 80 G.

N–acetylmethionine (**2.7**). To provide further support for this assignment, we performed the two isotopic substitutions illustrated in Chart 2.1. The first substitution was carried out as before by running the experiment in D_2O, where we expect H/D exchange at the N–terminus (Chart 2.1, right hand side). In this case we expect to see little or no effect for the dimer structure at low pH because there are no exchangeable protons near the radical center in the dimer, and this is indeed the case as per our discussion of Figure 2.5 above; the spectra of the dimer in H_2O and D_2O are identical. At high pH however, an isotope effect on the spectrum is observed (Figure2. 6C) and the simulation below the experimental spectrum (Figure 2.6D) tells us that the deuterium substitution was made at the amide nitrogen. The simulation was carried out once again with all parameters from the protonated structure in Figure 2.6A except for the deuterium atom on nitrogen which was given I = 1 and a coupling constant of 6.5 times less than that of the corresponding proton (Table 2.1).

Additional support for the cyclic structure comes from isotopic substitution at the methyl group on the side chain of N-acetylmethionine (Chart 2.1, left hand side). A sample of L–methionine with a CD_3 group in place of the CH_3 group was purchased and converted to the N-acetylmethionine-d_3. A subsequent TREPR experiment with ^{3}AQS* oxidation at high pH led to the spectrum shown in Figure 2.7B which is attributed to radical **2.7-d$_3$**. The protonated analog is shown for comparison immediately above it in Figure 2.7A. There is a large change in the spectral width and number of transitions between these two figures. Once again, spectral simulation with the predictable changes in spin quantum number and coupling constant for those 3 protons/deuterons leads to excellent agreement (Figure 2.7C, Table 2.1) for the cyclic structure.

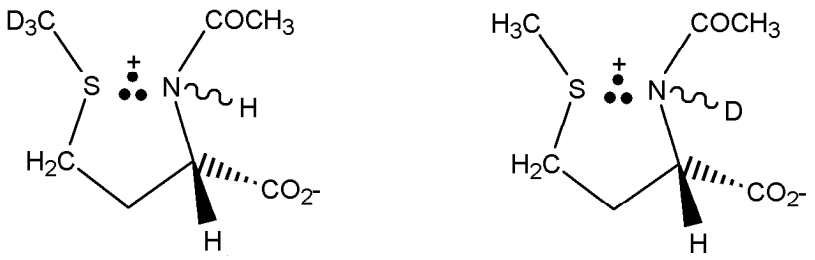

Chart 2.1: Isotopically labeled cyclic radical cations formed from the oxidation of NAM analogs

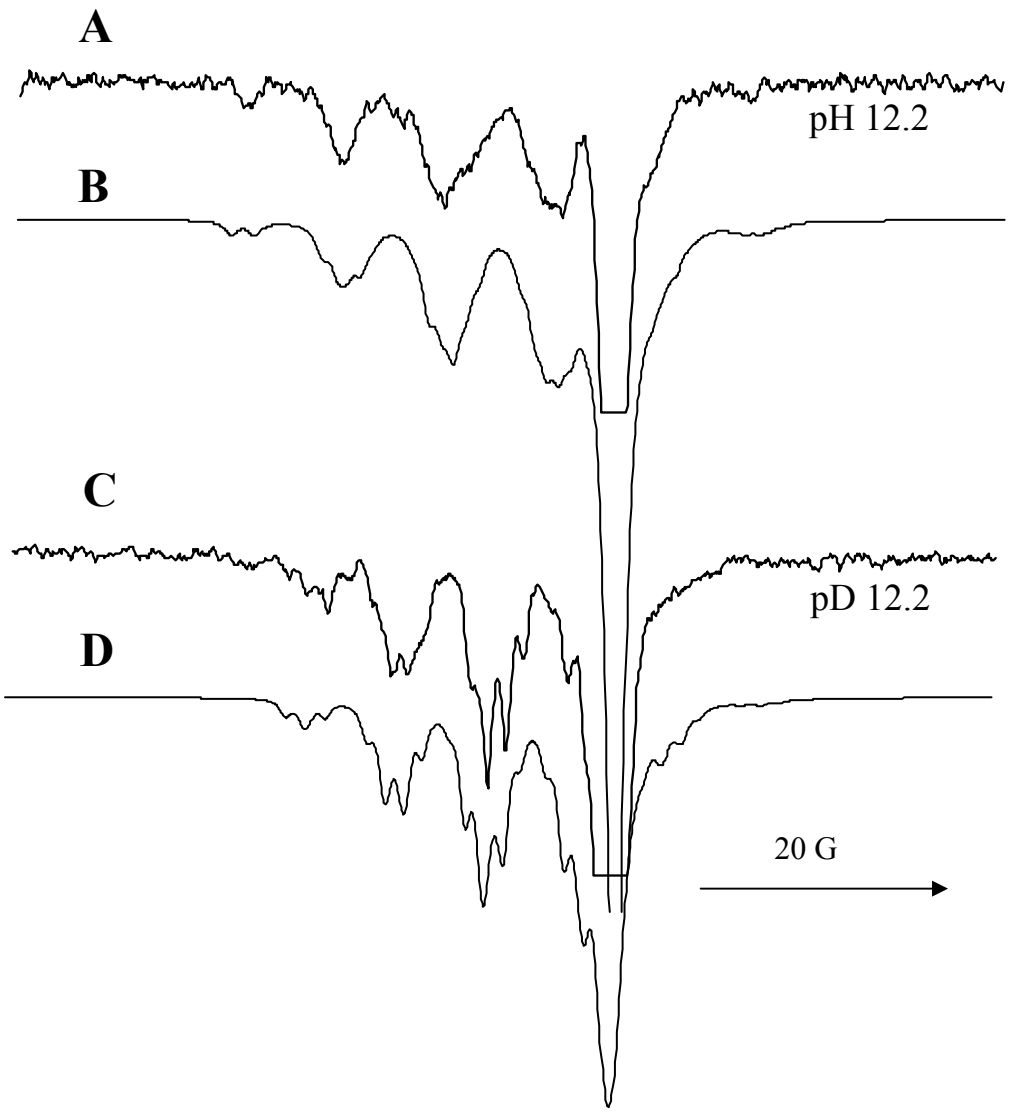

Figure 2.6: High pH/pD X-band TREPR spectra of irradiated N-acetyl L-methionine and AQS taken at 0.2 μs delay time in: A) H_2O C) D_2O. Exact pH/pD values are shown directly below the spectra. B) and D) simulations of A and C, respectively. See Table 2.1 (radical **2.7b and 2.7b-d1**) for parameters. The sweep width for both spectra and simulations is 80 G.

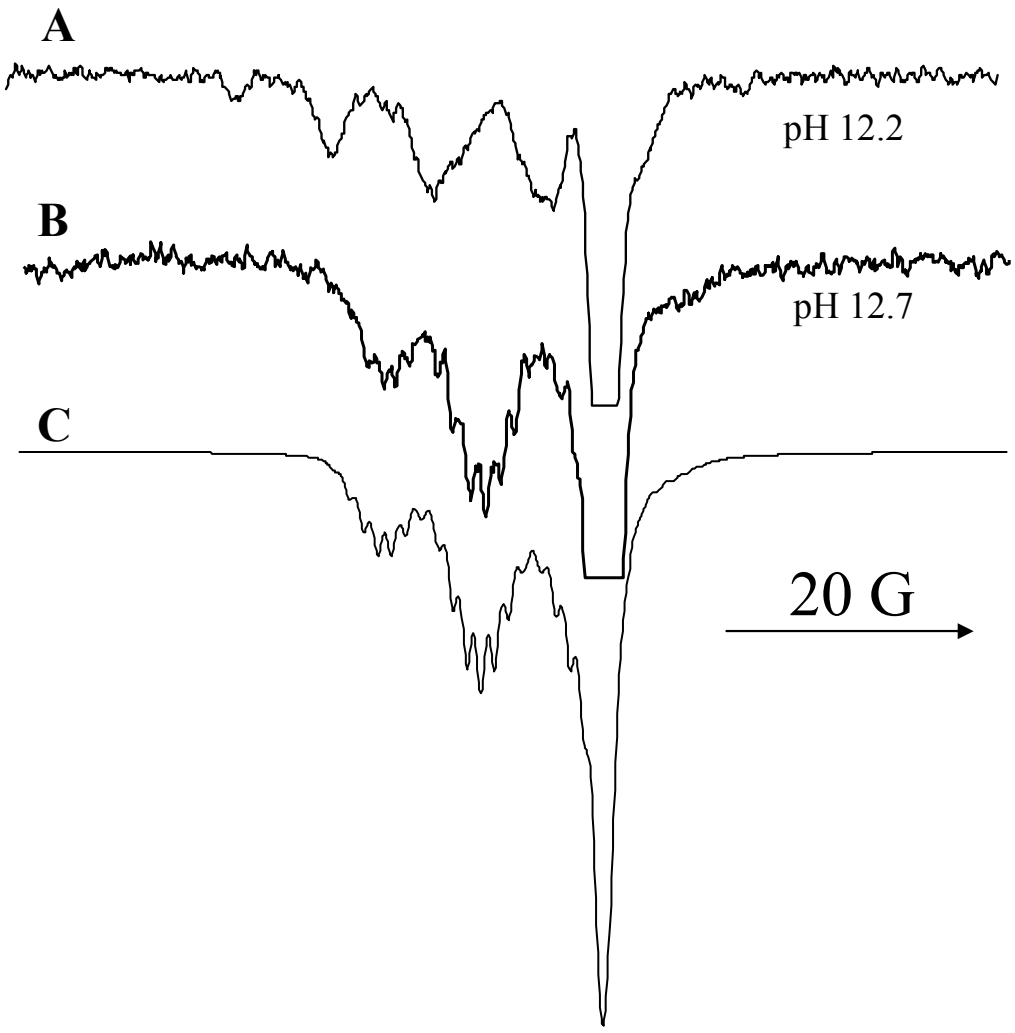

Figure 2.7: High pH X-band TREPR spectra of irradiated AQS and: A) N-acetyl L-methionine taken at 0.2 μs delay time B) N-acetyl L-methionine-*methyl-d_3* taken at 0.4 μs in H_2O. Exact pH values are shown below the spectra. C) simulation of B using parameters shown in Table 2.1 (radical **2.7b-d3**). The sweep width of both spectra is 80 G.

The coupling constants obtained for the cyclic cation of N-acetylmethionine are all hyperconjugative in nature except for the nitrogen. This is of interest as each coupling to these protons should be dependent on the dihedral angle and therefore to the ring conformations and/or dynamics. This will be commented on further below, but it should be noted here that the proton coupling constants are all smaller than usually observed for 5-membered rings[50] and this may be due to the σ-σ* nature of the three electron bond, *vide infra*. In such cases the hyperfine interactions might be expected to fall between those of a neutral radical and, say, a radical anion where all coupling constants are typically much smaller than their neutral counterparts due to the distance of the unpaired electron from the nuclei. In some cases this difference in hyperfine values can be an order of magnitude.

Figure 2.8 shows TREPR spectra of the N-acetylmethionine/AQS system measured at the Q–band microwave frequency. As mentioned above, deprotonation of this radical cation is slow even in strongly basic solution because it is an amide rather than an amine. Therefore, the dimer is observed at low pH and the cyclic structure at high pH. This experiment allowed very accurate g–factors to be obtained using field/frequency measurements and comparison to the X–band spectrum (Table 2.1). The observed splitting patterns are the same as at X-band for each radical, and are almost completely separated from the AQS signals at Q-band. It should be noted that in Figure 2.8B the polarization of the radical from AQS is absorptive – this is a common observation in Q-band experiments, where the higher field leads to stronger RPM[51] polarization. The RPM is driven here by the large g-factor difference and has the correct phase (E for the low field radical, A for the high field signal) expected for a geminate radical pair originating from a triplet state precursor and experiencing a negative

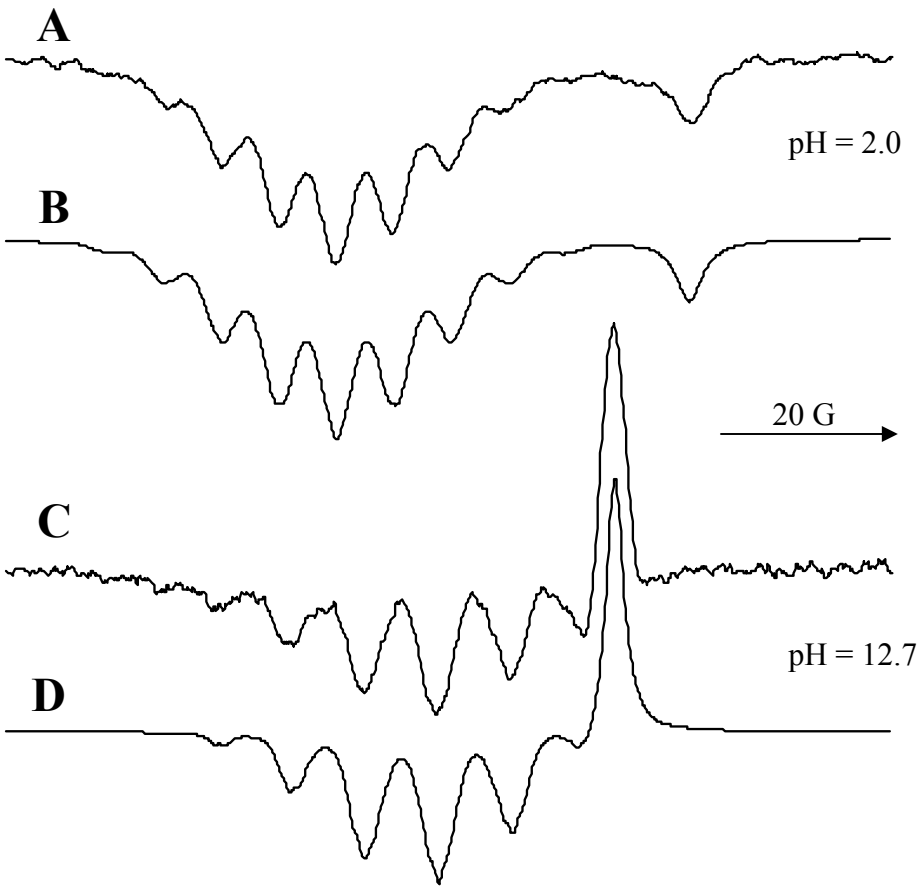

Figure 2.8: Q-band TREPR spectra of N-acetyl L-methionine and irradiated AQS in H_2O at: A) pH 2.0 taken at 400 ns delay time C) pH 12.7 taken at 150 ns. B) and D) simulations of A and C, respectively, using parameters shown in Table 2.1 (for radicals **2.5** and **2.7b**). The sweep width for both spectra is 100 G.

exchange interaction. The line widths are broader here than at X-band due to the shorter delay times of observation (uncertainty broadening).

The difference in g-factor between the S-S dimer structure (2.0101) and the cyclic S-N structure (2.0073) is easily understood using a resonance description. There are two main resonance structures that contribute to the stability and spin density of the cyclic cation. They have the general form S-N+• and +•S-N. The ratio of hyperfine coupling constants in the methyl protons of the dimer to the cyclic species is 8.30/7.12 = 1.17. This tells us that the S+• structure contributes roughly 60% to the overall g-factor (i.e., there is a greater spin density on the sulfur side of the three-electron bond). The remaining 40% comes from the N+• structure, which can be estimated by considering the literature value for the g-factor of an alkyl amine radical cation (2.0034).[52,53] Weighing these two g-factors by their appropriate percentages, we can calculate the expected g-factor for a S-N+• structure: 0.6 x (2.0101) + 0.4 x (2.0034) = 2.0074. This is almost exactly the observed value of 2.0073. Of course, calculations of g-tensors from first principles are much more complicated than this, and we present the above comparison only to show that, using a fairly simple model, the correct trend can be estimated for this previously undetermined g-factor.

Figures 2.6, 2.7 and 2.8 represent solid evidence for the assignment of the TREPR signal carrier in high pH solutions of **2.2** with AQS to the cyclic radical cation of N-acetylmethionine. The isotopic substitution studies have provided several self-consistent datasets for the existence of **2.7** as a five-membered ring with the S–N three electron bond. If the six–membered ring with a S–O three electron bond were present instead, we would not expect an isotope effect upon substitution at the amide nitrogen, and a very different hyperfine splitting pattern would have been observed. To the best of our knowledge this is

the first room temperature liquid solution EPR characterization of any two-center three–electron bond radical cation.

A noteworthy feature of the magnetic parameters we have determined in this work is the very small hyperfine coupling for the nitrogen atom in the cyclic radical cation of N-acetylmethionine. This result implies that there is a very low spin density at nitrogen in this radical, which conflicts somewhat with the *ab initio* calculations of Huang and Rauk,[35] and is a somewhat different interpretation of the field dependent CIDNP data of Korchak et al,[38] who studied both methionine and N-acetylmethionine. In the work of Champagne and coworkers[30] the nature of the three–electron bond is described as a σ–σ* interaction and this may help explain why the coupling constant is small. If the unpaired electron is located in a σ* orbital, it will be further away from the nucleus. Also, the remaining electrons from the lone pair on nitrogen may "shield" the unpaired electron from the nucleus.

While the calculations of Huang and Rauk may show a trend in hyperfine interactions that is physically reasonable, the fact that they were run without neighboring solvent molecules makes their absolute values somewhat suspect. The cyclic cation has a negative and positive charge, and therefore the presence of nearby water molecules would be expected to have a large effect on its structure. In addition, if the cyclic cation is fluxional, solvent would be expected to play a large role in determining the average coupling constants. As for the field-dependent CIDNP data of Korchak, et al.,[38] the authors also reported a low hyperfine coupling constant for the nitrogen and the α-carbon of N-acetylmethionine, which is consistent with our observations. However, they concluded from this small value for a_N that the cyclic structure was not a reactive intermediate present in N-acetylmethionine chemistry, or at least did not live very long. However, we have clearly shown that the N-

acetylmethionine radical cation cannot deprotonate or form dimeric structures in basic solution, and both the g-factor and the proton hyperfine splittings are consistent with the cyclic species. All other candidates are ruled out by our isotopic substitution experiments and/or comparison to literature parameters.

The field-dependent CIDNP technique is not as reliable as TREPR for the determination of hyperfine couplings due to the large number of parameters needed (5 in reference 22). In addition, if the cyclic and linear structures are in a dynamic equilibrium for methionine as suggested by Goez,[37] then each method (CIDNP and TREPR) may be sampling different average values. Such averaging problems have been considered before when comparing exchange interactions in flexible biradicals using these two techniques.[54] Even a small amount of fluxional behavior in the five-membered ring may be enough to cause considerable discrepancy between values determined by each method. Five-membered rings are notorious for such behavior and have historically been the subject of considerable discussion and debate in the field of free radical chemistry.[55]

The effects described above may be especially pronounced if the bonding interaction is weak and the bond is long. For the S–O three electron bond the bond length has been predicted to be 2.7 Å,[35] so this argument seems reasonable. However, we present this only as a tentative argument at the present time as there does not appear to be any data, experimental or computational, on the length of the S–N three electron bond in either of the two cations. Since we can rule out the S–O bonded structure from our isotopic substitution experiments, we conclude that the S–N bonded structure is favored, although whether it is for steric or electronic reasons is an interesting point. Based on the relative electronegativities we concede that the S–O bond should be stronger. It is still possible however that the 5–

membered ring structure is sterically more stable because of favorable axial interactions in the ring.

More insight into the small hyperfine coupling at nitrogen in **2.7** comes from analyzing the effect of the neighboring sulfur atom itself in these structures. Consider the two radicals shown in Chart 2.2. Here the presence of an α-sulfur in the radical structure lowers the nitrogen hyperfine coupling constant by a factor of three.[43,56] If we extrapolate this effect to the nitrogen hyperfine coupling in an alkyl amine radical cation (~ 9-18 Gauss), we can expect a maximum value of 3-6 Gauss in the S-N bonded cyclic structure. This estimate, taken together with the bond length issue discussed above, makes our determination of a small a_N value in structure **2.7** somewhat easier to rationalize.

2.3.3 Polarization Transfer from Amine Radical Cation to Aminyl Radical

As mentioned earlier in section 2.3.1, the TREPR transitions attributed to the aminyl radical (**2.10**) in Figure 2.3A are difficult to simulate using normal TM and RPM CIDEP parameters due to their anomalous intensity pattern. The most noticeable (and odd) feature of this spectrum is the successive A-E-A polarization of the 3 peaks at highest field. Also, if all the peaks are grouped into pairs of 2, examining from left to right, the low field peak of each pair is more emissive than the next. This aminyl radical spectrum, observed both X- and Q-band, is shown in Figure 2.9. The fact that the same general spectral intensity patterns are observed at both frequencies means that this effect is an inherent property of the observed radical and is not affected by magnetic field strength. To illustrate that polarization pattern of this spectrum can be simulated, Figure 2.10, shows the experimental spectrum along with plots of different combinations of RPM and TM polarization. The closest combination of

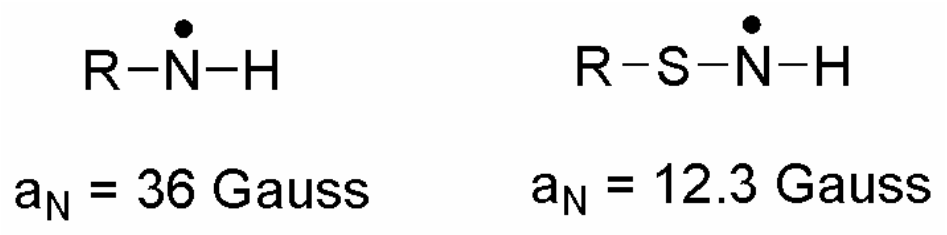

Chart 2.2: Aminyl and thio-aminyl radical hyperfines

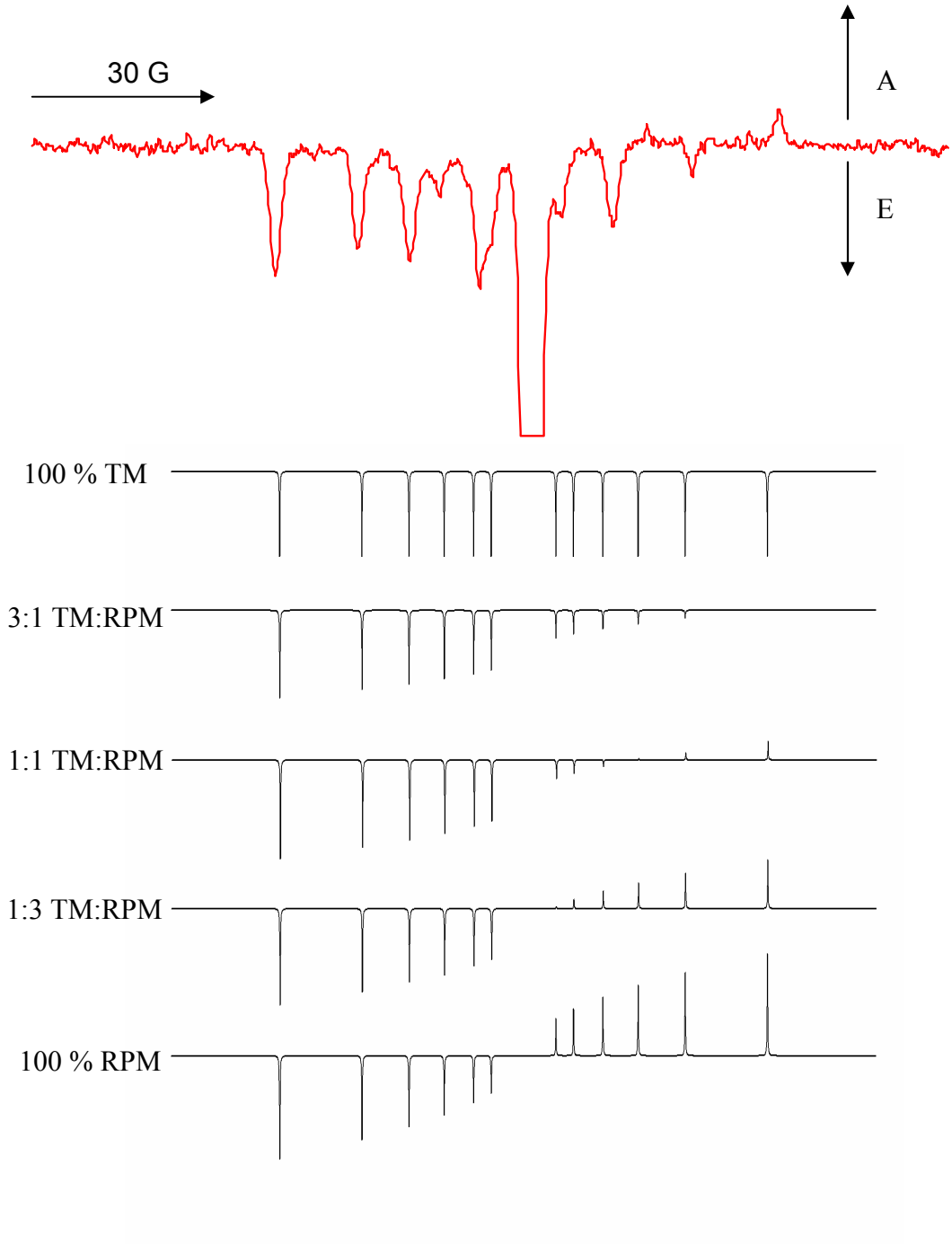

Figure 2.9: TREPR spectrum from Figure 2.3 shown with various simulations using different ratios of TM and RPM mechanisms.

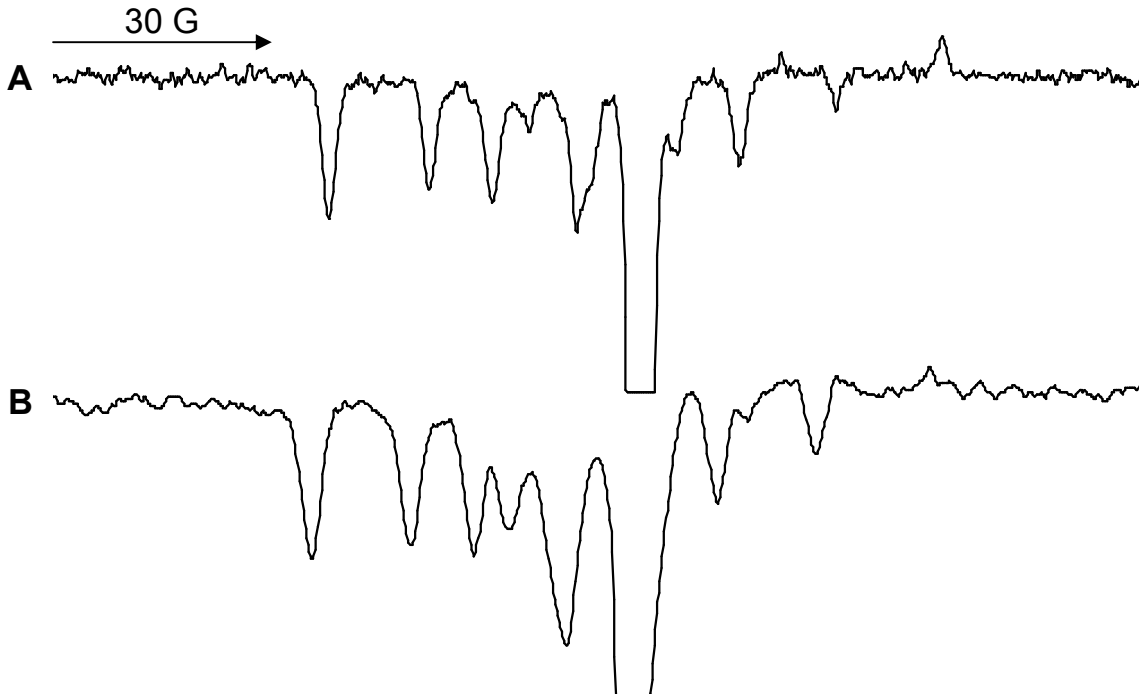

Figure 2.10: TREPR spectra taken after irradiation of 20 mM NAM and 8 mM AQS in aqueous solution (pH 12.5) at) X-band and B) Q-band frequencies.

these two mechanisms is a 1:1 RPM:TM ratio. This treatment still does not account for the emissive upfield peaks, nor the alternating E* transitions.

In order to determine the origin of spectral pattern of the aminyl radical, the deprotonation process that creates radical **2.10** must be considered. Chart 2.3 shows the deprotonation reaction by which the aminyl radical is formed. Upon irradiation in basic solution, methionine is oxidized at the sulfur center by ^{3}AQS*. Intra-molecular electron transfer then occurs from the amine to the sulfur, and the amine radical cation is generated. This radical cation can then deprotonate to produce the observed aminyl radical (**2.10**). Generally these deprotonation reactions are fast (< 10 ps), however, in cases where the radical cation can be stabilized (by formation of the cyclic radical cation **2.7**) this rate of deprotonation can be hindered. If the rate is slowed down to the nanosecond timescale, CIDEP polarization can be generated on the parent cation radical before deprotonation. This polarization can be then inherited by the aminyl radical that is directly observed. Figure 2.11 diagrams how this polarization is transferred to each observed aminyl radical transition. The top spectrum is a simulated spectrum of the amine radical cation generated using literature values for both the sign and magnitude of a_H. These literature values will be elaborated upon below. The middle spectrum is a stick plot of the observed aminyl radical spectrum. Each transition in this spectrum is a sum of two transitions from top spectrum, and the polarization tracks with the nuclear spin states. For example, the first transition at low field for the observed radical has the nuclear spin states: 'β' for the proton on the nitrogen, 'α' for the proton located on the adjacent carbon, and '1' for the nitrogen itself. The aminyl radical represented by this transition only inherits polarization from the parent radical cation with these same parameters. In the case of the parent radical: the $\beta\beta_{H(N)}$, $\alpha_{H(C)}$, and 1_N transition,

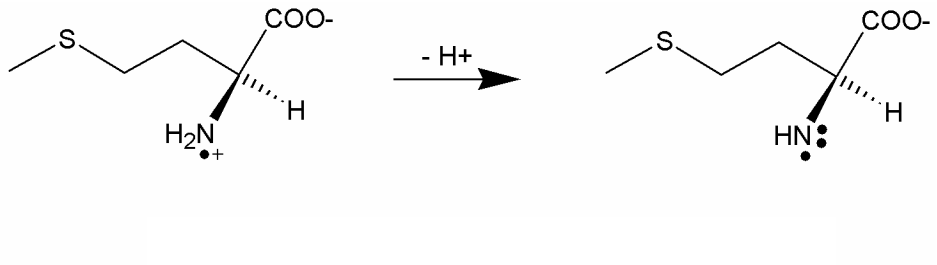

Chart 2.3: Deprotonation of amine radical cation to form aminyl radical

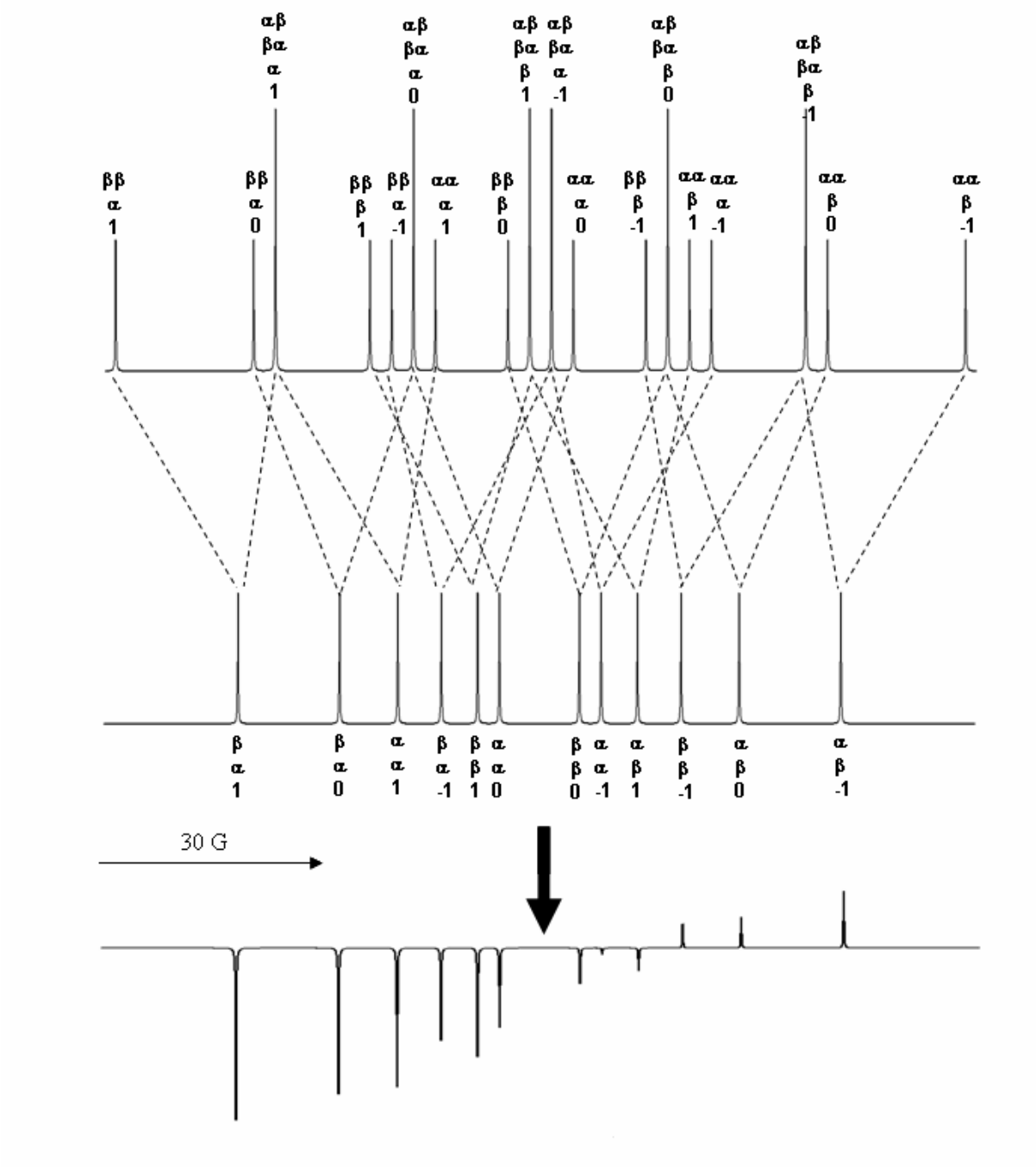

Figure 2.11: Polarization Transfer Diagram

as well as half the polarization from doubly degenerate $\alpha\beta/\beta\alpha_{H(N)}$, $\alpha_{H(C)}$, and 1_N radical. The resulting spectrum is shown at the bottom of Figure 2.11. The alternating E* pattern can be seen as well as a combination of emissive and absorptive peaks on right hand side of the spectrum. The phases and intensities of these peaks are greatly affected by the RPM:TM ratio generated in the parent radical cation and determined by the quality of the output for the aminyl radical.

In the computation of the peak intensities, the signs of the hyperfine coupling constants become very significant. A question was raised during this work as to the signs of each relevant hyperfine. If the sign of the hyperfine were to flip during polarization transfer from the parent radical cation to the aminyl radical, this would change which peaks from the parent funnel the polarization to the observed radical. Unfortunately, standard EPR techniques only give information about the magnitudes of hyperfine coupling constants, and the signs are not directly measured. To solve this problem, we performed extensive literature searches to determine the sign and magnitude of aH, as well as g-factors of nitrogen radical cations. The most pertinent reference of amine cation radical hyperfine signs found was for a $^{-}O_3S\text{-}NH_2^{+}\bullet$ in which both the a_N and $a_{C(H)}$ were found to be positive and the $a_{H(N)}$ negative.[57] The signs of the neutral aminyl radical hyperfine coupling constants appear to not to change based on a study by Iacona et al.[58]

The X-band spectrum is shown with simulation in Figure 2.12 with broader linewidths. The biggest discrepancy between the experimental spectrum and the simulation is the phase of the second peak from the right. One factor that may have caused this result is the lack of Δg in the simulations. No concrete values were found in the literature, and so a $\Delta g = 0$ was used in the simulation. This parameter will be varied in later simulations.

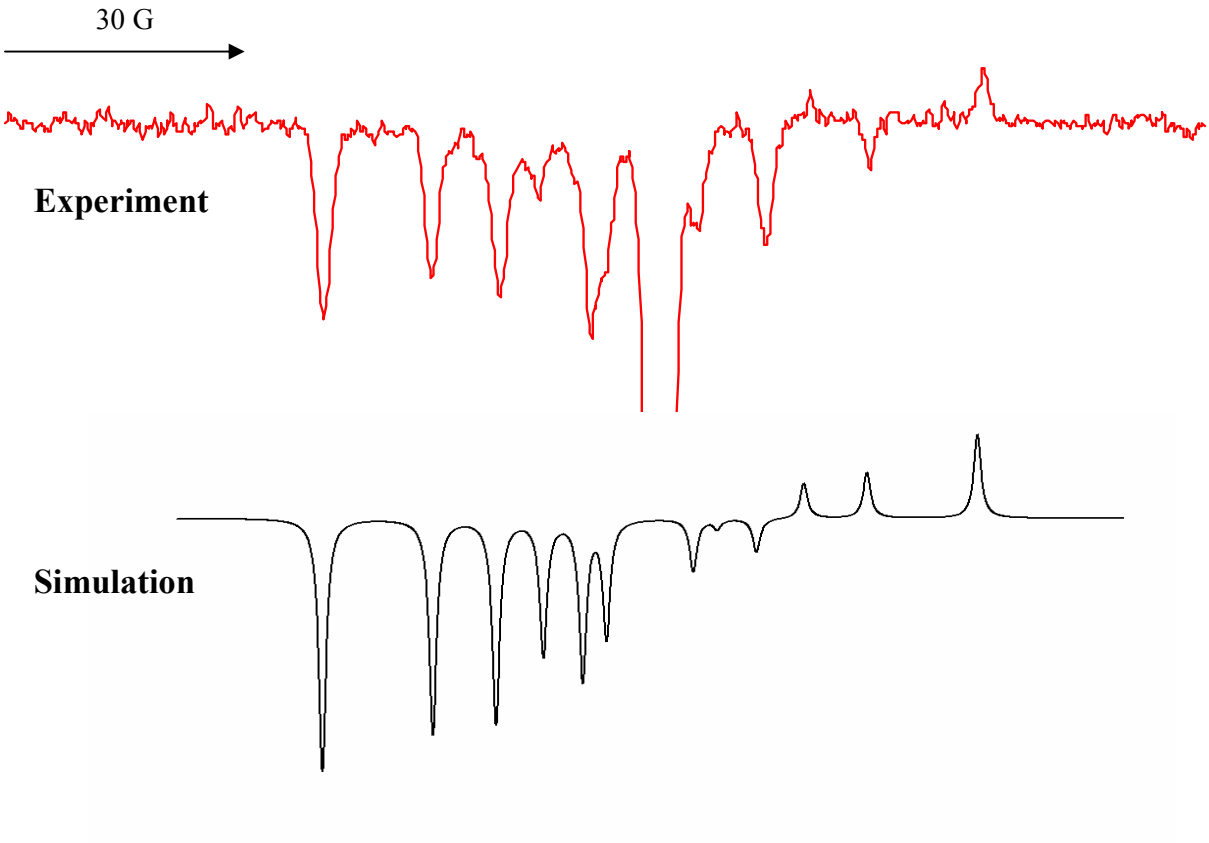

Figure 2.12: TREPR experimental spectrum of aminyl radical and simulation using polarization transfer from the amine radical cation.

2.4 Conclusions and Outlook

The precise magnetic parameters and the corresponding radicals are shown in Table 1. Using this Table and the chemistry in Schemes 2.1 and 2.2, this work can be summarized as follows: Deprotonation of **2.1** at any pH value to α–thio alkyl radicals **2.3** and **2.4** does not take place, and that the dominant structure observed in acid solution for both starting materials (**2.1** and **2.2**) is the dimer, **2.5**. In basic solution, decarboxylation to radical **2.8** or trapping by H_2O or HO^- to give hydroxythiyl radical **2.9** also appear to be slow or insignificant processes, at least on this time scale. Additionally, we see no evidence for the S–O three electron bond leading to the six–membered cyclic radical cation **2.6** proposed recently for methionine amide.[16] The appearance of either the five-membered ring cation **2.7** or the neutral aminyl radical **2.10** at high pH depends only on the rate of deprotonation of the cyclic cation, which in turn depends strongly on the substitution pattern at nitrogen.

Future studies on these interesting structures will include labeling with ^{13}C, ^{33}S, and ^{15}N to learn more about the spin distribution in the radicals and radical cations, especially in light of the very small nitrogen hyperfine coupling constant observed in the cyclic radical cation of both methionine and N–acetylmethionine. The stereochemical issue raised by the diastereotopicity of radical cation **2.7** is also of interest with respect to short peptides, dimers, trimers, etc. The memory effect observed in the aminyl radical and the resulting issue of polarization transfer from the protonated cation (Figures 2.2 and 2.3) have been modeled and discussed as well.

2.5 Experimental

Continuous wave TREPR experiments were performed at X-band as previously described.[10] All X-band (9.46 GHz) experiments were performed on a JEOL USA Inc. JES-REIX EPR spectrometer equipped with a fast preamplifier. The microwave power was 10 mW for all experiments. The aqueous solutions were circulated through a 0.4 mm quartz flat cell positioned in the center of a Varian TE_{103} optical transmission cavity. The solutions were irradiated using a Lambda Physik LPX-100i excimer laser (308 nm, XeCl) running at 60 Hz with an energy of 90 mJ (~20 mJ hitting the sample per pulse) and a pulse width of 20 ns. All spectra were collected in the absence of field modulation at variable delay times after the laser flash using a boxcar integrator (100 ns gates), while the external magnetic field was swept over 2 to 4 min.

Q-band TREPR experiments (34.6 GHz) were performed using a Varian E-110 spectrometer with a modified bridge as previously described.[41] The aqueous samples were circulated through a 0.4 mm i.d. quartz tube centered in a TE_{011} cylindrical cavity that was wire-wound to allow for sample irradiation.

All of the aqueous samples were prepared with 20 mM amino acid and 8 mM anthraquinone-2-sulfonate sodium salt (AQS) in Millipore double-distilled H_2O. The pH was adjusted with NaOH (98%, Sigma Aldrich) and measured with a Corning pH probe and meter. For experiments performed in D_2O (99.9%, Sigma Aldrich) the pD was adjusted with NaOD (99.9%, Sigma). The common amino acid analogs were used as received and consisted of L-methionine (99%, Sigma), N-acetyl L-methionine (99%, Sigma). The AQS (97%, Sigma) was recrystallized from ethanol/H_2O before use.

Synthesis of N-acetyl L-methionine-methyl-d_3. 1.00 g of L-methionine-methyl-d_3 (6.6 mmoles) was dissolved in 10 mL of acetic anhydride (80 mmoles) and 1 mL H_2O (55.5 moles) and reacted at 80 °C for 2 hours. 0.8 g of product (63 %) was purified by re-crystallization from ethyl acetate/hexane and characterized via NMR (D_2O): δ 1.95 (s, 3H), 2.05 (m, 2H), 2.47 (m, 2H), 4.36 (s, 1H). Close attention was paid to observing the shift of the α-proton w.r.t. that of L-methionine.

CHAPTER III

AMINO ACID AND PEPTIDE RADICALS FORMED BY ONE-ELECTRON OXIDATION

3.1 Introduction

As dicussed in the previous chapter, the oxidation of amino acid side chains via single electron transfer is a very important process that can have a major consequences for the degradation pathways of proteins. While studies of the oxidation hetero-atoms like sulfur and nitrogen are quite prevalent in the literature, the oxidation of more robust groups such as amide bonds, and carboxylates have not received as much scrutiny. This is somewhat suprising considering that these groups are much more commonly found in proteins and peptides they should be bigger targets for oxidation. Why then are they not studied more? One reason is that due to resonance stabilization of their lone pair electrons amide bonds and carboxylates are inherently more stable.[59] In order to study the mechanism of oxidation from either the amide bond or the carboxylate group, it is necessary to have an oxidant with a relatively high oxidation potential. TREPR can be a useful technique for the characterization of any radicals that are formed. Anthraquinone sulfonate salts serve as good oxidants for these studies. Which of the above mentioned groups are more susceptible to oxidation via electron transfer? Which radicals are formed in the process? These questions will be addressed in Chapter 3 which will focus on expanding the scope of the oxidation studies from methionine to dipeptides and their derivatives.

The glycine derivatives, N-acetylglycine and diglycine, are used here as model systems to examine the reactivities of the amine, amide bond, and carboxylate functionalities with ^{3}AQS*. These analogs are very soluble in water, relatively inexpensive, and derivatives of these compounds can be synthesized relatively easily. Scheme 3.1 shows several possible reaction pathways through which these derivatives can be oxidized. As mentioned above, this chemistry occurs in aqueous solution, and therefore pH has some effect on the possible

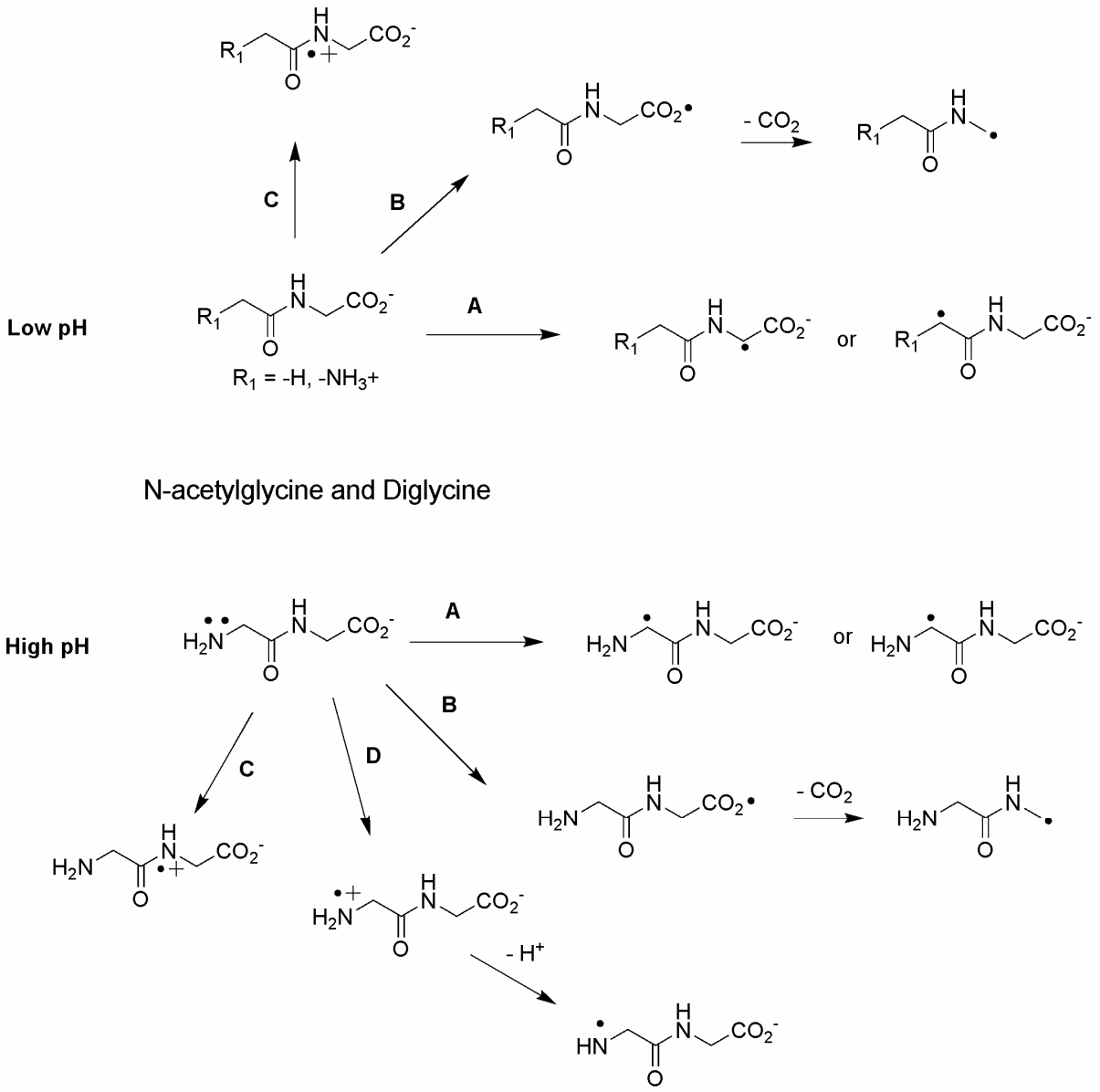

Scheme 3.1: Possible Oxidation Mechanisms for Glycine Derivatives

pathways. At pH < 2, both the C-, and N-termini are protonated. This effectively blocks the electron transfer pathways at either end of the diglycine, and the carboxylic acid of the N-acetylglycine, because the reactive lone pair electrons are converted to bonding electrons with H. This acidic pH will not be focused on in this discussion because no chemistry is observed under these experimental conditions. When the pH is in the neutral range, between pH 3 and pH 8, a majority of the C-termini of both analogs exist as the deprotonated carboxylate. At pH > 9, both the C-, and a majority of the N-termini of diglycine are deprotonated. Pathway A shows the pH independent H-abstraction from both the N-, and C-terminal α-carbons. This process has been shown to occur with the oxidation of glycine with ^{3}AQS*.[60] Pathway B shows the oxidation of the carboxylate group to form R–CO_2•. Which can rapidly decarboxylate.[61] Pathway C shows the amide bond oxidation pathway to form the amide radical cation. Due to the low lying energy of the resonance stabilized amide lone pair this pathway is the least probable. Pathway D is specific to the high pH case in which the amino terminus is deprotonated. The aminyl lone pair is very susceptible to oxidation by excited triplet anthraquinones. Deprotonation of the aminyl radical cation often occurs to form the more stable aminyl radical.

3.2 Results and Discussion

3.2.1 pH Dependence

Figure 3.1 shows TREPR spectra taken 500 ns after irradiation of an aqueous sample of diglycine and AQS with a 308 nm laser pulse. At pH 5.6 (Figure 3.1B) transitions attributed to two different radicals can be seen. Simulation of this spectrum (Figure 3.1A) yields magnetic parameters that are consistent with AQS^-• and the terminal alkyl radical, **3.1**.

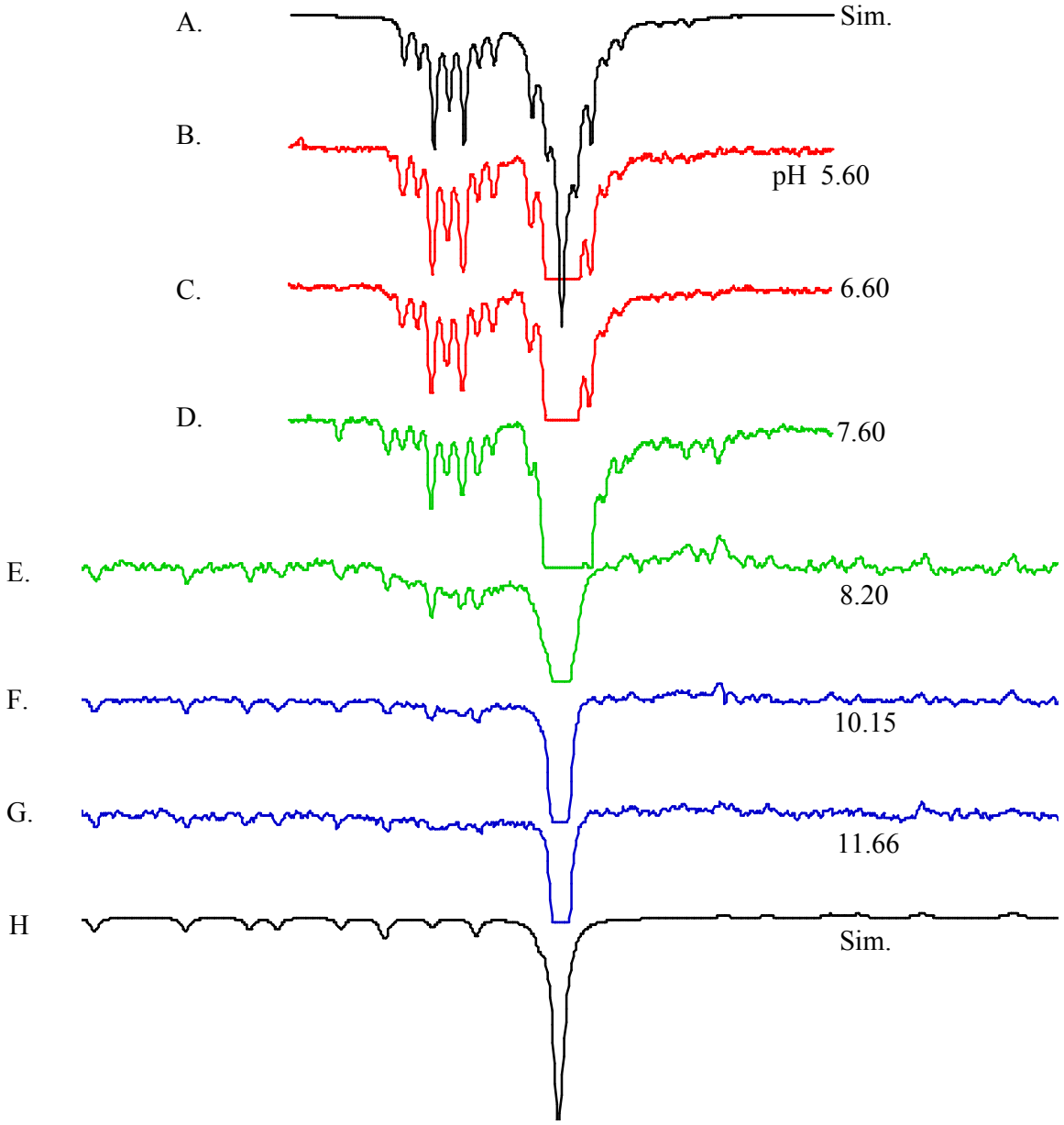

Figure 3.1: TREPR spectra taken 500 ns after irradiation of 0.2 M diglycine and 0.02 M AQDS in aqueous solution at various pH conditions. A and H are simulations of the pH 5.6 and 11.66, respectively.

The structure of radical **3.1** and all magnetic parameters used in the simulation are shown in Table 3.1. As discussed in chapter 2, the AQS^{-}• transition appears as an intense emissive peak polarized by TM. It is cut off in Figure 3.1 to show the radical **3.1** transitions more clearly. The spectral transitions attributed to radical **3.1** (and all radicals discussed in this chapter are polarized) by a superposition of RPM and TM CIDEP mechanisms. Upon decarboxylation of **3.1**, the radical is emissively polarized by TM. As the radicals diffuse in solution, $S\text{-}T_0$ mixing occurs and RPM is generated. The result is that the set of transitions downfield of the central AQS-• peak are in enhanced emission (E*) and the lines upfield are slightly absorptive, rendering the spectrum E*/A. The terminal radical **3.1** is formed upon oxidation of the carboxylate, and subsequent decarboxylation (Pathway B in Scheme 3.1). As the pH is increased, transitions from another radical grow into the spectrum (see Figure 3.1D). This radical, which completely takes the place of radical **3.1** in Figures 3.1E-G**,** shows the same AQS^{-}• signal along with single, symmetrically spaced lines. The computer simulation of these lines is shown in Figure 3.1H, and is consistent with an aminyl radical **3.2** formed via Pathway D in Scheme 3.1 Radicals **3.1** and **3.2** have been observed previously by Tarabek et al. through oxidation with the disulfonate derivative AQDS by Fourier transform TR-EPR.[44]

Although terminal radicals are generally unstable, **3.1** obtains considerable stabilization by conjugating with the planar amide bond π system. TREPR spectra can give information about how delocalized a radical is by the magnitude of the hyperfines. In the case of radical **3.1**, the protons on the α-carbon opposite the amide bond from where the radical is formed have a significant hyperfine coupling (4.0 G). The fact that the unpaired

electron is coupled to these protons (which are 3 bonds away) means it experiences some delocalization across the amide bond.

To further prove the that the aminyl radical is formed at high pH, the oxidation of diglycine was run in D_2O. As discussed in chapter 2, in D_2O at high pD, the protons are exchanged on the amine terminus for deuteriums. This changes the TREPR in the expected way (shown in Figure 3.2). Figure 3.2A shows the aminyl radical **3.2** transitions and the corresponding simulation. In D_2O, radical **3.3** is formed, the α-H is replaced with α-D, reducing the hyperfine by a factor of 6.5, and changing the spin of the nucleus to I = 1. Both radicals are shown in Table 3.1 with all magnetic parameters. The fact that the aminyl radical is formed in basic solutions where both the amine and carboxylate are available for electron transfer, means that the electron lone pair on the amine have a higher reduction potential than those on the oxygen. This is not surprising when the electronegativities of the two different atoms are taken into account.

To examine radical **3.1** in more detail when it is formed at neutral pH, glycine derivatives were oxidized under the same conditions. Figure 3.3 shows TREPR spectra taken upon oxidation of 4 different analogs: N-acetylglycine (NAG), N-acetylglycine-$^{13}C_2$ (NAG-^{13}C), N-acetyl-d_3-glycine (NAG-d_3), and Alanine-Glycine (Ala-Gly) dipeptide. Figures 3.3A and 3.3B shows the spectra and simulation obtained from oxidation of NAG to form **3.4**. All of the hyperfine splitting parameters are comparable to radical **3.1**, except for the fact that there are three protons on the opposite side of the amide bond, as opposed to two in the diglycine case. Figures 3.3C and 3.3D show the TREPR spectrum and simulation of the NAG-^{13}C radical analog, **3.5**. The ^{13}C nucleus has I = ½ and typical hyperfine coupling of ~35 G for radicals located directly on the nucleus. The spectrum therefore splits into a

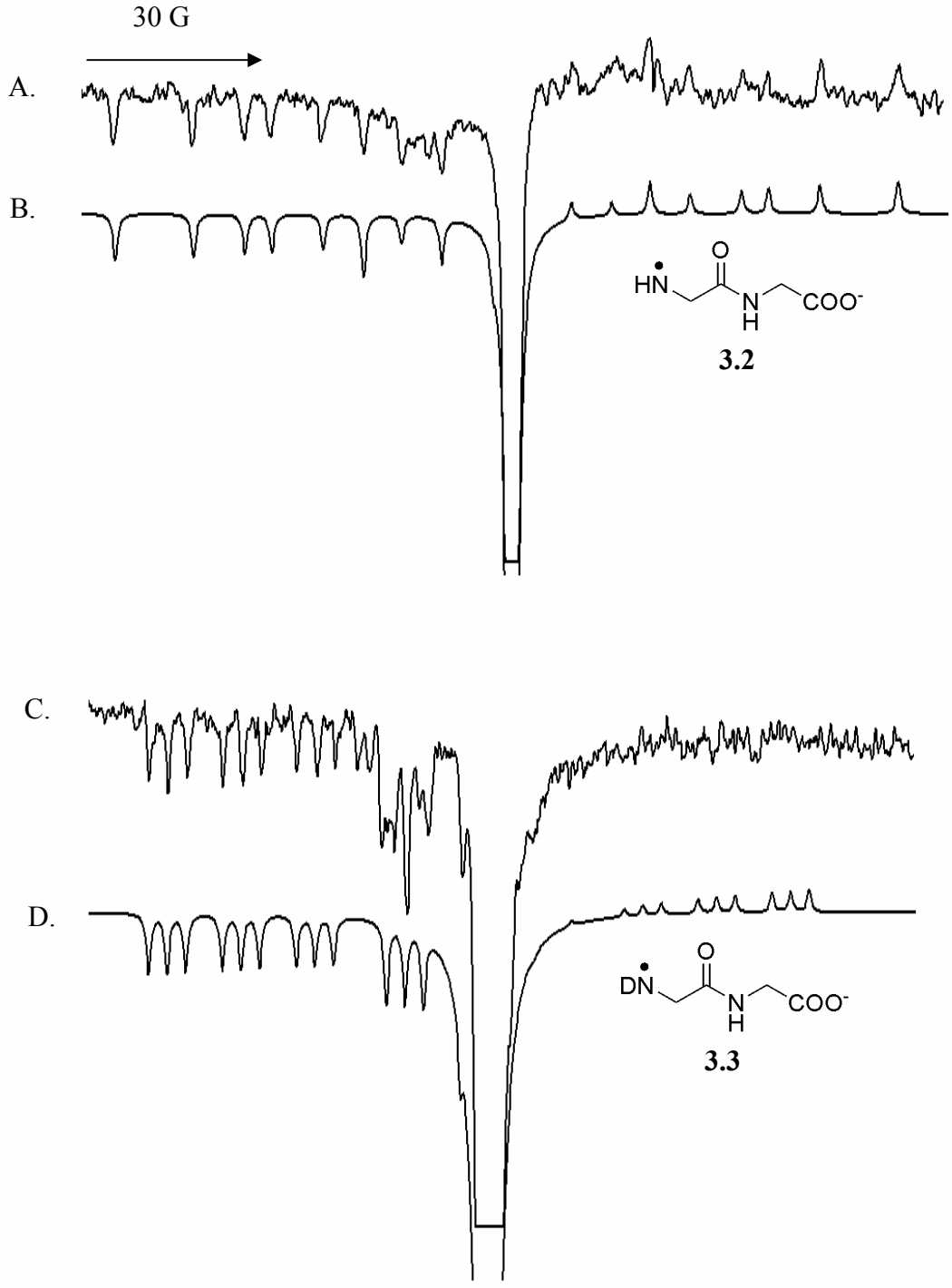

Figure 3.2: TREPR spectra taken 300 ns after irradiation of aqeuous solutions (pH (pD) 10) of 20 mM AQS and 200 mM GG in A) H_2O and C) D_2O. Simulations of each spectrum are shown in B, and D, respectively.

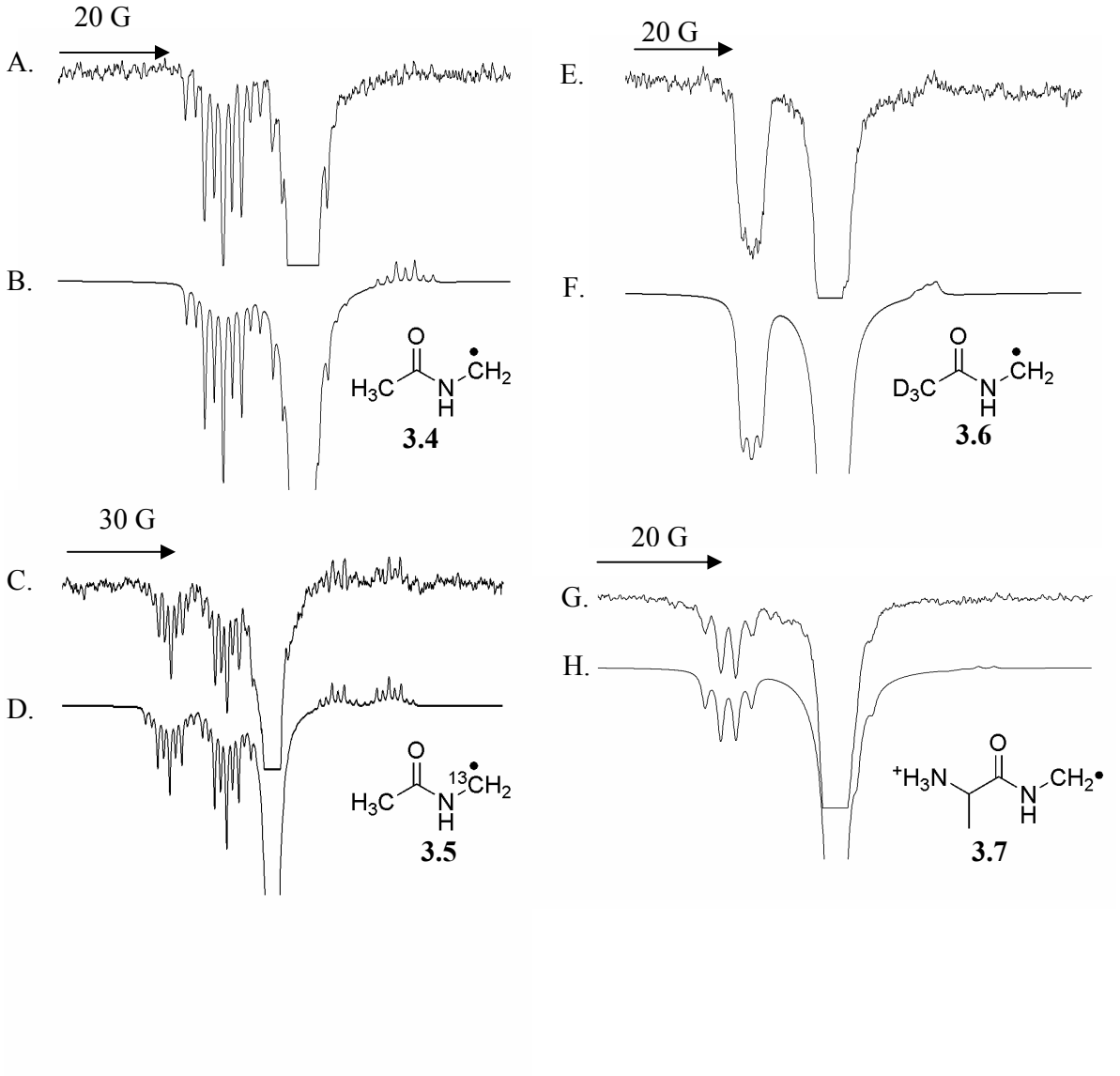

Figure 3.3: TREPR spectra taken 300 ns after irradiation of aqeuous solutions (pH 5.5) of 20 mM AQS and 200 mM A) NAG, C) NAG-^{13}C, D) NAG-d_3, G) L-Ala-Gly. Simulations of each spectrum are shown in B, D, F, and H, respectively.

doublet. This is proof that a large part of the radical spin density remains on C-terminal methylene carbon. The NAG-d_3 radical analog, **3.6,** shows the predicted spectral changes as deuteriums are substituted onto the acetyl group (Figure 3.3E and 3.3F). Figures 3.3G and 3.2H show the spectrum and simulation taken upon oxidation of L-Ala-Gly to form **3.7**. The hyperfine value on the proton opposite the amide bond does appear to decrease from 4 G to 2.5 G. This may be because of the planar structure that stabilizes these types of radicals has been perturbed. The stuctures and simulation parameters of all the radicals described in Figure 3.2 are listed in Table 3.1.

3.3 Conclusions

The radicals formed from oxidation of glycine amino acid and peptide radicals are characterized in this chapter and listed in Table 3.1. In low to neutral pH environments, the carboxlate termini of these species are oxidized. These radicals then decarboxylate to form stabilized α-amido methylene radicals. In high pH environments, the N-termini of these species are oxidized first and then deprotonate to yield neutral aminyl radicals.

3.4 Experimental

The TREPR data was obtained with the same spectrometer set up as described in Chapter 2. All of the aqueous samples were prepared with 200 mM amino acid and 20 mM anthraquinone-2-sulfonate sodium salt (AQS) in Millipore double-distilled H_2O. The pH was adjusted with NaOH (98%, Sigma Aldrich) and measured with a Corning pH probe and meter. For experiments performed in D_2O (99.9%, Sigma Aldrich), the pD was adjusted with

Radical	Structure	g factor	a-hcc	b-hcc	g-hcc
AQS-•	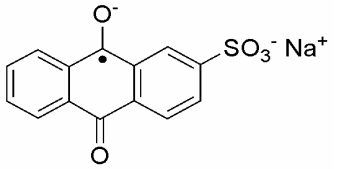	2.00398	< 1 G		
3.1	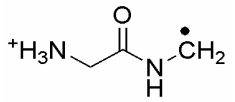	2.00292	18.80 (2H) 2.20 (N)		4.42 (2H)
3.2	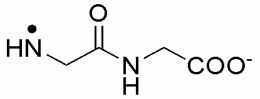	2.00392	22.35 (H) 13.50 (N)	42.80 (2H)	
3.3	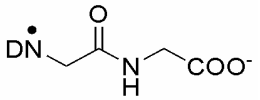	2.0039	13.60 (N) 3.7 (D)	43.40 (2H)	
3.4	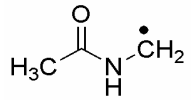	2.00282	19.05 (2H) 2.10 (N)		4.00 (3H)
3.5	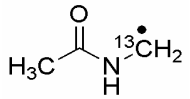	2.00202	35.3 (13C) 19.05 (2H) 2.1 (N)		4.00 (3H)
3.6	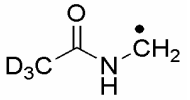	2.00282	19.05 (2H) 2.10 (N)		0.63 (3D)
3.7	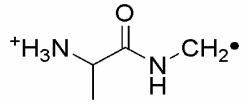	2.00272	19.0 (2H) 2.40 (N)		2.5 (H)

Table 3.1

NaOD (99.9%, Sigma). The common amino acid analogs were used as received and consisted of glycyl-glycine (99%, Sigma), N-acetylglycine(99%, Sigma). The AQS (97%, Sigma) was recrystallized from ethanol/H_2O before use.

Synthesis of NAG-d_3. 1.00 g of glycine (13.2 mmoles) was added to 6 mL of d_6-acetic anhydride (48 mmoles) with 1 mL of H_2O. After 1 hour of stirring at room temperature, 1.2 g, (75 % yield) of precipitated product was collected by suction filtration. The product was characterized by its solubility in MeOH (glycine is insoluble) and via ^{1}H NMR (D_2O): δ 4.45 (s, 2H).

CHAPTER IV

AMINO ACID AND PEPTIDE CARBON AND PEROXYL RADICALS FORMED BY H-ABSTRACTION BY HYDROXYL RADICAL

4.1. Introduction

Another important mechanism of protein oxidation is H-atom transfer. Certain by–products of cellular respiration, such as hydrogen peroxide and hydroxyl radicals, are known to oxidatively damage proteins and enzymes by this mechanism. [1] These reactions can lead to a number of unnatural and toxic protein responses such as loss of enzymatic activity and structure,[9] as well as fragmentation and aggregation.[8] It has also been shown that in the presence of oxygen, fragmentation of proteins is preferred, while in its absence, aggregation is more prevalent.[62] While there has been 30 years of EPR characterization performed on amino-acid, peptide, and protein radical intermediates formed by these processes, direct evidence for the primary steps in protein degradation remains elusive. The primary reason for this is that these reactions occur on a fast timescale, and many of the radical intermediates are oxygen centered. Oxygen centered radicals are notoriously difficult to observe due to there fast T_2 spin relaxation due to the oxygen nucleus. TREPR is a good technique to observe these radicals before this T_2 relaxation completely occurs. Protein systems are very complex and have many sites from which H-atom transfer to oxidants can occur. It is therefore advantageous to characterize simple, small molecule model systems and gradually increase in complexity.

In de-oxygenated solutions, the radicals produced after H-abstraction from amino acids and peptides have been studied via SSEPR using in both aqueous liquids and solid matrices.[43,63] In general, hydroxyl radicals are thought to be very reactive and un-selective towards various types of hydrogens attached to saturated alkanes. To determine exact reaction mechanisms it would be very advantageous to study these radicals via TREPR. While there have been numerous spin trapping studies perfomed on amino acid/•OH systems,

there have been relatively few which directly characterize the product radicals. For instance, Hawkins and Davies directly characterized the radicals formed from the aliphatic amino acids and peptides in presence of a steady state concentration of •OH. They found that the side chains were most reactive towards •OH attack, and α-hydrogens were absracted only in the case of glycine derivatives. In general the amine and carboxylate termini do not react with •OH. In these studies, the product radicals were detected on a relatively slow time-scale (40 μs), and the primary radical intermediates may not have been observed. It would be advantageous to study these very reactive systems on a faster time-scale, to determine if there are primary intermediates that are produced which were previously not detected by SSEPR. The first section of this chapter will present TREPR spectra of carbon-centered radicals from H-abstraction reactions involving •OH and amino acids and short peptides by •OH. In addition to characterization of the intermediates, the CIDEP polarization of the spectra will be analyzed to gain information about the spin-states of the radical precursors and the identity of the radical pairs.

The mechanism of hydroxyl radical attack on proteins and amino acids in oxygenated environments has been exhaustively reviewed and points to the formation of peroxyl adducts as key intermediates in main chain scission of proteins. [64-66] These adducts are formed by the reaction of O_2 with either the α–carbon radical on the main chain, or on carbon or sulfur radicals on side chains (Scheme 4.1). At ambient temperatures, peroxyl radicals have short chemical lifetimes in aqueous solution.[67] Previously they have been successfully only observed in frozen solutions in previous studies. While spin trapping techniques have been used to trap peroxyl radical adducts arising from radical reactions of amino acids and proteins,[68] these adducts have never been directly observed by EPR techniques in real time,

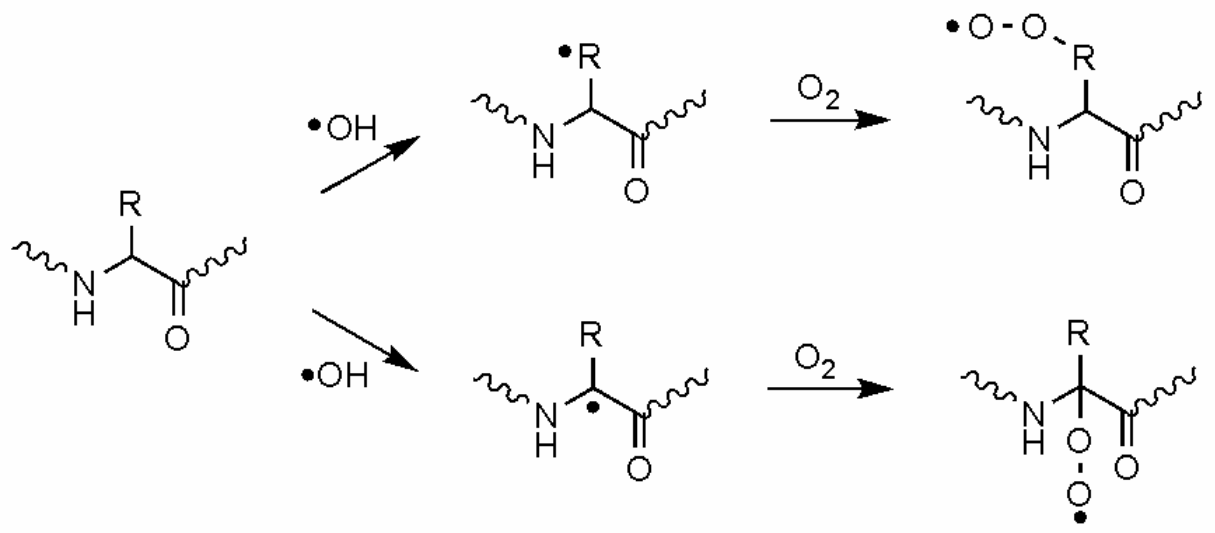

Scheme 4.1: Hydroxyl radical attack on peptide main and side chains and peroxylation by O_2.

in 100% aqueous solutions, at room temperature. It is highly desirable to work at conditions closer to physiological ones in order to draw better comparisons to biological systems.

This chapter will focus on the direct observation of amino acid and peptide radicals generated upon UV photolysis of hydrogen peroxide in deoxygenated and oxygen-saturated solutions via TREPR spectroscopy. In oxygenated solutions, the radicals may react with dissolved oxygen to form peroxyl radical adducts, which in turn can be detected using this technique. Unlike steady state spectra which rely on Boltzmann populations of spin levels, the phase and intensity of TREPR spectral transitions are affected by CIDEP mechanisms. The observed polarization patterns can yield mechanistic information about the origin of the radical pairs. Hydroxyl radicals, initially produced upon photolysis of hydrogen peroxide, have fast T_2 relaxation times and are typically not observable on the EPR timescale due to extremely broad linewidths. Fortunately, due to the their near diffusion controlled rate constants for H-abstraction,[18] they react to form carbon radicals before losing their initial polarization. This allows RPM to be generated as the carbon radicals diffuse in solution. In oxygenated solutions, the peroxyl radical signal obtains polarization strength from the parent carbon radical, making its observation facile at room temperature in real time.

4.2 Results and Discussion

4.2.1 Studies in De-Oxygenated Aqueous Solutions.

Diglycine. Figure 4.1 shows the TREPR spectra and simulation taken 0.5 μs after photolysis of H_2O_2 in the presence of diglycine. H_2O_2 is photolyzed by 248 nm light, and creates two equivalents of •OH which react with the diglycine through H-abstraction at the C-terminal α-

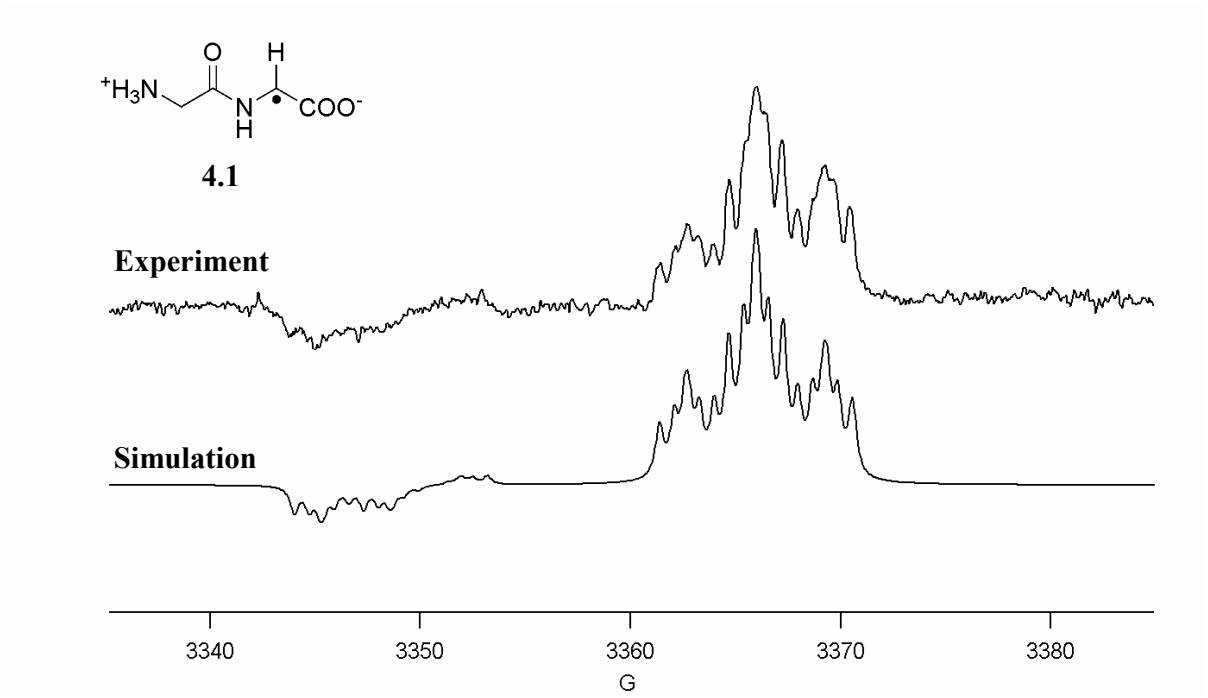

Figure 4.1: TREPR spectrum taken upon 500 ns after photolysis of 0.8 M H_2O_2 in the presence of 0.4 M diglycine at pH 5.5. Magnetic parameters used in the simulation are shown in Table 4.1.

carbon. The spectrum is attributed to the α-carbon radical **4.1**, the simulation of which is overlayed with the spectrum. The structure of **4.1**, and all radicals in this chapter are listed along with their magnetic parameters in Table 4.1. Radical **4.1** is stabilized by the hyperconjugative effect of both the neighboring amide and carboxylate groups.

The phases of the transitions in Figure 4.1 give information about the multiplicity (singlet or triplet) of the radical precursors, the identity of the radical pairs (geminate or F-pair), and the identity of the counter-radicals. The original radical pair consists of two hydroxyl radicals generated from the excited singlet state of H_2O_2, which would, according to Kaptein's rules for CIDEP,[69] give geminate polarization that is A/E. However, hydroxyl radicals react at near diffusion controlled rates and have fast electron spin relaxation, therefore this geminate pair CIDEP would be difficult to observe. The E/A pattern observed in the spectra in Figure 4.1 must be generated in random or so–called F–pairs ("free pairs). These F-pairs form when the original radicals diffuse away from their original partners and come into contact with other radicals. This process is outlined in Scheme 4.2. In this case, once this diffusion process occurs, •OH can react with diglycine to form **4.1**. This radical has no geminate counter-radical because the formation of **4.1** is a propagation process yielding H_2O as a biproduct. Over a few tens to hundreds of nanoseconds, radical **4.1** will then come into contact with other radicals in solution and form F-pairs with E/A RPM polarization as discussed in Chapter 1. There are two different counter-radicals with which F-pair formation can occur: **4.1**, and •OH. The observed spectra should reflect both situations: F-pairs formation between two **4.1** carbon radicals, and a radical pair consisting of **4.1** and •OH. This is exactly what is observed in the spectral simulation in Figure 4.1, a superposition of the two radical pairs.

Substrate	Radical	Structure	g-factor	Hyperfine Coupling Constants (G)			Simulation Linewidth (G)
				alpha-H(D) (G)	beta-H (G)	Other (G)	
Diglycine	**4.1**	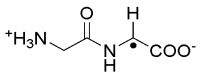	2.0029	17.4	1.2 (H_N)	3.3 (2H) 0.7 (N)	1.1
Alanine	**4.2**	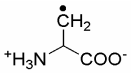	2.0032	22.2	26.1	3.5 (N)	1.2
Valine	**4.3**	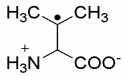	2.0026	23.6	6.3	7.35	1.2
Valine	**4.4**	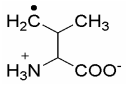	2.0026	22.2	29.8 (2H)		1.1
Serine	**4.5**	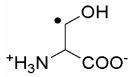	2.0029	17.7	9.8	7.59 (N) 1.0 (H_O)	1.2
Threonine	**4.6**	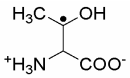	2.0029	31.4 (3H)	31.4 (3H) 12.1	10.0 (N)	1.1
Methionine	**4.7**	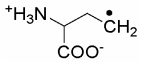	2.0027	22.4 (2H)	25, 25.7		1.2
Methionine	**4.8**		2.0026	22.8 (3H)			1.2
Methionine-^{13}C(2)	**4.8-^{13}C**		2.0026	22.4 (3H)		39.3 (^{13}C)	1.2
Methionine-d_3	**4.8-d_3**		2.0026	3.5 (3D)			1.1
N-acetyl Glycine	**4.9**	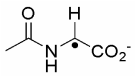	2.0027	17.5	1.3 (H_N)	2.6(3 H) 0.4 (N)	1.2
N-acetyl Glycine-2,2-d_2	**4.9-d**	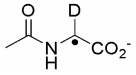	2.0027	2.8 (D)	1.3 (H_N)	2.6 (3 H) 0.4 (N)	5.9
N-acetyl Glycine	**4.10**	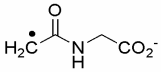	2.0024	20.9		2.7 (NH) 2.5 (N)	1.2

Table 4.1

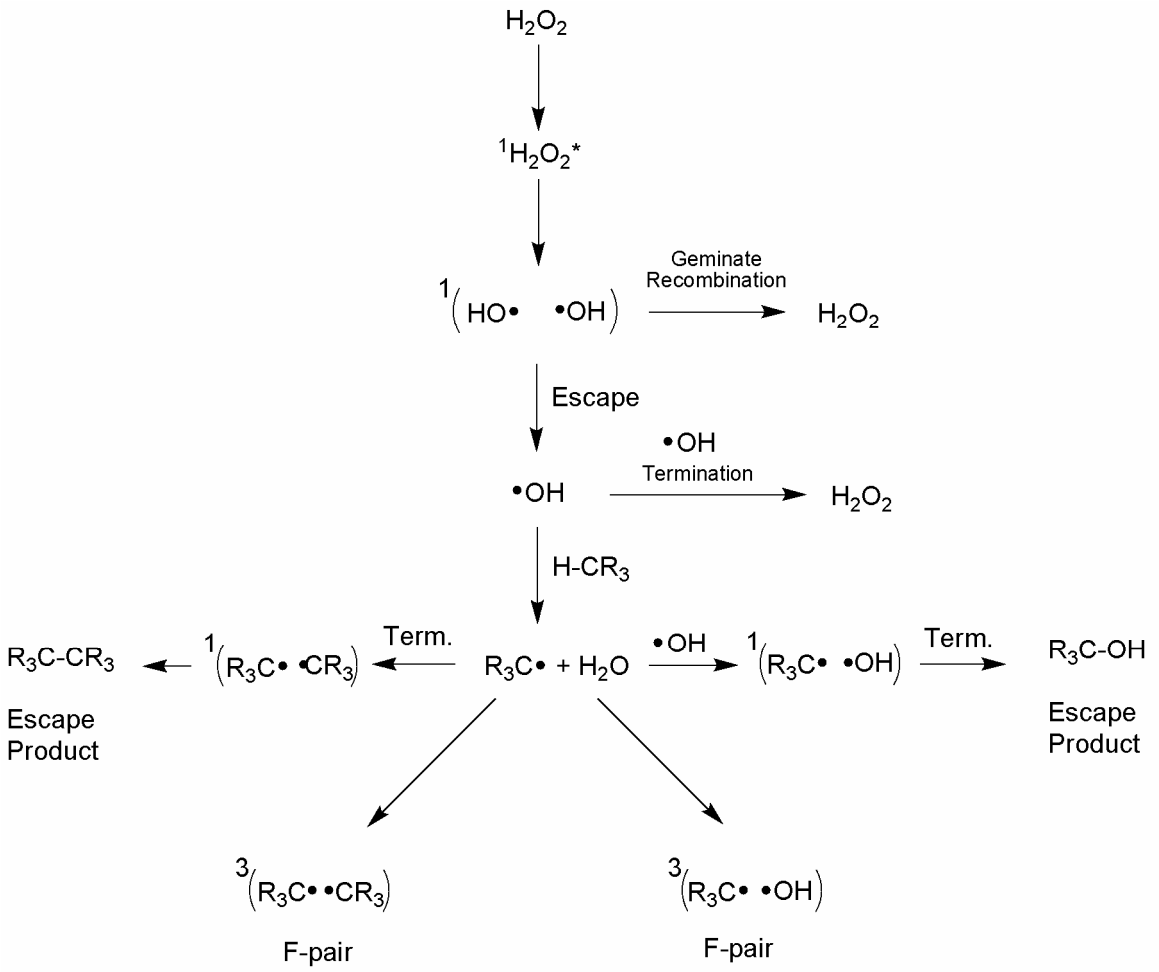

Scheme 4.2: Formation of F-pairs upon photolysis of hydrogen peroxide

This combination of 2 F-pair spectra to make a new spectrum has not been proposed previously. This E/A* CIDEP pattern was first observed by Paul and Fischer in TREPR of the oxidation of glycine by •OH.[70] They explained this anamolous intensity pattern was generated from spin-selective reactions of the observed carbon radical with H_2O_2 to form a carbocation center. The radicals at lowest field react to form diamagnetic products faster than those at higher field. This reaction would however be considerably energetically unfavorable as radicals are not considered good lewis bases. At the time this explanation was proposed, the concept of F-pairs observed in radical studies was novel and this situation does not appear to be considered in this previous work. In the few other publications showing CIDEP of carbon radicals generated with •OH, this same anamolous intensity pattern presents itself.

Figure 4.2A shows the spectral simulation of the F-pair formed between two identical **4.1** radicals. The difference in the g-factors, Δg, is 0 and hence the low and high field lines are equally polarized in E and the A, respectively. Figure 4.2B shows the spectral simulation of an F-pair formed between radical **4.1** and •OH. In this case there is a relatively large Δg (2.011 for •OH – 2.0029 for radical **4.1** = 0.008) and all of the transitions of radical **4.1** are absorptively polarized because they are all located upfield of the •OH. The hydroxyl radical is not observed due to its fast relaxation. Once these two spectra are added together, the low field lines effectively cancel out, and the observed spectral intensities are obtained. In order to determine if this CIDEP phenomenon is specific to a certain radical type, and to compare TREPR spectral data to that of SSEPR, other amino acids were oxidized.

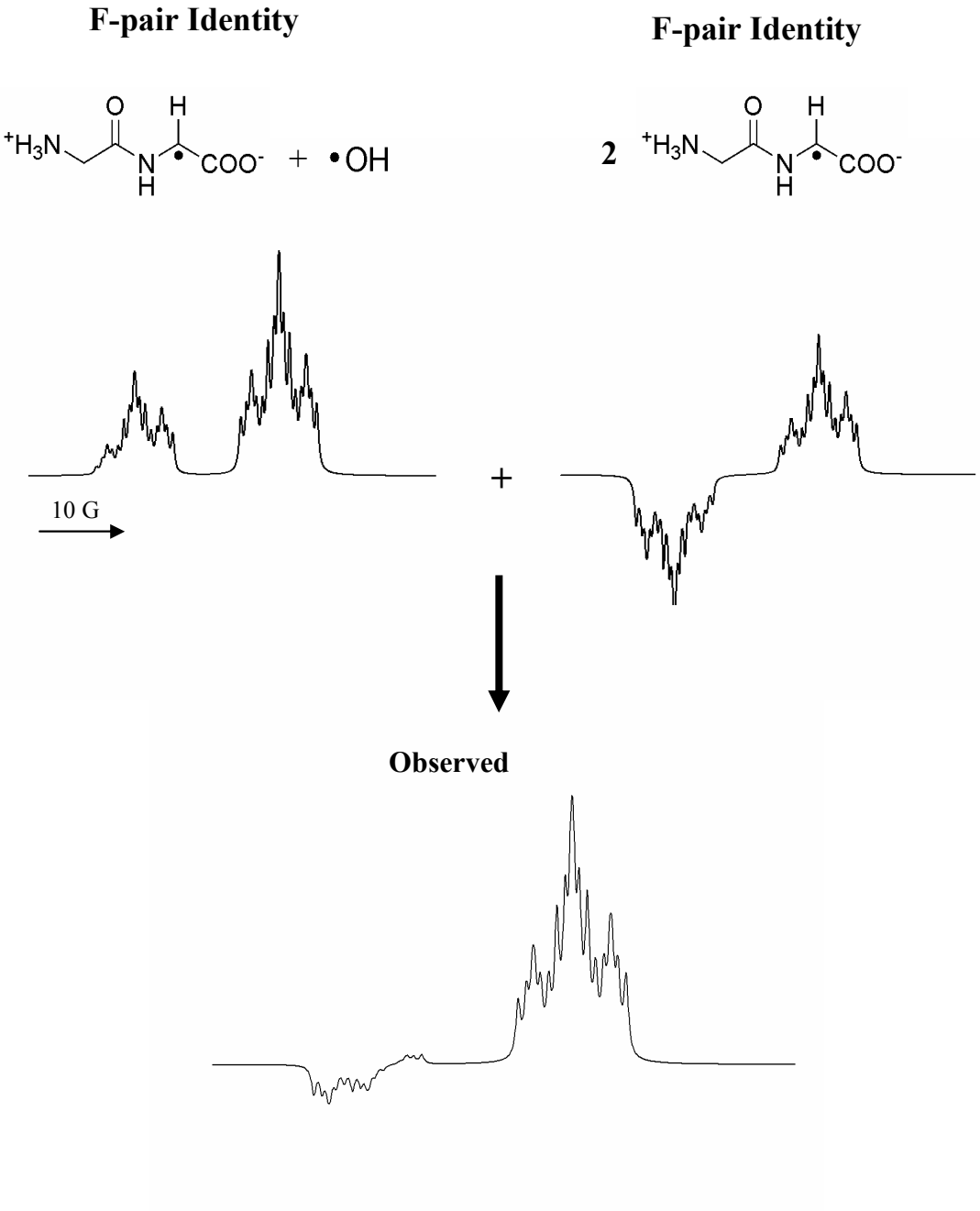

Figure 4.2: Combination of 2 F-pair spectra

Alanine and Valine. Figure 4.3A shows the TREPR spectrum attributed to the terminal methylene radical **4.2** generated upon H-abstraction from the methyl group on L-Alanine. Figure 4.3B shows the radicals which are obtained upon H-abstraction from L-Valine. The peaks are assigned to radical **4.3** (formed upon H-abstraction from the C(3) carbon) and radical **4.4** (formed from abstraction from C(4) carbon). The spectra are generated by the same method used in the diglycine case, addition of the two F-pair spectra. In the case of valine, 4 total spectra were added together, 2 for the **4.3** case, and 2 for the **4.4** case. These identity of the radicals are in agreement with previous EPR characaterization data by other groups.[43,71] Figures 4.4A and 4.4B show TREPR spectra generated upon H-abstraction from amino acid analogs, L-Serine and L-Threonine, respectively. The purpose of this experiment was to test the CIDEP polarization for radicals with neighboring hydroxyl groups. The generated radicals, **4.5** in the serine case, and **4.6** in the threonine case, suggest that the hydroxyl group greatly stabilizes the radical centers via hyperconjugation. This is in line with reports from other laboratories. Neighboring heteroatoms with lone pairs can in general stabilize electron deficient carbon centers, similar to that observed for carbocations.

Methionine. As discussed in Chapter 2, the oxidation of methionine is thought to one of the primary steps towards the development of plaque formation in Alzheimer's Disease. While the oxidation of methionine via electron transfer to form Met+• was investigated in Chapter 2, its oxidation by •OH has not been investigated by TREPR to date. The only EPR work that has been performed on the oxidation of methionine by H_2O_2/•OH species have been trapping studies. While species such as methyl radicals and terminal methylene radicals have been trapped by spin-traps, these radicals have not been observed directly in solution at room

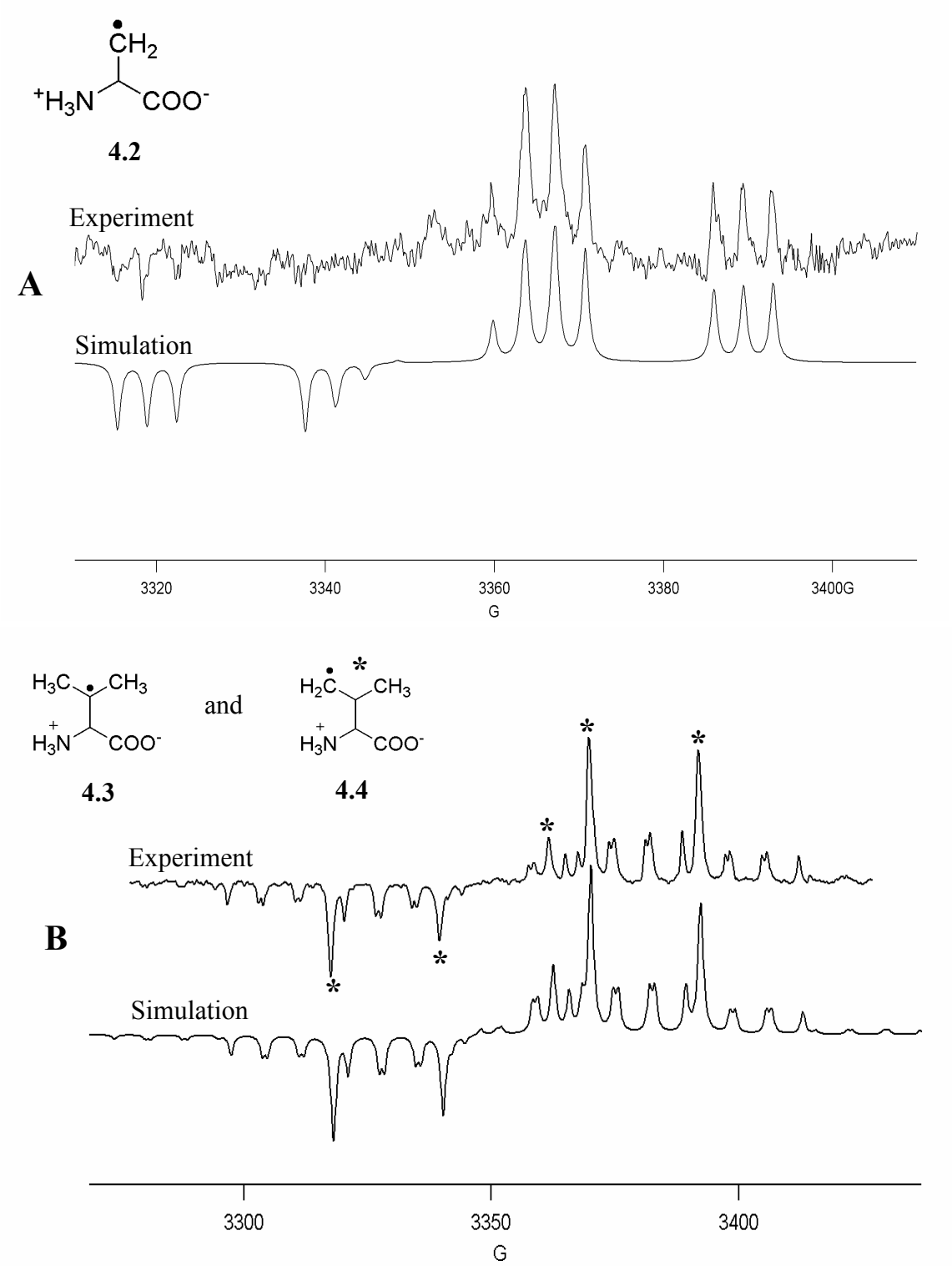

Figure 4.3: TREPR spectra taken upon 500 ns after photolysis of 0.8 M H_2O_2 in the presence of 0.4 M A) L-Alanine and B) L-Valine. Corresponding magnetic parameters used in simulation are shown in Table 4.1.

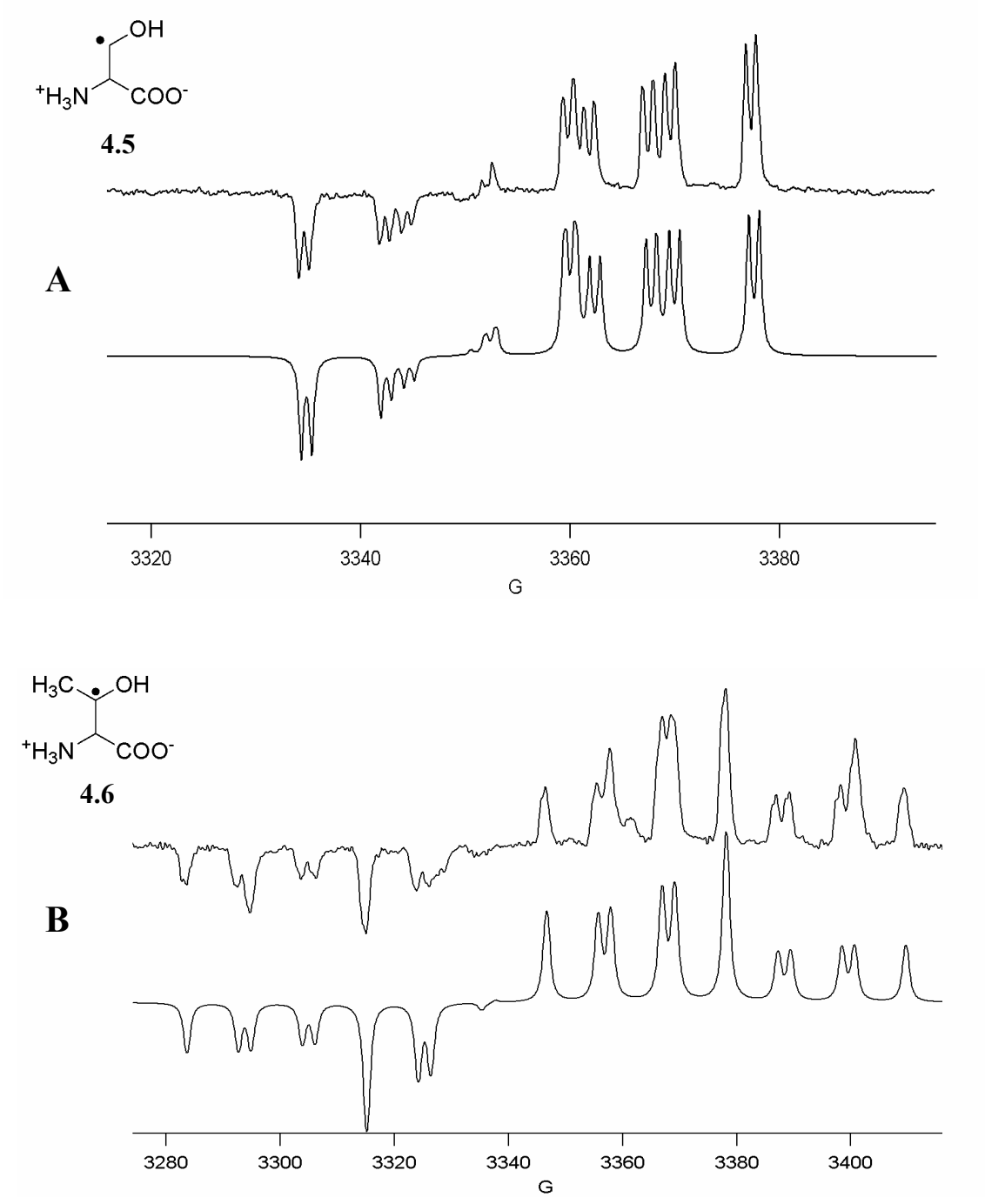

Figure 4.4: TREPR spectra taken upon 500 ns after photolysis of 0.8 M H_2O_2 in the presence of 0.4 M A) L-Serine and B) L-Threonine. Corresponding magnetic parameters used in simulations are shown in Table 4.1.

temperature. The data in this section represents the first experiments performed upon direct observation of radicals created upon oxidation by H_2O_2 and •OH.

Figure 4.5A shows the experimental spectrum and simulation obtained 500 ns after irradiation of a solution of H_2O_2 and L-methionine in de-oxygenated aqueous solution. Two radicals are observed and simulated in the spectrum: a terminal methylene radical, **4.7**, and a methyl radical, **4.8**. To confirm the identies of these species, the same experiments were run with the isotopic analogs L-methionine-^{13}C and L-methionine-d_3. Figure 4.6A shows the TREPR spectra and simulations generated from the ^{13}C analog radicals **4.8-^{13}C** and **4.8-d_3**. It is expected that if the •CH_3radical is located on the ^{13}C center, the normal quartet should be split into a doublet of quartets. This is exactly what is observed, the peaks of the •$^{13}CH_3$ are labeled accordingly. The deuterated analog also shows the expected change in hyperfine splitting shown in Figure 4.6B. The α-protons are changed to α-deuteriums and the hyperfine coupling constants changed accordingly. In previous SSEPR work, these radicals have been spin-trapped and it was suggested that H-abstraction from methionine is not the primary chemical step in this photochemistry. The proposed oxidation mechanism is shown in Scheme 4.3. The methionine sulfur atom is known to react with H_2O_2 to produce a sulfoxide. The hydroxyl radical then adds to sulfoxide sulfur to create a hydroxy-sulfoxyl radical which can eliminate to form either **4.7** or **4.8**.

4.2.2 Oxygenated Solution: Direct Observation of Peroxyl Adducts

N-acetylglycine. Figure 4.7A is the spectrum obtained upon photolysis of H_2O_2 in the presence of NAG in a de-oxygenated environment. The spectrum is assigned to the α–carbon radical **4.9**. Parameters obtained from computer simulation of this spectrum agree

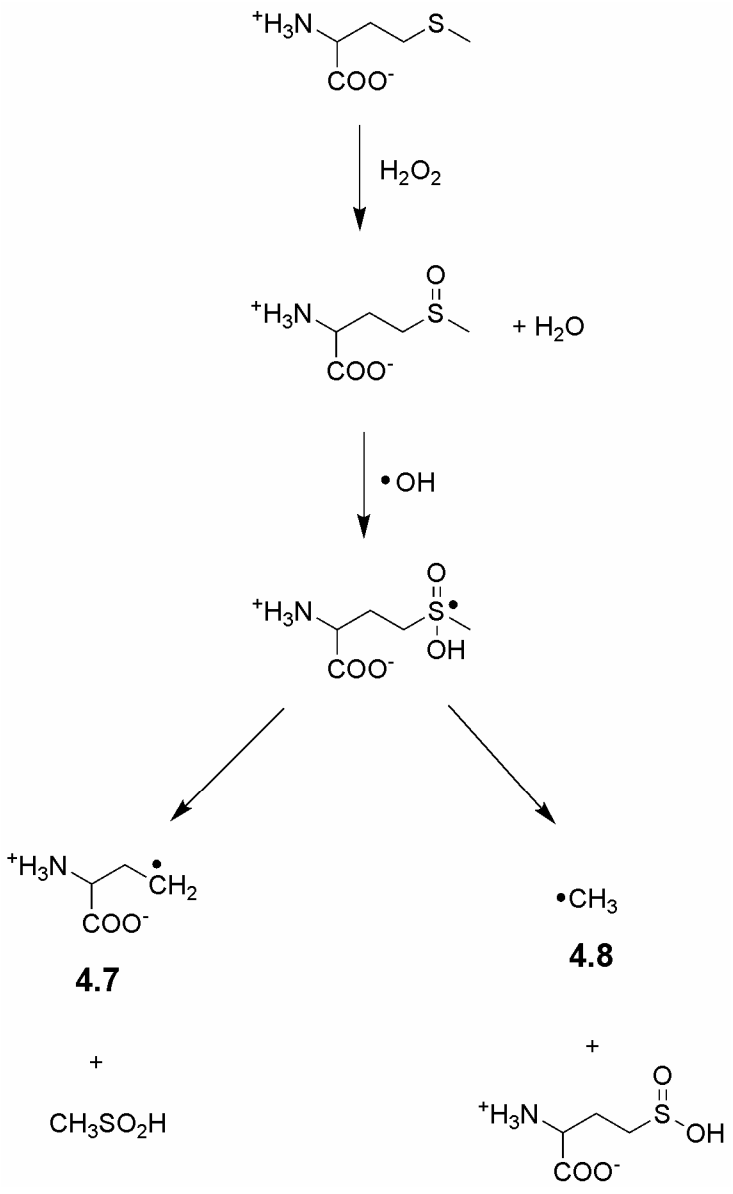

Scheme 4.3: Oxidation of methionine by H_2O_2 and hydroxyl radical.

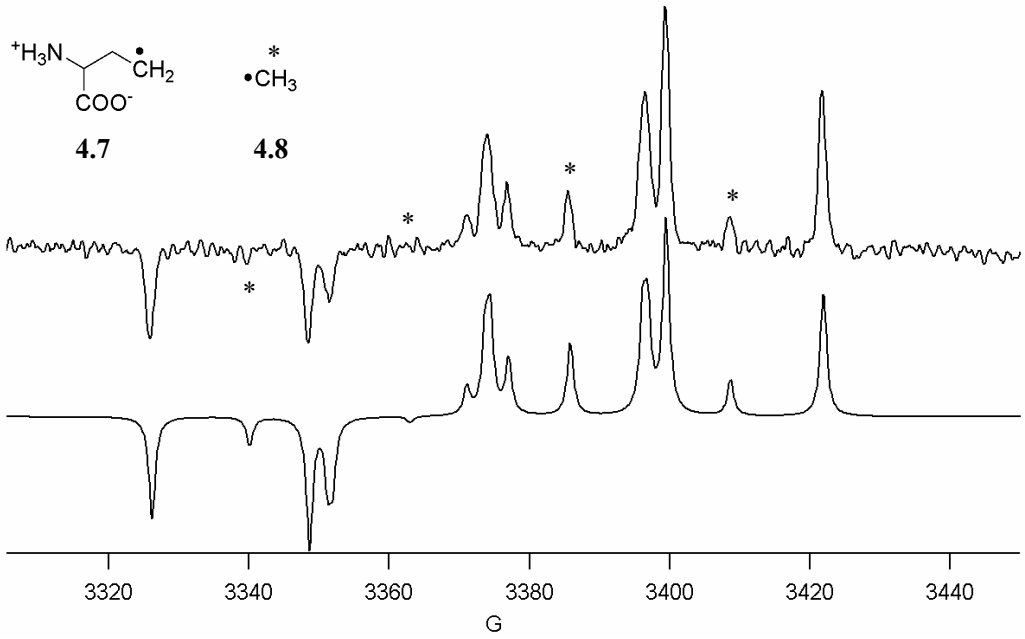

Figure 4.5: TREPR spectra taken upon 500 ns after photolysis of 0.8 M H_2O_2 in the presence of 0.4 M L-methionine. Corresponding magnetic parameters used in simulation are shown in Table 4.1.

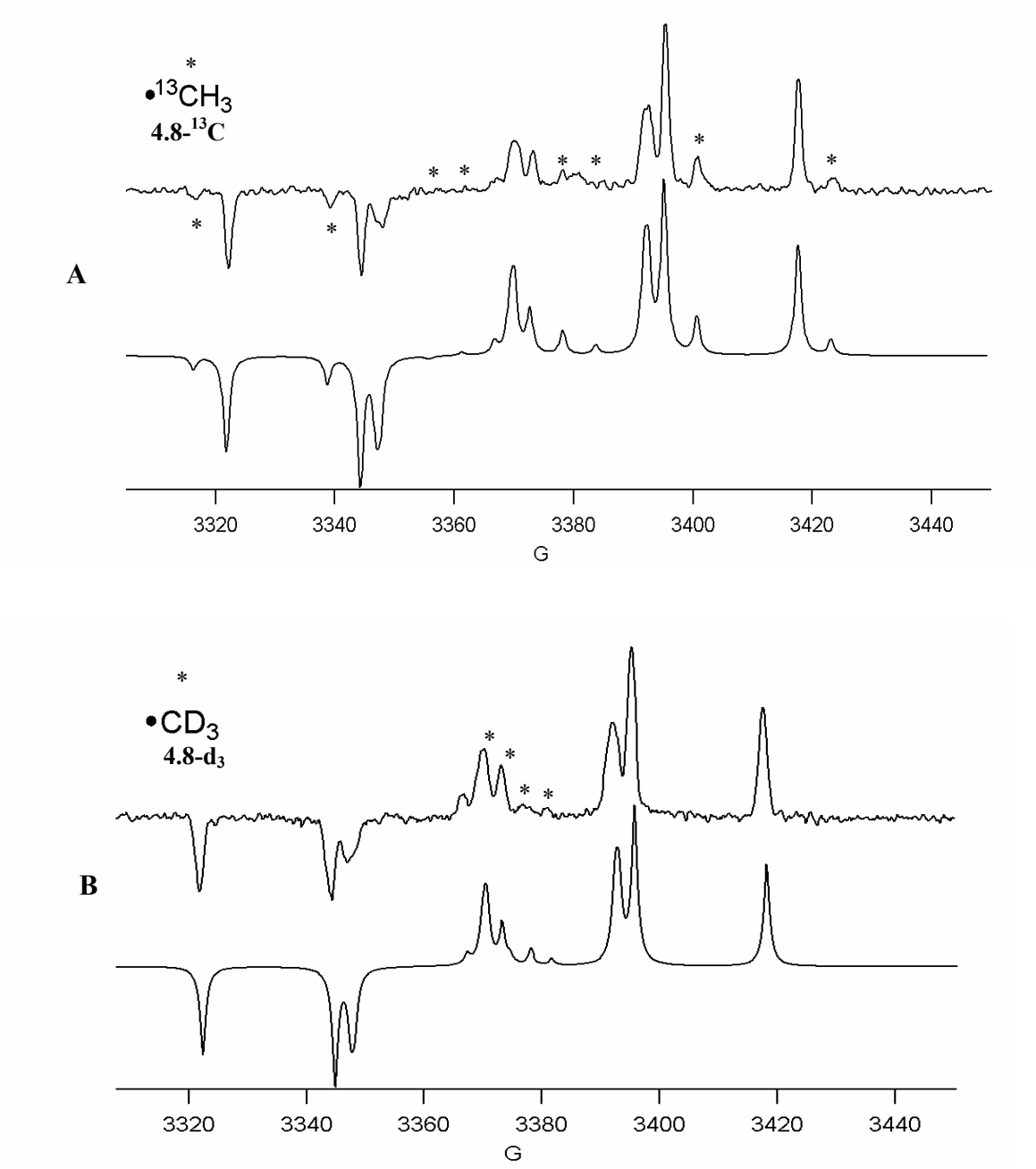

Figure 4.6: TREPR spectra taken upon 500 ns after photolysis of 0.8 M H2O2 in the presence of 0.4 M A) L-methionine-13C and B) L-methionine-d3. Corresponding magnetic parameters used in simulation are shown in Table 4.1.

with those obtained by Neta and Fessenden[43] and Hawkins and Davies.[71] A small signal corresponding to radical **4.10** is also observed. Both of these radicals are formed by H–abstraction and are stabilized by adjacent carbonyl groups. Figure 4.6B shows spectra taken upon irradiation of aqueous H_2O_2/NAG solutions that have been oxygen–saturated. A broad signal appears at low field, while the transitions due to radical **4.9** have disappeared completely. The broad signal has a g–factor of 2.0130, consistent with known literature values for peroxyl radicals.[72] To confirm that we are observing the peroxyl–NAG radical adduct and not •OOH or another transient species, the same experiment was run with isotopically–substituted N–acetyl glycine–2,2–d_2 (NAG–d_2) in both de–oxygenated (Figure 4.6C) and oxygenated (Figure 4.6D) conditions. Under N_2, radical **4.9-d**, the deuterated analog of **4.9,** is formed. The linewidth of the peroxyl radical in Figure 4.6D is noticeably smaller than in the protonated case shown in Figure 4.5B. This narrowing of the linewidth occurs because the largest hyperfine coupling constant has been changed from H to D by a factor of 6.5. The broad transitions observed in Figures 4.5B and 4.5D are therefore assigned to peroxyl radical adducts **4.11** and **4.11-d,** respectively. The magnetic parameters used to simulate these and all peroxyl adduct radicals are shown in Table 4.2. Line-widths of 5.9 Gauss for both **4.11** and **4.11-d**, as well as a respective hyperfine interactions of 4.0 G, and 0.6 G, were used in the simulations. These hyperfine values are comparable with those found previously for peroxyl adducts observed in polar non-aqueous solvents via steady-state techniques.[72,73] The absorptive CIDEP observed in peroxyl radicals **4.11** and **4.11-d** can be explained by polarization transfer. Because the polarization of the TREPR signal is inherited directly from the carbon parent radical, and the net polarization of the carbon radicals are

Substrate	Radical	Structure	g-factor	alpha-H(D) hcc (G)	Simulation Linewidth (G)
N-acetyl Glycine	**4.11**	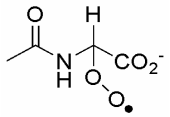	2.0130	4.0	5.9
N-acetyl Glycine-2,2-d_2	**4.11-d**	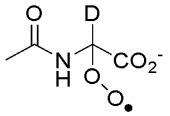	2.0138	0.6 (D)	5.9
Serine	**4.12**	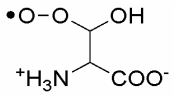	2.0146	4.0	5
Diglycine	**4.13**	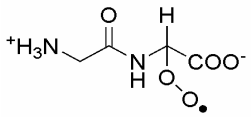	2.0138	4.0	4.7

Table 4.2

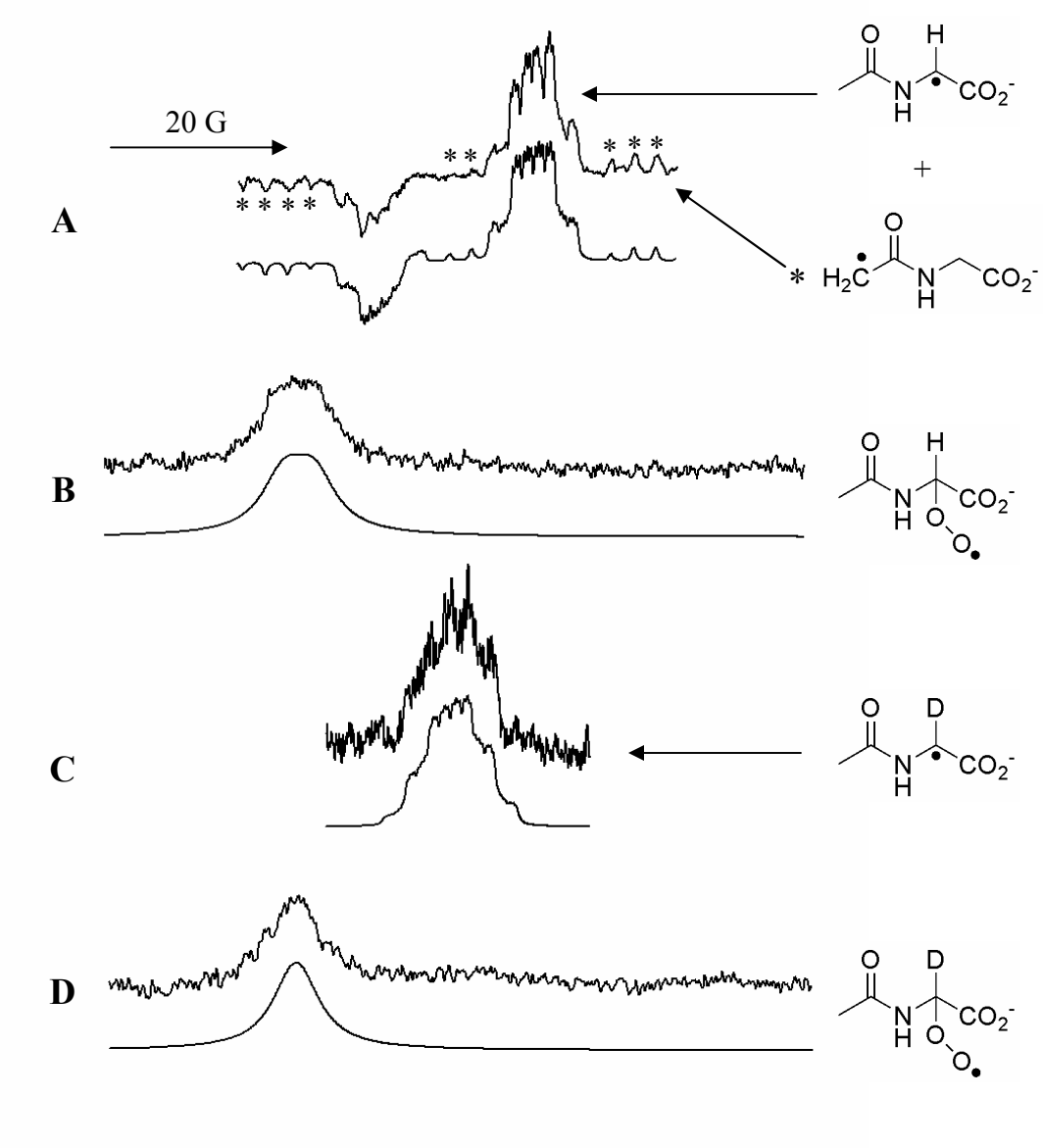

Figure 4.7: TREPR spectra taken upon 248 nm laser irradiation (1 μs delay) of aqueous solutions (pH 5.5) of 0.8 M H_2O_2 and: 0.4 M NAG in A) de–oxygenated and B) oxygenated solutions, 0.1 M NAG–d2 solution in C) de–oxygenated solution and D) oxygenated solutions with simulations.

absorptive (E plus enhanced A = overall A), the peroxyl radicals will show net A polarization.

Serine and Diglycine. When glycine was used as a substrate, no signal was observed in deoxygenated or oxygenated solutions, though α–carbon radicals from this substrate have been observed via SSEPR at ambient temperatures.[43,71] The ^{17}O peroxyl adduct of alanine has been characterized via steady–state conditions in frozen aqueous solution by Sevilla et al.[74] When we ran the TREPR experiment with H_2O_2 and alanine, we observed the C(3) primary radical under deoxygenated solution. When the same experiment was run in oxygen saturated solutions, the peroxyl radical signal was not directly observed. However, the intensity of the signal from the carbon parent radical was reduced in the presence of oxygen. It is possible that for these cases the reaction with O_2 is too slow to allow for polarization transfer, or that recombination of the F–pairs is fast. Spectra and simulations for the serine and glycyl–glycine systems are shown in Figure 4.8. The spectrum shown in Figure 4.8A shows two different radicals, the serine C(3) carbon parent radical **4.12** and the peroxyl radical adduct **4.13**. Radical **4.12** has been observed by Behrens and Koltzenburg in aqueous solution[63] and the magnetic parameters used in the simulation in Figure 4.8A are similar. The intensity of the transition due to **4.13** is greatest at 1.5 μs. Because both radicals are seen in solution at the same time delay means that the concentraton of **4.12** is greater than the concentration of O_2 and oxygen is the limiting reactant to form **4.13**. There is also a significant g-factor difference between radicals **4.11**, **4.12**, and **4.13**. Radical **4.12** has the highest g-factor due to the close proximity of the electronegative hydroxyl group. The glycine analog radicals **4.11** and **4.13** do not any appreciable difference in the g-factors. This

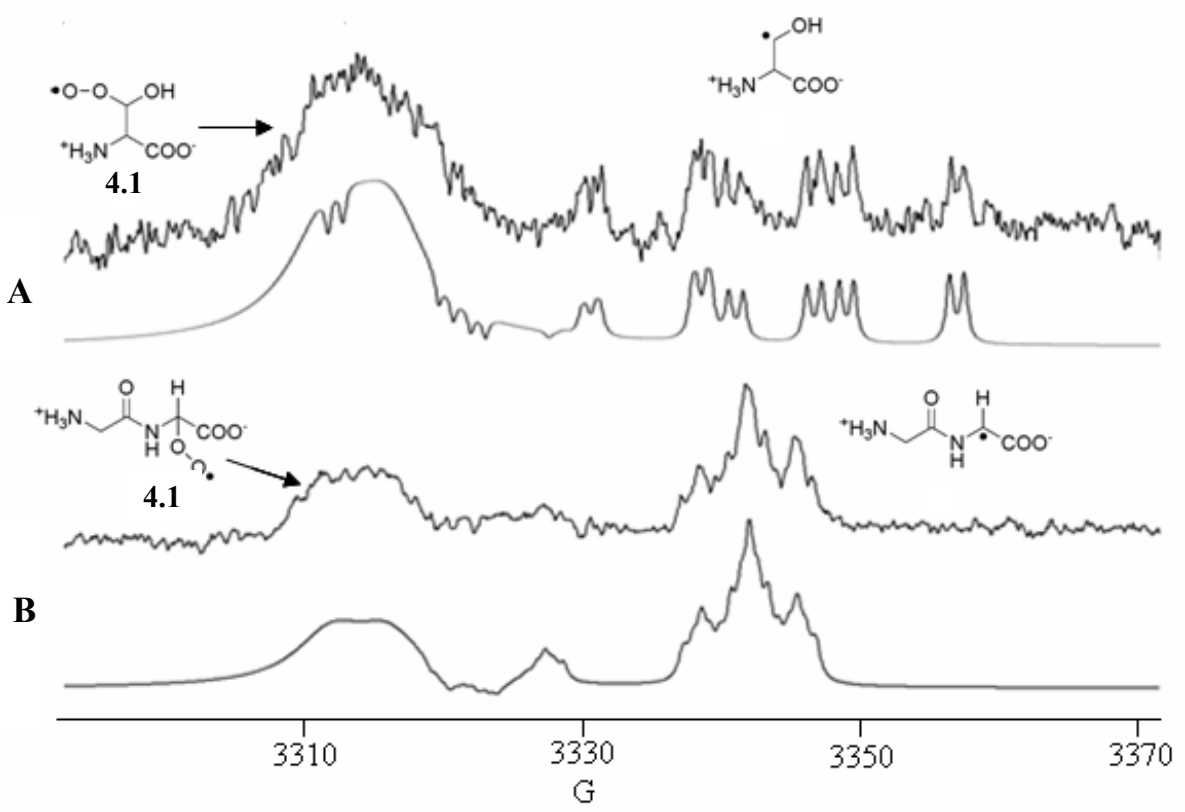

Figure 4.8: TREPR spectra taken upon 248 nm laser irradiation of oxygenated aqueous solutions (pH 5.5) of 0.8 M H_2O_2 and 0.4 M: A) L-serine and B) diglycine solutions with simulations.

means that the positive ammonium group does not appear to have any inductive effect on the peroxyl radical.

At time delays less than 1.5 μs, the peak intensity attributed to the peroxyl radical is found to grow with time as the intensities of the carbon parent radicals decrease. Figure 4.9 shows the serine TREPR spectra taken at different time delays. The intensity of the peroxyl radical transition visibly increases with the time delay, while the intensity of the carbon radical peaks do the opposite. The fact that these two signals are inversely proportional suggests that under these experimental conditions, that these signals are directly proportional to radical concentration and can be used to determine the rates of oxygen additon to the carbon parent radicals. In order to perform more quantitative measurements the rise time of the peroxyl radicals must be analyzed. From the qualitative picture shown in Figure 4.9 though, it can be concluded that the peroxyl radical forms directly by addition to the carbon radical and that at these concentrations this process happens on the timesecale of the experiment.

Diglycine was also tested under these experimental conditions to examine the effect of a protonated ammonium N–terminus on the formation of the peroxyl adduct. Figure 4.8B show the spectrum and computer simulation. The spectrum is similar to the serine case in which the both the α–carbon (**4.5**) and peroxyl adduct (**4.9**) radicals are observed. Hawkins and Davies reported that the majority (90%) of •OH attack occurs on the α–carbon neighboring the carboxylate group.[71] This is indeed the only observed radical. It can be assumed that the observed peroxyl radical peak is attributed to the peroxyl radical adduct at this site.

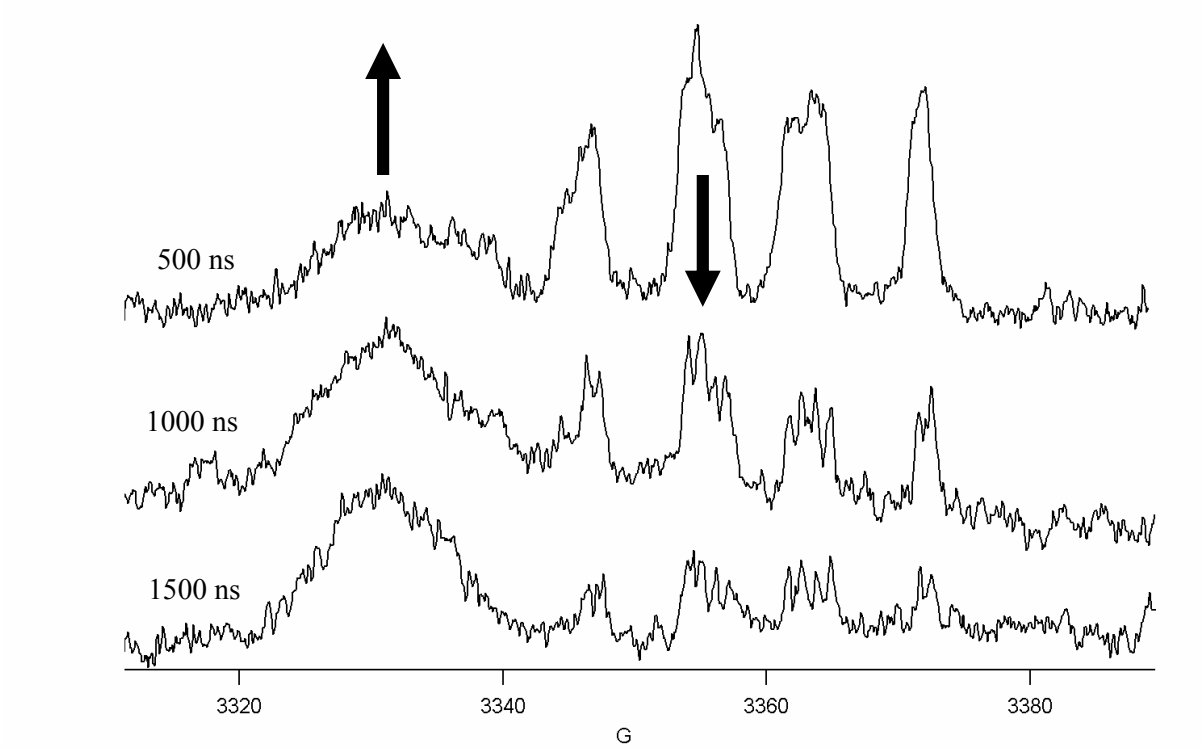

Figure 4.9: Time-dependence of TREPR taken upon irradiation of 0.8 M H_2O_2 and 0.4 M L-serine in aqueous solution at pH 5.5.

4.3 Conclusions and Outlook

The reactions of NAG, alanine, serine, threonine, and diglycine with •OH in the presence of oxygen are summed up in Scheme 4.4. Methionine reacts thermally with H_2O_2 and this chemistry is shown in Scheme 4.3. These reactions show significant spin polarization of carbon and peroxyl radicals in room temperature solutions and provide a new avenue for study of an important class of reactive intermediate. The RPM polarization generated in the carbon radicals allow for characterization on the sub-microsecond timescale. Due to E/A* signal intensities of carbon radicals, enough A polarization is transferred to the peroxyl radical so that it can be observed. Because peroxyl radicals have g–factors that are quite different from carbon–centered radicals, they are easy to identify and extension of this chemistry to short peptides and proteins under physiological conditions should be possible. It is also important to note that this method of generating peroxyl radicals avoids the presence or generation of singlet oxygen, which often complicates such photochemistry. In future studies the rate information will be extracted from this experiment by monitoring the kinetics of the transitions from each species.

4.4 Experimental

Preparation of H_2O_2 Solutions. All TREPR experiments were performed in aqueous solutions at pH 5.5. Except where noted the amino acid and peptide concentration was 0.4 M and the H_2O_2 concentration was 10% or 0.8 M. The hydroxyl radicals were generated with 248 nm laser pulses (60 mJ, 20 ns pulse length). Otherwise the experiments were performed exactly as described in the previous two chapters. With the exception of NAG-d_2, all amino acids and dipeptides listed in this chapter were purchased from Aldrich.

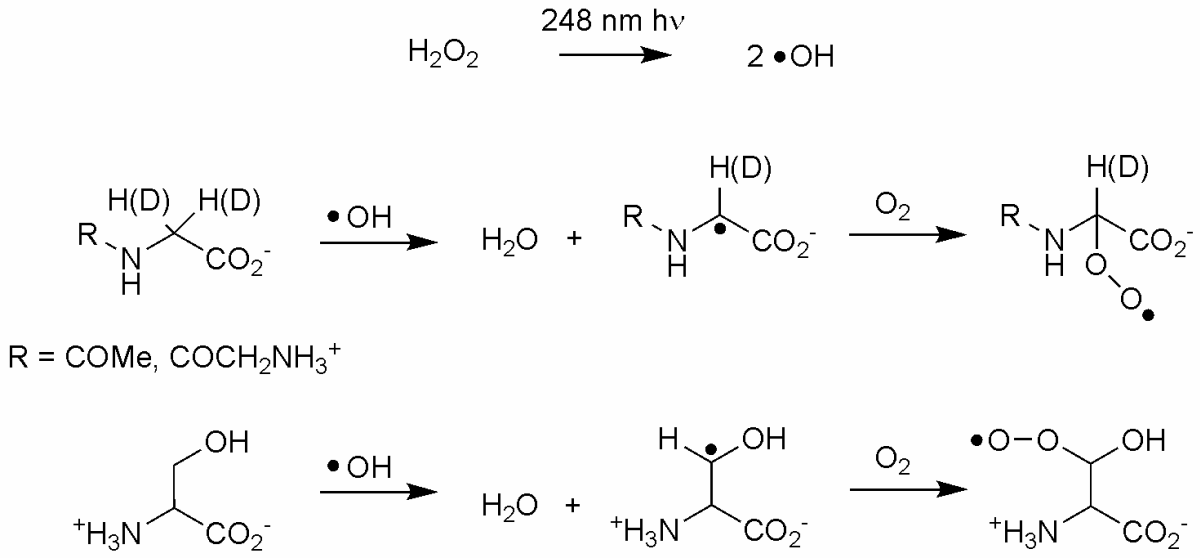

Scheme 4.4: Peroxylation of carbon radicals formed by hydroxyl radical attack.

Synthesis of NAG-d_2. 1.00g of Glycine-C_2-d_2 (13 mmoles) were placed dissolved into 1 mL of H_2O, and added to 5 mL of acetic anhydride (39 mmoles). The reaction was stirred at room temperature for 1 hour. The 1.1 g of NAG-d_2 (71% yield) was collected via filtration. The sample was characterized by ^1H NMR (D_2O): δ 1.84 (s, 3H).

CHAPTER V

PEPTIDE RADICALS AS PROBES FOR THE AQUEOUS MICROENVIRONMENT

5.1 Introduction

The studies discussed in the above chapters focus on the characterization of radical intermediates created from the oxidation of amino acids and peptides in bulk aqueous solution. Although bulk aqueous solution is a relevant medium for biologically relevant studies, this environment is vastly different from that found on within biological cells. One very significant cellular feature is the presence of membranes formed from phospho-lipids and other types of amphiphilic molecules. These molecules associate into bi-layers that create separate the aqueous phase from a non-polar intra-membrane layer. Radicals created within the cell are therefore not free to diffuse to infinite dilution in the cell. They are contained within certain compartments. In an effort to simulate that environment, this chapter will focus on radical pair dynamics within microscopic water-pools formed by a common industrial surfactant. The special CIDEP mechanism that is pertinent here is SCRP which is generated from when a radical pair is contained within a restricted diffusion volume such that they continually re-encounter each other. The most prominent feature of SCRP spectra is the so–called "anti–phase structure" (APS) where each individual hyperfine line of the free radicals is split into two components of opposite phase: emission (E) or absorption (A). Analysis of the APS line shape and its time dependence has been extensively investigated in several laboratories (e.g. the work of Tarasov[75], Shushin[76] and Pedersen[77]). There now exist models for correlated radical pair dynamics that allow for determination of the diffusion coefficients of the radicals in the micro–reactor. Also from such analysis the internal micro-viscosity of the supramolecular structure and the intensity of the Heisenberg electron exchange interaction between the radicals can be estimated.

In this chapter the results of an extensive investigation of the confined radical pair formed by photo–oxidation of diglycine by water soluble quinone acceptors in reverse micelles and microemulsions will be presented and discussed. This work represents the convergence of the two areas of research described in the preceding chapters, photo–oxidation of peptides and diffusion of radical pairs, and is the first application of the micro–reactor model to reverse micelles, which are better mimics of cellular conditions (hydrophobic walls enclosing an aqueous interior) than ordinary aqueous micelles.

5.2 Background

Reverse micelles and water–in–oil microemulsions are microscopic spherical pools of water surrounded by a monolayer of surfactant separating the water pool from a hydrophobic bulk solution (see Scheme 5.1). The surfactant bis(2-ethylhexyl) sulfosuccinate sodium salt (referred to in this field as AOT) is commonly used because of its tendency to form uniform spherical reverse micelles of different sizes controlled by the $[H_2O]/[AOT]$ ratio, W_0. AOT reverse micelles and water-in-oil microemulsions can be used as a spherical "container" to encapsulate a water–soluble radical pair. There have been two previous reports of radical pairs created and contained within AOT reverse micelles. Both of these studies used water–soluble anthraquinone sulfonate salts as the photo-initiated oxidizer, and both organic and inorganic substrates within AOT reverse micelles were used as donors. Turro et al.[78] observed radical pairs in AOT reverse micelles through the one–electron photo–oxidation of sodium sulfite. Akiyama et al.[48] have also used anthraquinone derivatives to photo–oxidize hydroquinone substrates within AOT reverse micelles to form semiquinone radicals. However, radical pair diffusion was not modeled in these studies.

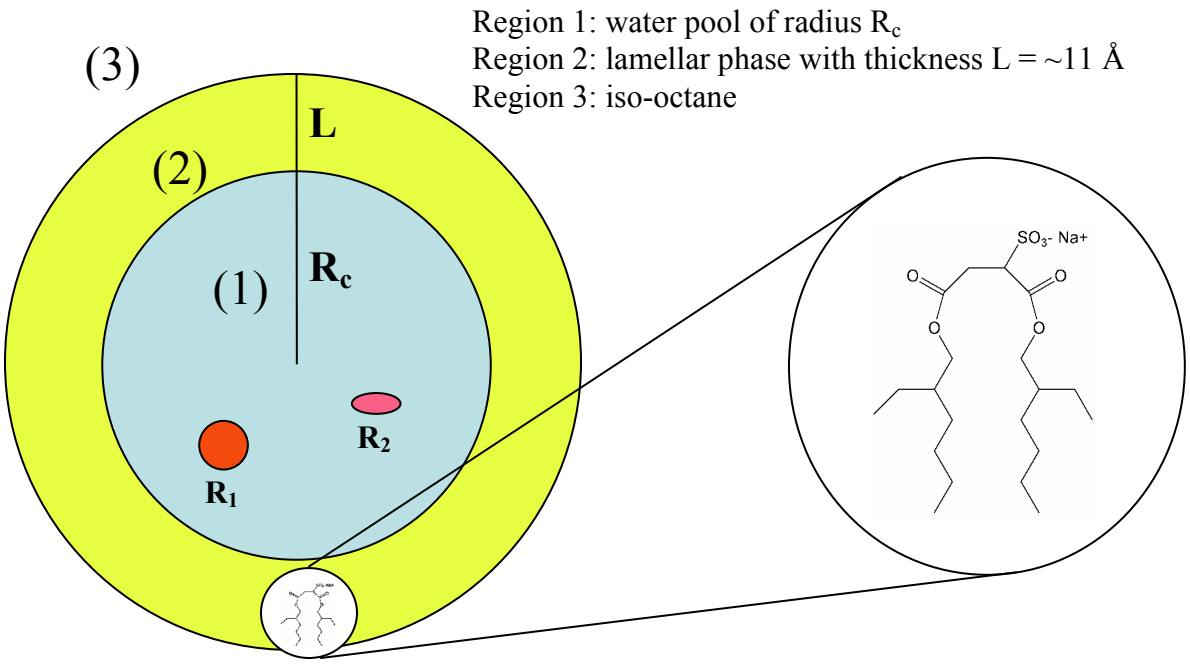

Scheme 5.1: Diagram of an AOT reverse micelle

Our photochemical system is shown in Scheme 5.2 and involves the photo-oxidation of diglycine (GG) which is a water–soluble, biologically relevant substrate.[44] AQS and AQDS are chosen as sensitizers because they are also water soluble. As discussed in Chapters 2 and 3, photoexcitation followed by fast intersystem crossing converts these anthraquinone analogs to their first excited triplet states. At neutral pH, the AQ(D)S triplet state reacts with the carboxylate terminus of the diglycine in a Kolbe–type[61] one–electron oxidation to form the α-amidomethylene radical and the reduced anthraquinone (AQDS). The α–amidomethylene radical, and AQDS, make up the confined radical pair in the interior of the AOT reverse micelle.

When a radical pair is created in a reverse micelle, it remains in the interior although it is still highly mobile. This is advantageous for the observation of sharp EPR transitions. Subsequent diffusion of the radical partners, coupled with the time evolution of the individual electron spin wave functions, gives rise to polarization of the EPR transitions in a predictable way. Simulation of the APS polarization pattern and time dependence has been described in detail in previous work from the Forbes laboratory.[75] The model, which will be discussed in more detail below, can yield information about the relative diffusion coefficient, the interaction of the radicals with the surfactant walls, and the ultimate fate of the reactants (spin relaxation, chemical reaction, or escape processes). It is important to recognize that the APS pattern arises because the radical pair remains within a close enough proximity to allow for electron spin exchange (J), and that the magnitude of this spin exchange interaction is dependent on, and very sensitive to, the rate of encounters between the members of the radical pair.

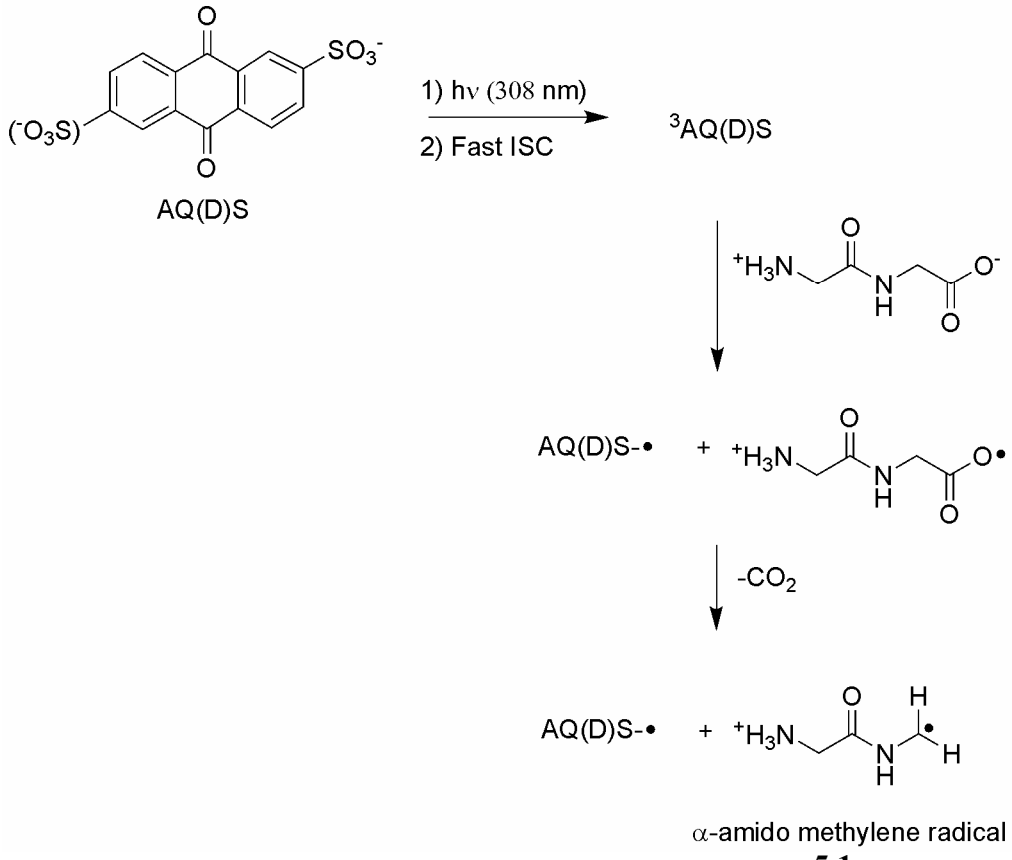

Scheme 5.2: Formation of radical probes

The first explanation of the APS spectral pattern was proposed by Closs, Forbes, and Norris,[13] and also Buckley et al.[79] in 1987. It is now generally referred to as the CFN model after the former paper's authors. It assumes a completely time and space averaged spin exchange interaction, J, which can then be extracted directly from the EPR spectrum by simulation using an average J value as a coupling constant, much like simulating an NMR spectrum. This model essentially ignores diffusion by assuming it is fast compared to the magnitude of J expressed in inverse frequency units. However, there are several experimental conditions for diffusionally restricted radical pairs that lead to TREPR spectra that cannot be simulated using CFN. For example, studies on modified surfactant molecules synthesized in our laboratory have shown that SCRP polarization can evolve on the same time scale as the experiment (0.1–2 μs), and give rise to asymmetric line shapes.[80] In order to simulate such spectra, a new model was proposed by Tarasov[75] which explicitly takes into account radical diffusion and subsequent modulation of the exchange interaction. This is called the micro–reactor model, and we use it here to obtain diffusion, exchange and relaxation parameters of hydrophilic radicals within the water pool of reverse micelles and water-in-oil microemulsions.

5.3 The Microreactor Model and Viscosity

The Closs, Forbes, and Norris (CFN) theory of SCRP, assumes that diffusion (and thus re-encounter rates) of radicals is fast with respect to the frequency of spin-exchange. This means that the observed J values, the distance between the two lines of the APS doublet, is actually a J_{avg} value which is sampled over the entire diffusion volume available to the radical pairs. However, between the dates of the first reported spectra and the present there

have been a number of TREPR spectra of radicals in micelles reported with asymmetric lines shapes, and anomalous spectral shifting. To explain these "anomalous" spectral features, a new theory of spin polarization has been proposed that takes radical diffusion dynamics into account. This model is called the micro-reactor model and was first reported by Tarasov and Forbes in 2000.[75]

In order to fully understand the APS structure of TREPR signals obtained from radicals in confined spaces it is necessary to consider the magnitude of J at different inter-radical distances and times. The spin-exchange interaction has an exponential dependence upon inter-radical distance r and is shown in Equation 5.1.

$$J(r) = J_0 e^{\frac{-(r-R)}{\lambda}} \tag{5.1}$$

Where J_0 = the spin exchange interaction at closest approach, R equals the inter-radical distance at closest approach (assumed to be ~ 6 Å), and λ = the fall off parameter of wave functions in a condensed medium (assumed to be 0.6 Å). The assumption of the CFN model is that the radical pair spends a vast majority of time in the diffusion volume where r > R, and that the radicals effectively sample all states within the time frame of the experiment. The observed J interaction is thus assumed to be an average of all possible J values sampled by the radical pair.

The microreactor model simulates the APS structure through a more rigorous process in which J is calculated at an infinite number of time points and then integrated to generate a simulation of the APS spectra. As the value of J is largest at the point of radical re-encounter, where r = R, J_{obs} is influenced by the rate of forced re-encounters, k_{re} (see Equation 5.2), as well as the value of J_0.[81]

$$k_{re} = \frac{4\pi RD}{V_m} \tag{5.2}$$

Where D is the diffusion coefficient of the radical pair in solution, and V_m is the available diffusion volume within which the radicals may diffuse. When the radical pair is restricted to a small diffusion volume and radical diffusion is fast, k_{re} is large, and J_{obs} increases. In contrast, if D is small, and V_m is large, then J_{obs} decreases. By simulating APS phase, linewidth, and intensities, the microreactor can determine the rate of radical encounters. If the radical pair is contained within a diffusion volume of known size, then the diffusion coefficients of the radical partners can be determined. The D values of the radical pair are directly linked to the viscosity of the solution through the Stokes-Einstein law[82]. (Equation 5.3)

$$D = \frac{k_b T}{6\pi\eta r_{rad}} \tag{5.3}$$

Where T is temperature, k_b is the Boltzmann constant, η is the viscosity of the surrounding solution, and r_{rad} is the molecular radius of the radical. By simulating the intensity, phase, and width of SCRP polarized TREPR transitions attributed to radicals that are diffusionally limited to a known volume, it is possible to determine k_{re}. Once k_{re} is known, the D value of the radical pair, and viscosity of solution can be determined by Equations 5.2 and 5.3 above. Unlike the CFN model, the micro-reactor model does not rely on an estimated J_{avg} value. Rather, the two main input parameters needed to simulate the APS structure using the micro-reactor model are J_0 and D. There are few other methods, such as transient grading,[83] for example, that determine of translational diffusion coefficients directly.

5.4 Results and Discussion

5.4.1 Reverse Micelle Parameters

Isooctane (2,2,4–trimethyl pentane) was chosen as the hydrophobic bulk solution for our experiments. The total radius of a reverse micelle or water-in-oil microemulsion is the sum of the lamellar layer thickness (approx. 11 Å) and the water pool radius, R_c. The value of R_c is dependent on W_0 and can be estimated in a straightforward fashion using Equation 5.4:[84]

$$R_c(\text{Å}) = 36.65\nu/g \tag{5.4}$$

The variables, ν and g, are the weight percentages of water and AOT, respectively.

To minimize the possibility of multiple radical pairs being formed in one RM, these experiments were carried out with a majority of the reverse micelles containing only one radical pair. The Poisson distribution[85] was used to determine the concentration of AQ(D)S needed to achieve this condition. In general the experiments were run with an AQDS/RM ratio of 0.3. For this ratio, 74 % contained no photosensitizers, 22 % contained one photosensitizer, 3 % contained two photosensitizers, and < 1 % contained three or more. Each reverse micelle also contained anywhere from 20–40 GG molecules. This high GG concentration was needed to increase the probability of electron transfer for better sensitivity. This may have an effect on the microemulsion structure, which makes the accuracy of Equation 5.4 somewhat questionable for this system. It is not immediately clear that any fluctuation in the observed spectra caused by the high concentration of GG will be systematic with regard to water pool size. This will be discussed in more detail below.

Diffusion of the radical pair is limited to the water volume contained within surfactant walls by the polar head groups of the AOT molecules. This leads to a high

probability of radical reencounters in which the spin of the unpaired electron on each member of the radical pair experiences an electron exchange interaction with the other radical. By changing the size of the water-pool by varying W_0, the maximum volume into which the radical pair can diffuse changes thereby changing k_{re}.

5.4.2 Time Dependence

The two radicals shown in Scheme 5.2 have been fully characterized in free solution in this work, using field swept TREPR. They have also been studied by Tarabek et al. using a FT-EPR technique.[44] Figure 5.1A shows the X–band TREPR spectrum of radicals **5.1** and $AQDS^{-}\bullet$ in bulk water at pH 5.5. The α–amidomethylene radical is represented by 3 packets of 1:1:3:2:3:1:1 spectral lines while the $AQ(D)S^{-}\bullet$ radical is represented by relatively intense and closely spaced lines, which are completely emissive. The signal from the central radical $AQDS^{-}\bullet$ is cut off at the bottom of each scan to allow the transition for radical **5.1** to be seen more clearly. Spectra of the same radicals in AOT reverse micelles are shown in Figures 5.1B-E.

In free aqueous solution the spectra exhibit CIDEP spectral patterns from two different mechanisms. The RPM[15] polarization can be accounted for by comparing the low and high field packets of lines attributed to radical **5.1**. The low field lines show stronger emission than those of the high field packet. TM [11] appears as net emission, which is the expected phase of the TM for quinone triplet states.[86,87] The TM and RPM polarizations add to give the resulting overall pattern of E*/A. The hyperfine and g–values obtained by simulation of this free solution spectrum are consistent with previous data obtained by the FT–EPR measurements of Tarabek, et al.[44] The free solution spectrum is included at the top

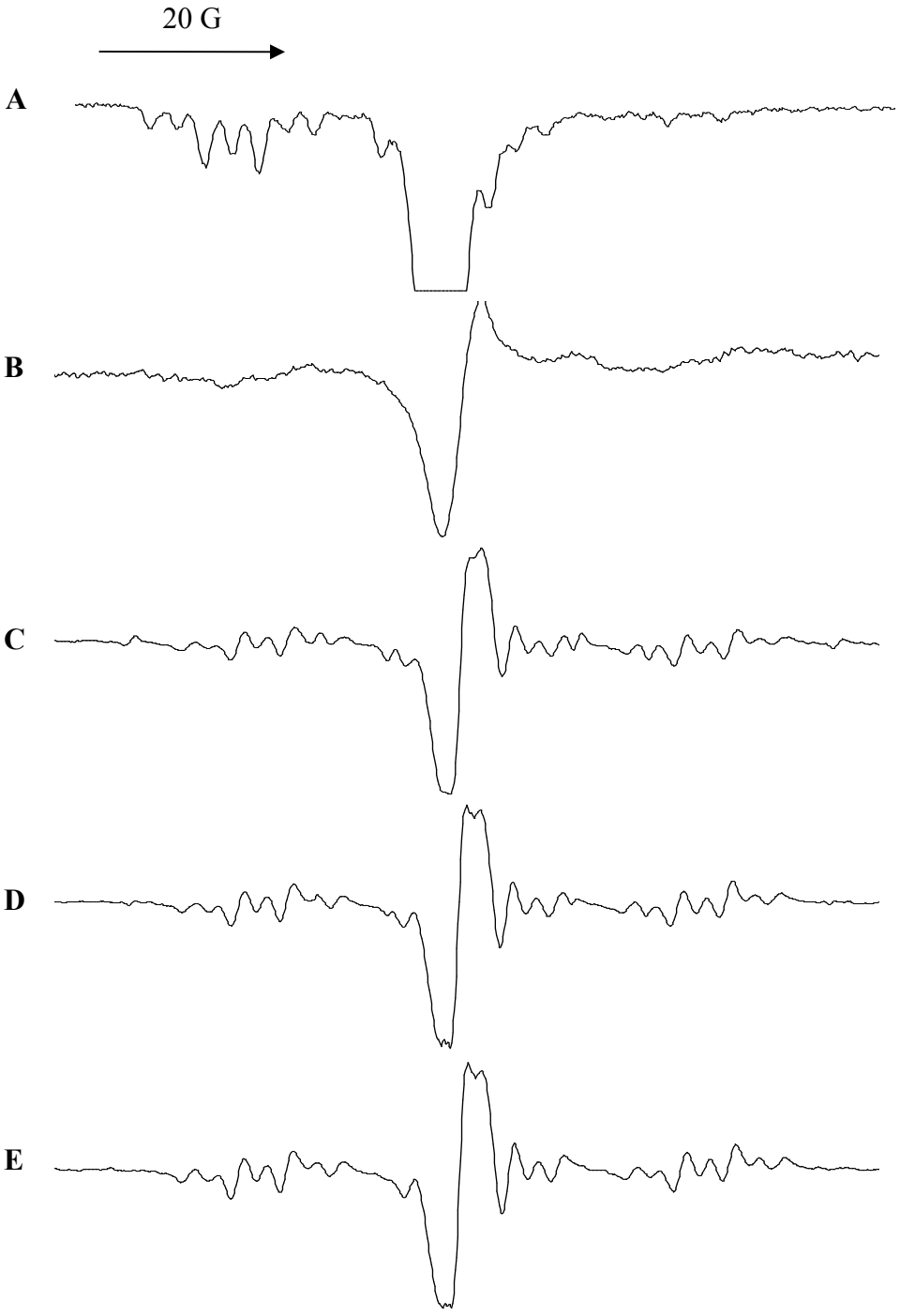

Figure 5.1: A) TREPR spectra taken acquired at a 400 ns delay time of radicals 5.1 and AQDS-• in bulk aqueous solution of pH 5.5 (2.5 mM AQS, 200 mM GG). B-E) TREPR spectra of radicals 5.1 and AQDS inside AOT reverse micelles with R_c = 23 Å at B) 100 ns, C) 200 ns, d) 1000 ns, E) 2000 ns.

of Figure 5.1 for comparison to that in reverse micelles where a different polarization pattern appears, and also to clearly show that the same radicals are formed in both cases. It can be concluded from Figure **5.1** that the photophysics and photochemistry are the same for reverse micelles as in free solution, with one minor exception that will be discussed below.

Figures 5.1B-E show the radical pair created in AOT reverse micelles at increasing delay times after the laser pulse. The SCRP polarization pattern is observed when the radical pair is formed inside the water pools of reverse micelles and water-in-oil microemulsions, indicated by the E/A character of the central peak attributed to radical $AQDS^{-}\bullet$. Figure 5.1B shows APS features (E/A splitting of each line) in the spectrum at a delay time of 100 ns, although they are broad and asymmetric. This indicates that once formed, the radical pair diffuses freely and quickly throughout the hydrodynamic volume of the water pool. At 200 ns (Figure 5.1C) the polarization mechanisms have evolved enough so that APS can be seen in individual transitions. At longer delay times (Figures 5.1D and 5.1E) the APS is still present, indicating that the correlated radical pair has not escaped from the microemulsion. Longer delay time measurements (up to 20 μs) indicate that radical escape is negligible for this system over at least this range of delay times. This is to be expected for charged species which are unlikely to cross over into the hydrophobic environment of bulk isooctane. Back electron transfer is of course prohibited by the irreversibility of the reaction, i.e., when there is fast decarboxylation.

The micro–reactor model predicts that the size of the water pool and the re-encounter rate constant k_{re} will dictate the line shape and intensity of the APS spectral pattern. As radicals **5.1** and $AQDS^{-}\bullet$ are formed inside the water pool by the reaction depicted by Scheme 5.2, the micro–reactor model predicts that the radical pair will evenly distribute

throughout the hydrodynamic volume within the first 10 ns. This is called the "filling out" of the micro–reactor. Once the radical pair has sampled all available inter–radical distances, the resonance line shape is governed by the steady rate of an internal spin relaxation process induced by the exchange interaction. Normally this rate is comparable with the inverse time for filling out of the water pool. Therefore, the essential changes in the APS shape normally take place within the time resolution of EPR spectrometer, and little change is observed in the spectra at subsequent delay times.

The time dependence of these spectra can be summarized as follows: Figure 5.1 clearly shows that the TREPR resonance lines are polarized. There are three mechanisms which contribute into the polarization. The TM (negative net polarization), which is due to the electron transfer reaction taking place from polarized electron spin sublevels of the molecular AQS (and AQDS) excited triplet states. The second is the RPM mechanism which gives E/A multiplet polarization and manifests itself as a positive polarization of high-field lines of radical **5.1** and also gives a specific line shape for the signal from radical **AQDS^{-}•** (like first derivative signal). The third mechanism is the SCRP polarization which gives the APS shape. It is important to note that the contribution from the RPM is more pronounced at earlier delay times. At longer delay times, the signal is fully defined by the APS in both radicals. This interesting characteristic of the TREPR signal evolution from spin-correlated radical pairs, which is due to internal longitudinal spin relaxation, has been discussed thoroughly and modeled successfully in previous work. Because this has been observed and simulated previously for "normal" aqueous micelles (e.g. SDS), this result demonstrates that this phenomenon is a general one for confined mobile radical pairs.

5.4.3 AQS vs. AQDS

The two different anthraquinone analogs exhibit somewhat different chemical reactivity in the reverse micelle environment. The AQS molecule, with a sulfonate group on only one end, exhibits slightly amphiphilic character, while the AQDS is negatively charged at both ends. Figure 5.2 shows TREPR transitions consistent with the structures of radicals **5.1** and anthraquinone radicals from both sensitizers. In Figure 5.2A, where the sensitizer is AQS, there are several additional APS lines marked with asterisks. These transitions are attributed to radical products formed by H–atom abstraction from the hydrophobic alkyl chains of the surfactant AOT by ^{3}AQS*. The transitions are difficult to accurately simulate due to a number of possible primary, secondary, and tertiary radical products as shown in Scheme 5.3. The more thermodynamically stable tertiary product (A) would be in kinetic competition with the 5 types of secondary radicals (B). The primary radicals (C) are not likely to be observed in this experiment as they are rarely produced when significantly more stable radicals can form. Hydrogen atom abstraction from isooctane is not the source of these observed radicals, because when heptane is used as the bulk liquid, the same spectral pattern is observed. In Chapter 6, these surfactant-based radicals will be characterized in more detail.

The observation of radicals from both H–atom abstraction chemistry and the photo–oxidation reaction allows us to conclude that AQS resides in both the aqueous core and the lamellar phase of the surfactant. Within the aqueous core, the oxidation of GG as outlined in Scheme 5.2 is dominant; and in the lamellar phase H–abstraction is the primary process. This follows directly from consideration of the local polarity in each region. In the AQDS case, only radicals **5.1** and AQDS$^-$• are observed. Because there are two sulfonate groups on

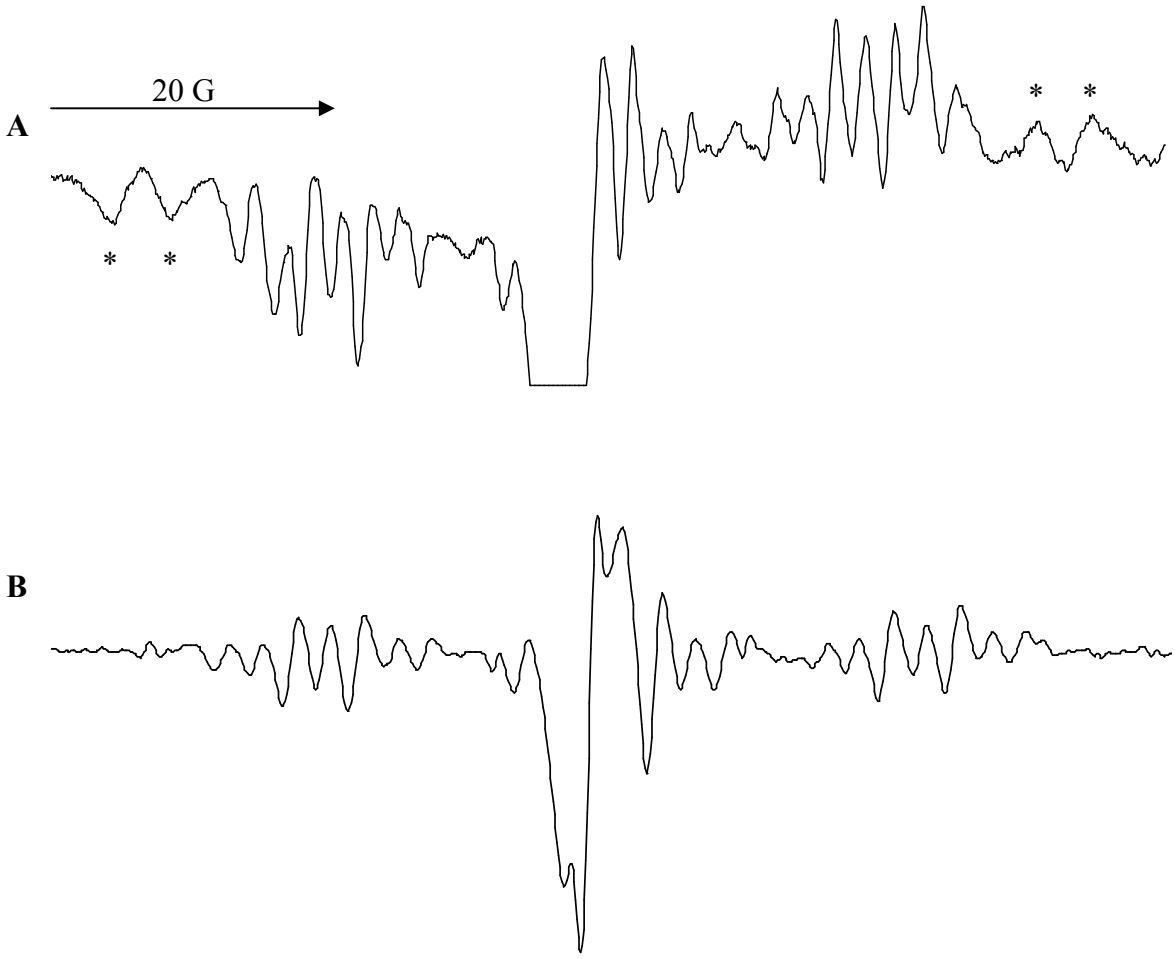

Figure 5.2: TREPR spectra of radicals 5.1 and A) AQS-• in a 37 Å AOT RM and B) AQDS-• in a 33 Å AOT RM. Both spectra were acquired at a 400 ns delay time at 25 °C. Asterisks in A) denote radicals formed from H-abstraction reactions from the AOT surfactant.

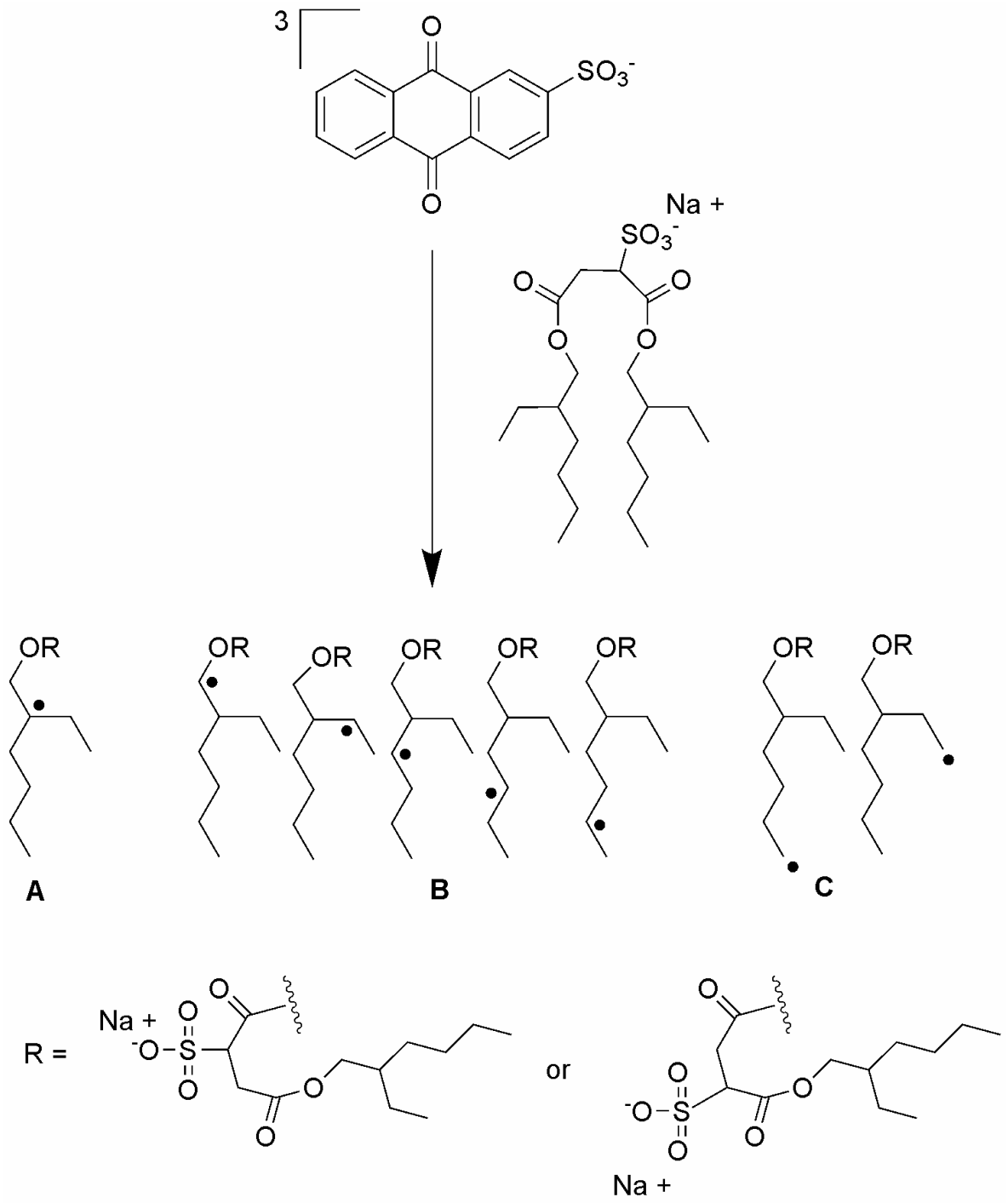

Scheme 5.3: Possible AOT A) tertiary, B) secondary, and C) primary radicals produced upon oxidation by ^{3}AQS*.

the AQDS, it is much more likely to remain in the aqueous core and not diffuse into the lamellar surfactant phase. Figure 5.2B confirms this, where AQDS is used as the sensitizer and the size, temperature and delay time are all the same as for Figure 5.2A. No alkyl radicals are detected in this spectrum, and for clarity the remainder of this work will report spectra involving only AQDS as the sensitizer.

5.4.4 Size Dependence

The APS spectral shape is primarily affected by two parameters: the radical reencounter rate (k_{re}), and the rate at which the confined radical pair samples all possible inter-radical distances, described by the diffusion coefficient (D). As the hydrodynamic volume decreases, so does the maximum distance between the radical pair. This means that radical pair spends more time in close range, thereby increasing the probability of reencounters, k_{re}. The ratio of k_{re}'s for reverse micelles or water-in-oil microemulsions for any two R_c values, will change according to Equation 5.5:

$$k_{re1}/k_{re2} = c\ ((R_1^3)^{-1}/(R_2^3)^{-1}) = c((R_2^3/R_1^3)) \quad (5.5)$$

If our assumption that the diffusion of the radical pair takes place throughout the entire micelle volume is correct, the rate of the re-encounter process must be proportional to the diffusion coefficient of the radicals and inversely proportional to the inverse volume of the micellar phase (Equation 5.6).

$$k_{re} = c\ D/R^3 \quad (5.6)$$

It is important to note that the k_{re} (which decreases as RM's increase in size due to increased volume) and the decrease in viscosity (increase in k_{re} as RM's get bigger) are competing with each other to change the APS line shape in different ways, and can be probed by systematically changing the size of the aqueous core. Figure 5.3 shows spin–correlated spectra of radicals **5.1** and $AQDS^{-}\bullet$ in water-in-oil microemulsions and reverse micelles of different R_c. Unlike Figure 5.2A, no signals from H–atom abstraction reactions are observed, therefore we can conclude that radicals **5.1** and $AQDS^{-}\bullet$ are formed only from electron transfer reactions inside the aqueous core. Figures 5.3A and 5.3B show some APS features in the transitions due to radical **5.1** and in the central peak resulting from radical $AQDS^{-}\bullet$. The E/A RPM pattern is still apparent in radical **5.1**. Figures 5.3C and 5.3D clearly show an increase in APS intensity for both radicals. The intensity of the APS can be estimated by observing the high field side of the emissive peak corresponding to radical $AQDS^{-}\bullet$. As the water pool decreases in size, the central peak changes from pure emission to pure E/A polarization.

Figures 5.3E–F show that as the R_c value is decreased below 20 Å the individual transitions begin to broaden and become quite asymmetric. This is expected to occur as spin exchange increases to a rate much faster than that of D. This illustrates that average inter–radical distance has much larger effect on k_{re} than an increase in viscosity in the reverse micelle interior. These last three spectra should be viewed with some caution as the water pool is so small for these reverse micelles and the concentration of GG so high that substantial structural deviations from normal spherical water pools may be taking place.

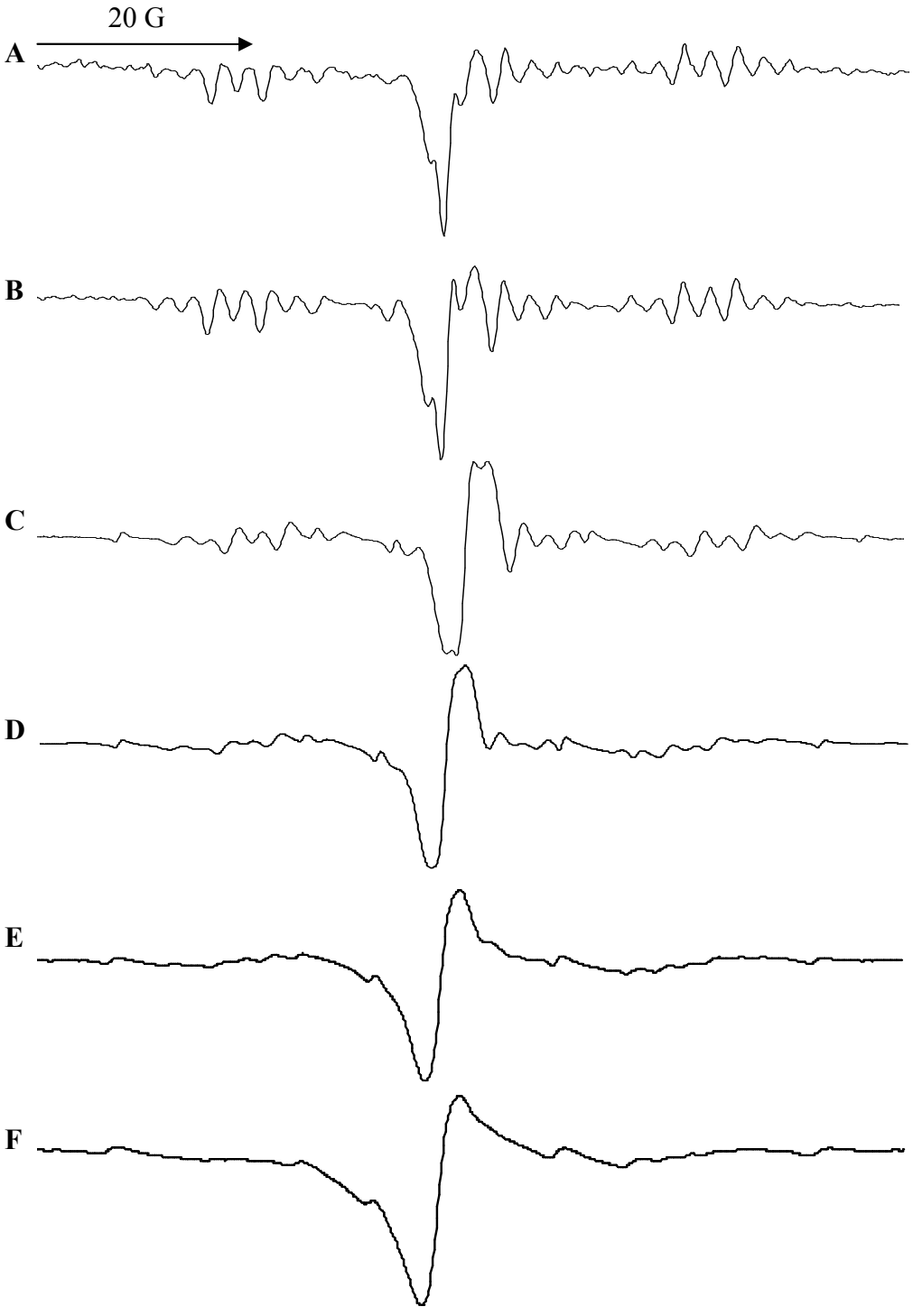

Figure 5.3: TREPR spectra of radicals **5.1** and AQDS-• in AOT RM's with R_c = A) 53 Å, B) 43 Å, C) 23 Å, D) 17 Å E) 6 Å. All spectra were acquired at a 400 ns delay time at 25 °C.

5.4.5 Temperature Dependence

An increase in temperature should increase both D and k_{re}. By simulating the APS line shape at different temperatures, it is possible to estimate the effect of D on the system without changing the volume of the hydrodynamic core. Figure 5.4 shows the temperature dependence of the TREPR spectra of AQDS/GG in a 33 Å AOT water–in–oil microemulsion. The change in the APS structure in the center signal of radical $AQDS^{-}\bullet$ is not as apparent as in the size dependence shown earlier in Figure 5.3. At 30 ˚C, the APS appears slightly more intense than at 45 ˚C. The micro–reactor model predicts that stronger APS intensity should be observed at higher temperatures. One possible reason for this effect being so minor this system is that there could be a substantial increase in the hydrodynamic radius at higher temperatures. Eicke et al.[88] studied the hydrodynamic radius of sodium AOT microemulsions at various temperatures, and found little change in size. In the absence of and increase in reverse micelle size, we suggest that the water pool radius can increase, by thermally freeing up the layer of "bound" water molecules at the sulfonate–water interface, thereby allowing the radical pair access to an increased diffusion volume.

5.4.6 Simulation of TREPR Spectra and Extraction of D Values

The micro–reactor model is constructed by assuming that one radical is in a fixed position in the geometrical center of the water pool. The furthest accessible distance between the two radicals is known and limited by the radius of the aqueous core, R_c. The radius of closest approach, where the inter-radical distance equals r_0, (~ 6 Å) is also taken into account to set the radial diffusion limits. At this radius, $J = J_0$, and can be calculated. The D value and transverse relaxation time T_2 are varied to best fit the simulations to the data, and the

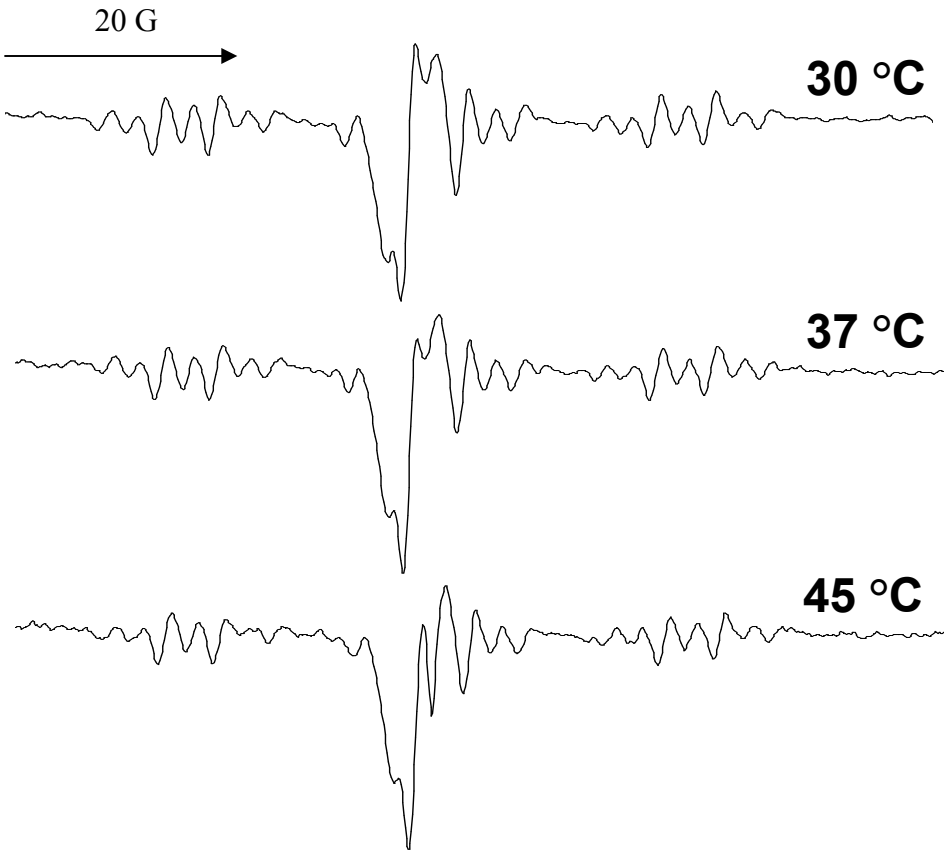

Figure 5.4: TREPR spectra of radicals **5.1** and AQDS-• in AOT RM's (R_c = 33 Å) at a delay time of 400 ns at the temperatures indicated.

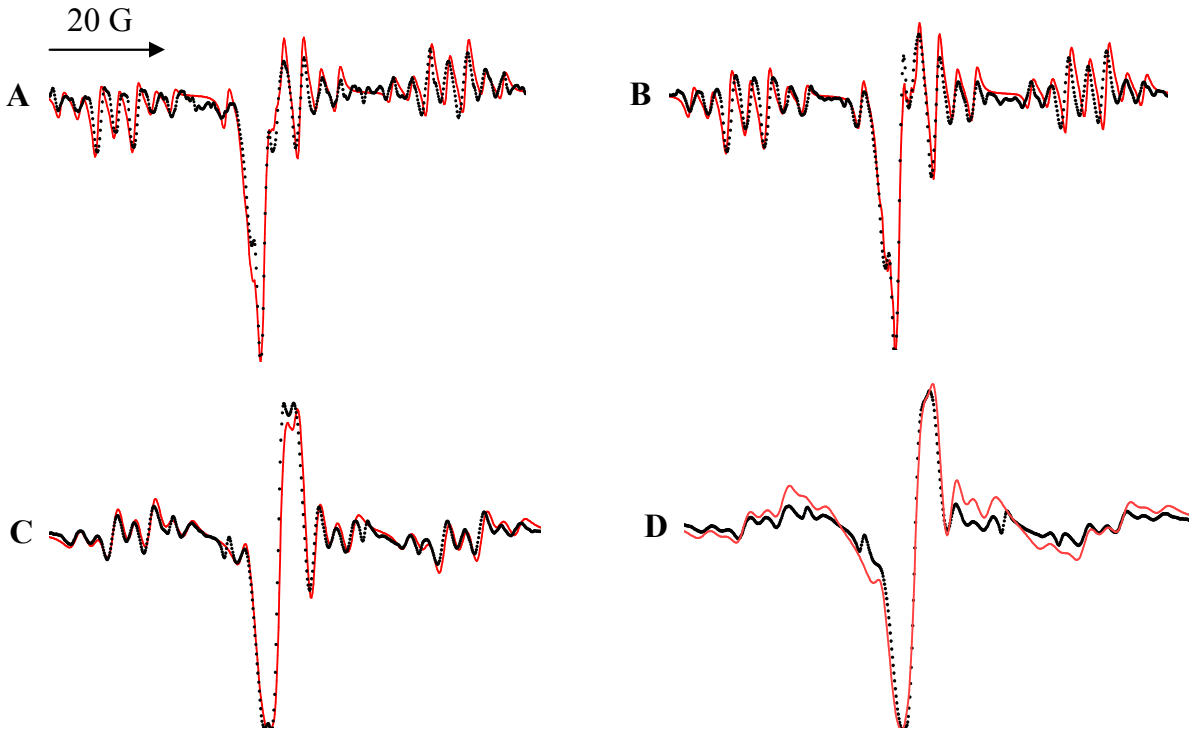

Figure 5.5: TREPR spectra and simulations of radicals **5.1** and AQDS-• created inside AOT RM's using the micro-reactor model for R_c values A) 53 Å, B) 33 Å, C) 23 Å, and D) 17 Å.

results are shown in Figure 5.5 for four different water pool sizes. The parameters used are listed in Table 5.1. The J_0 values should not change with water pool size and were held constant in all simulations. As expected, D decreases with water pool size as the viscosity increases. Above $W_0 = 15$ or $R_c = 20$ Å, the water molecules are considered unbound and free to diffuse as in bulk solution.[85] Below this value, the water interacts strongly with Na^+ ions lining the wall created by the sulfonate head groups. The D value for the radical pair with a 17 Å water pool is nearly two orders of magnitude smaller than that in a water pool of radius 53 Å. Graph 5.1 shows that there is a roughly linear increase in D with increasing R_c values. Also shown is the estimated diffusion coefficient for these species in bulk water (~ 3 x 10^{-6} cm^2/s) calculated using the Stokes-Einstein relation. As the size of the water-pool increases, the calculated D values approach this bulk value. Unfortunately, the fast T_2 broadening of the TREPR signal for the radical pair in smaller size reverse micelles makes data simulation much more difficult and time–consuming. The faster T_2 relaxation for this spectrum is attributed to dipolar relaxation of the radical pair.

Ignoring the electron–electron dipolar interaction in the SCRP is a clear disadvantage of the theoretical model. Unfortunately, this cannot be overcome by including the interaction directly in the model. On the other hand successful simulation demands a decrease in the T_2 relaxation times. It is clear that the dipolar interaction is responsible for some internal relaxation (as is the exchange interaction), and can be roughly taken into account as an external relaxation process. A decrease in the average distance between the radicals within the water pool radius must increase the rate of dipolar relaxation. In large micelles, this interaction can probably be neglected. However, in small micelles, it cannot. Therefore, to get better simulations we were forced to increase the rate of transversal external relaxation,

W_0 ([H_20]/[AOT])	Water Core Radius (Å)	J_0 (MHz)	D (x10^{-6} cm^2/s)	T_2 Relaxation Time (x 10^{-6} s)
37	53	-31	2.40	0.36
30	43	-31	1.60	0.36
23	33	-31	1.20	0.24
16	23	-31	0.40	0.24
12	17	-31	0.05	0.12

Table 5.1

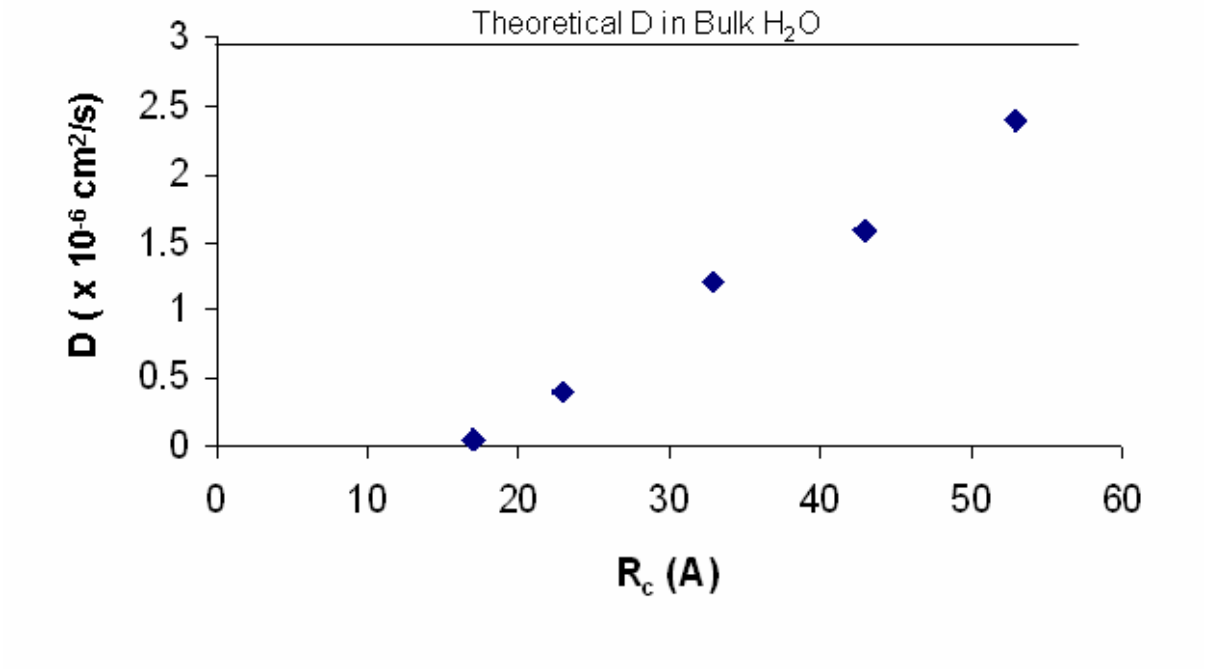

Graph 5.1: Plot of diffusion coefficients (extracted from simulations) with versus water pool radius. The theoretical D value in bulk solution was calculated using the viscosity of water (1 cP) at 296 K, and an average radius of the combined volumes of the two radical probes (7.5 Å).

which at present is an artificial solution to a real problem. This issue is currently being addressed at present in our laboratory. The structure of the small water pools with large GG concentrations will also be investigated using neutron scattering techniques, which have previously been used to characterize unusual micellar structures.

5.5 Conclusions

The interior of AOT reverse micelles and water-in-oil microemulsions have been probed using a charged radical pair formed by the photo-oxidation of glycyl–glycine by water soluble anthraquinone derivatives. Our TREPR spectra provide information on the reactivity of these radical species in both the interior and lamellar phases of the microenvironment. The micro–reactor model has been applied to assign quantitative D values to the radical pair, and it is found to change monotonically with water pool size but seems to be relatively independent of temperature. This is a new approach to investigating the microviscosity of such environments.

5.6 Experimental

All continuous wave TREPR experiments were performed as previously described in Chapter 2. All spectra were recorded on a Varian E–line EPR console and bridge modified with a fast preamplifier and a low noise GaAs FET microwave amplifier (25 dB gain). The microwave power incident on the samples was 10 mW for all experiments. The solutions containing the reverse micelles were circulated through a quartz flow cell of path length 1.0 mm centered in a rectangular brass TE_{103} cavity. The solutions were irradiated by a 308 nm laser pulse (20ns width, ~40 mJ, repetition rate: 60 Hz) from an excimer laser LPX100i

(Lambda Physik). Spectra were collected at a fixed delay time after the laser flash using a Stanford Research Systems boxcar integrator (100 ns gates), and the external field was swept over 2 to 4 minutes. All spectra and simulations shown have a sweep width of 80 G except as noted.

Glycyl–glycine (Aldrich), AQDS (Aldrich), and isooctane were of purest commercially available grade and used as received. The water used in the reverse micelle and water-in-oil microemulsion cores was purified on a Millipore purification system. The dioctyl sulfosuccinate sodium salt (Aldrich) was purified by dissolving 140g in 700mL of dry methanol. The solution was chilled to 5 ^{o}C and centrifuged to separate out the insoluble white solid. The resulting solution was evaporated under reduced pressure at 50^{o} C. The resultant solid was dried over P_2O_5 in a vacuum oven at 50 ^{o}C for 1 day. The resulting white solid was spongy and opaque.

CHAPTER VI

TREPR AND CIDNP STUDIES OF THE OXIDATION OF AOT

6.1 Introduction

This chapter will focus on electron transfer chemistry that occurs between AQDS and AOT itself. Due to its unique phase behavior in the presence of water, bis(ethylhexyl) sulfosuccinate ester (Aerosol–OT or AOT, left side of Chart 6.1) is a widely used surfactant for the formation of water–in–oil microemulsions. These microemulsions have many important industrial applications, including the synthesis of AgBr particles for the photographic industry[89,90] and CdS particles for semiconductor sensor applications.[91] Such nanoparticles are photochemically redox active, therefore it is somewhat surprising that the photo–redox chemistry of the AOT surfactant has not previously been investigated in greater detail. Water soluble quinones have photo–excited triplet states that are strong oxidants and are easily created in the interior of AOT microemulsions and we have used this chemistry previously to study oxidation of biologically relevant substrates in AOT RM's. Here we use one of the same quinones, 2,6–anthraquinone disulfonate sodium salt (AQDS, right side of Chart 6.1), to investigate the photo–redox behavior of the AOT surfactant itself. Of particular interest is whether photo–oxidation occurs via electron transfer reactions or by hydrogen atom abstraction from AOT at the water–surfactant interface.

TREPR spectroscopy is ideal for such investigations as it allows for observation of, in most cases, free radicals produced from the primary photophysical and photochemical events after a laser flash. CIDEP is often observed in such experiments and this phenomenon can be used to extract mechanistic and dynamic information about the radical pairs. A related experiment that detects chemically induced nuclear spin polarization (CIDNP) in the products can be used to corroborate mechanistic hypotheses and support structural assignments of free radical intermediates. As will be detailed below, we have discovered a

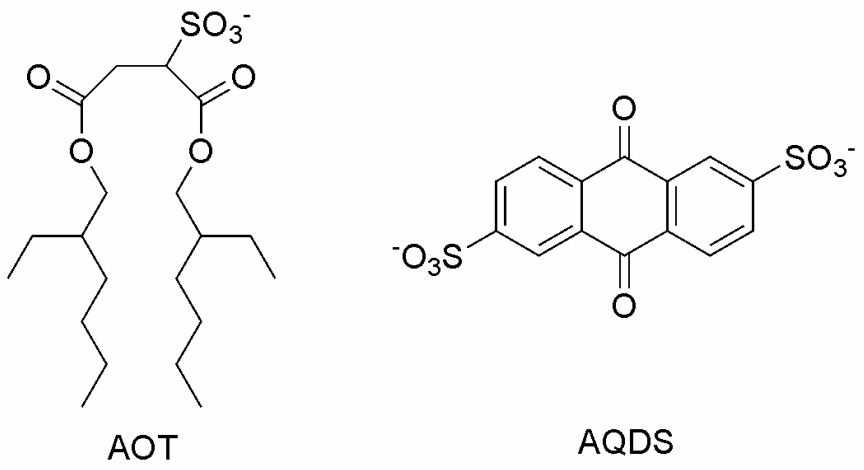

Chart 6.1: Structures of AOT and AQDS

remarkable range of photo–reactivity for AOT, involving several competing pathways that TREPR and its associated CIDEP and CIDNP mechanisms can help to unravel. The two complementary techniques (TREPR and CIDNP) are powerful tools for the investigation of mechanistic organic photochemistry.

For a number of reasons, AQDS is a good choice as a photo–oxidant in AOT microemulsions. It is a charged species and should therefore be located primarily within the water pool of the RM. Its highly reactive triplet state is formed quickly and can participate in electron transfer, H–atom transfer, and oxidative rearrangement reactions.[92] In hydrophobic environments, neutral anthraquinones react mainly through hydrogen transfer and triplet energy transfer pathways.[93] The photochemistry of anthraquinone derivatives and their ensuing radical reactions in both aqueous and non–aqueous media are well understood, but they remain of significant interest to us in RM systems because of their proximity to both hydrophilic and hydrophobic regions of the supramolecular assembly.

In earlier investigations of photo–redox chemistry within RMs, Turro and Khudyakov placed AQDS within AOT RMs of various sizes and observed, using TREPR, that radical pairs are formed from electron transfer after excitation of Na_2SO_3.[78] Their detailed investigation of sulfite oxidation in AOT RMs is important to our investigation and will be elaborated on below. In another study, Akiyama and Tero–Kubota examined the oxidation of hydroquinone species located in the interior of AOT RM's.[48] In our laboratory, we have used TREPR to observe radicals formed by oxidation of glycyl–glycine by ^{3}AQDS* in the interior of AOT RM's.[94] The reactivity of AQDS with the AOT surfactant itself is mentioned in the previous chapter but not addressed specifically.

The AOT molecule contains a hydrophilic anionic sulfonate head group, while the tail consists of an ester group and a branched hydrocarbon. The most probable photo–oxidative pathways that can occur with these functional groups are depicted in Scheme 6.1. Reaction **A** shows oxo–acyl radicals formed from direct Norrish I α–cleavage of the ester group. Although esters are commonly thought to be photochemically robust, steady–state EPR spectra of radicals have been observed during ester photolysis, and this cleavage reaction has been observed in time–resolved studies in our laboratory when acrylic polymers are irradiated with UV light.[95] However, absorbance of this chromophore at 308 nm is very weak, and as will be detailed below, control experiments with only AOT microemulsions show that direct photolysis of the ester functionality in our experiments is unlikely.

Pathway **B** shows radical cations located on the carbonyl oxygen, and these are also known to be formed from photo–excited esters.[96] Tertiary and secondary alkyl radicals formed on the alkyl tail of the AOT molecule (pathway **C**), have been observed by White et al.[94] but their mechanistic origins were not discussed in that work. The α– and β– sulfonate radicals (pathway **D**), have been reported to occur via H–atom abstraction of vinyl sulfonate by the hydroxyl radical.[97] The sulfonate group itself might also act as an electron donor, as shown in pathway **E**. We propose this possibility because it is known that, for example, sodium sulfite can be oxidized to form sulfite anion radicals.[78,98]

The TREPR experiment can give characteristic structural information about radicals through the g–factor and hyperfine coupling constants. When a radical pair is formed in a confined environment, diffusion is limited, and re–encounters occur between the radical partners. This manifests itself in TREPR spectra through CIDEP effects, particularly line-shapes and intensities. In some cases, fine structure due to spin exchange or dipolar

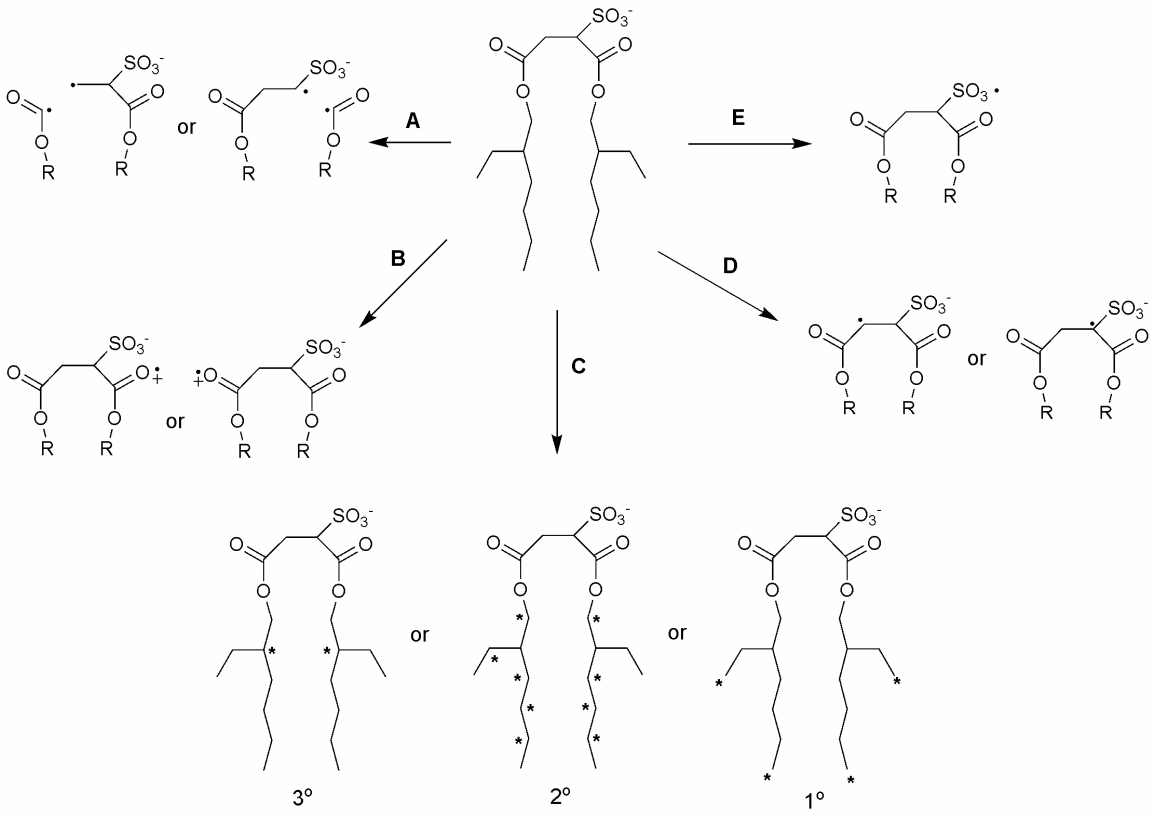

Scheme 6.1: Possible photo–oxidation pathways of AOT. The radical products from pathway C are denoted by asterisks. R= $–CH_2CH(CH_2CH_3)(CH_2)_3CH_3$.

interactions appears as additional splittings of hyperfine lines. The CIDEP polarization pattern can change depending on the identity of the radical pair involved, as well as the environment in which the radical pair is formed. For example, the solvent viscosity, spin state of the radical precursors (singlet, triplet, etc.), and limits to diffusion (solvent boundaries such as the lamellar phase of a surfactant, all affect the appearance of TREPR spectral transitions. We have used these patterns previously to extract information about radical mobility and water pool viscosity inside of an RM. The theoretical and quantitative details of these changes have been reported in two previous publications.[75,94,99]

Two CIDEP mechanisms are particularly relevant to the TREPR spectra shown here. They are the Triplet Mechanism (TM) and Spin Correlated Radical Pair (SCRP) mechanism. The 3AQDS* creates strong emissive polarization due to TM. This has been described in preceding chapters and will not be elaborated upon further here. Exchange interactions and dipolar couplings are both distance dependent and diffusion in these systems can be fast, therefore when SCRP polarization is also present, simulation of the TREPR line shape is not trivial. There are several models for predicting the appearance of SCRP spectra using approximations for the diffusion problem[79,13] which have been successfully applied to radical pairs observed in micelles[80] and RM's.[48,78,94] A more rigorous treatment that takes both diffusion and re–encounter rates of the radical pair into account was used in our earlier analysis of diffusing radical pairs formed by ^{3}AQDS* oxidation of glycyl–glycine in the interior of AOT RM's.[75]

Once created, a radical pair has two fates: recombination to form geminate products or they can diffuse apart and combine with other radical species (escape products). If the radicals are created initially from a triplet state, recombination is at first forbidden and they

must diffuse away from each other to allow spin wave function evolution to the singlet state and are more likely to form escape products. A consequence of this process is that protons in both the geminate recombination and escape products have an excess of spin population in the higher or lower Zeeman levels. This leads to emissive or enhanced absorptive peaks in the NMR spectra of the products, respectively, which can be detected in a CIDNP experiment. To form a more complete picture of mechanistic photochemistry involving free radicals, it is often informative to detect both CIDEP and CIDNP polarizations.

The goals of the studies presented in this chapter are 1) to present a complete structural characterization of all free radicals created from the photochemistry of AQDS in the presence of AOT, 2) to delineate the various photo–oxidation mechanisms for the AOT/water/AQDS system, and 3) to correlate the observed CIDEP mechanisms with the location and mobility of the radical pairs of interest. We use standard CIDEP simulation routines involving the TM, the RPM and the more approximate model mentioned above (see refs 15 and 16) for SCRP polarization. Even with this simpler model, we can simulate the APS structure reasonably well, and this allows us to estimate the location of the radical pairs within the RM. We will report some approximate values for the exchange couplings in these systems, however we stress that they are used only to obtain reasonable fits of the line positions and intensities. In further studies we will use the more accurate micro-reactor model (described in the preceding chapter) to investigate aspects of radical pair diffusion in the present photochemical system.

6.2 Results and Discussion

6.2.1 TREPR experiments at Room Temperature

After irradiation with UV (308 nm or 355 nm) laser light, AQDS undergoes intersystem crossing from the first excited singlet state to its lowest triplet excited state, ^{3}AQDS*, which is a strong oxidant. This triplet state has been used in our laboratory and in others to oxidize a variety of organic groups in aqueous media including amines,[44] carboxylates,[44,94,100] sulfides,[37,101] hydroquinones,[48] and the inorganic anion SO_3^{2-}.[78] Figure 6.1 shows the experimental TREPR spectrum obtained after 308 nm excitation at room temperature of AQDS in an AOT reverse micelle. To show all of the transitions, the spectrum has been scaled up to cut off the most intense lines in the center. This remarkable spectrum shows more that 30 different lines, many of which have different line widths and show different CIDEP patterns. It is clear by inspection that there are several different signal carriers. It should be noted that this spectrum was acquired at a fairly fast scan rate and so the line shapes of some of the signals are slightly distorted. Figure 6.2 shows an expanded, narrower sweep width spectrum of the same system acquired at a slower scan rate to show that the predominant CIDEP mechanism for most transitions in the spectrum is SCRP, i.e., there are E/A doublets for each hyperfine line. However, the line widths for some of transitions are sharp and for others they are much broader. Furthermore, the broader E/A doublets are much less intense. These features allow us to differentiate between some of the TREPR signals in Figure 6.1 and are the starting point for a deconvolution of the complex spectrum in Figure 6.1 into individual radical sub–spectra.

Figure 6.3 shows a spectrum from this system that has been expanded further to show only the central transitions. The perimeter transitions are SCRP polarized as E/A doublets,

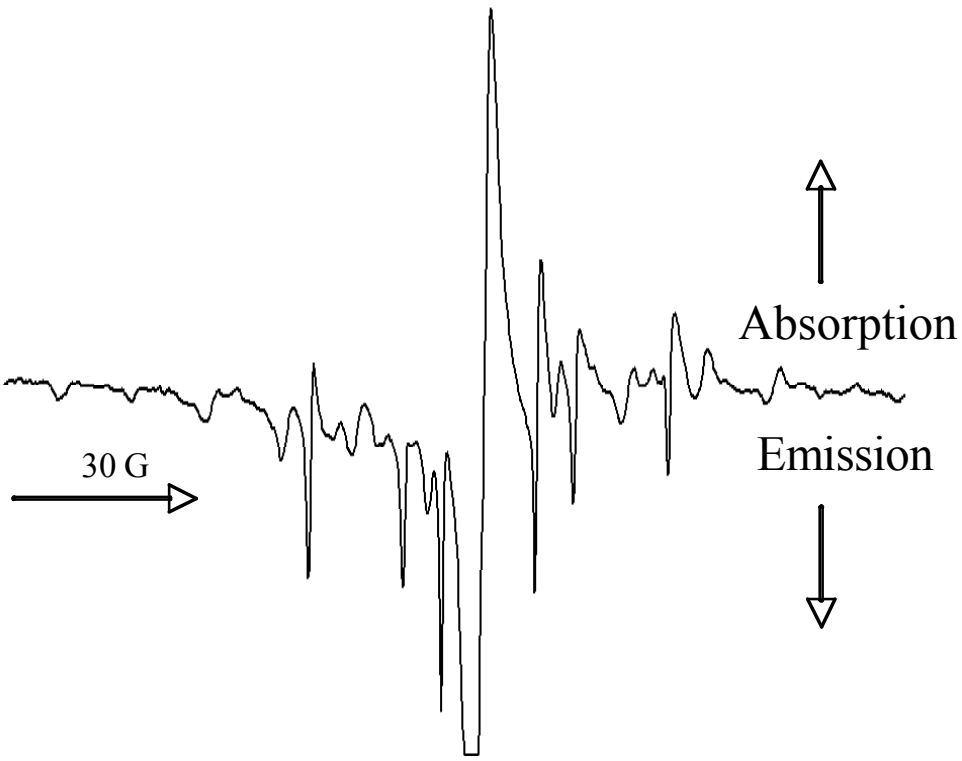

Figure 6.1: X–band TREPR spectrum obtained 500 ns after 308 nm laser irradiation of AQDS in AOT reverse micelles of radius 30Å.

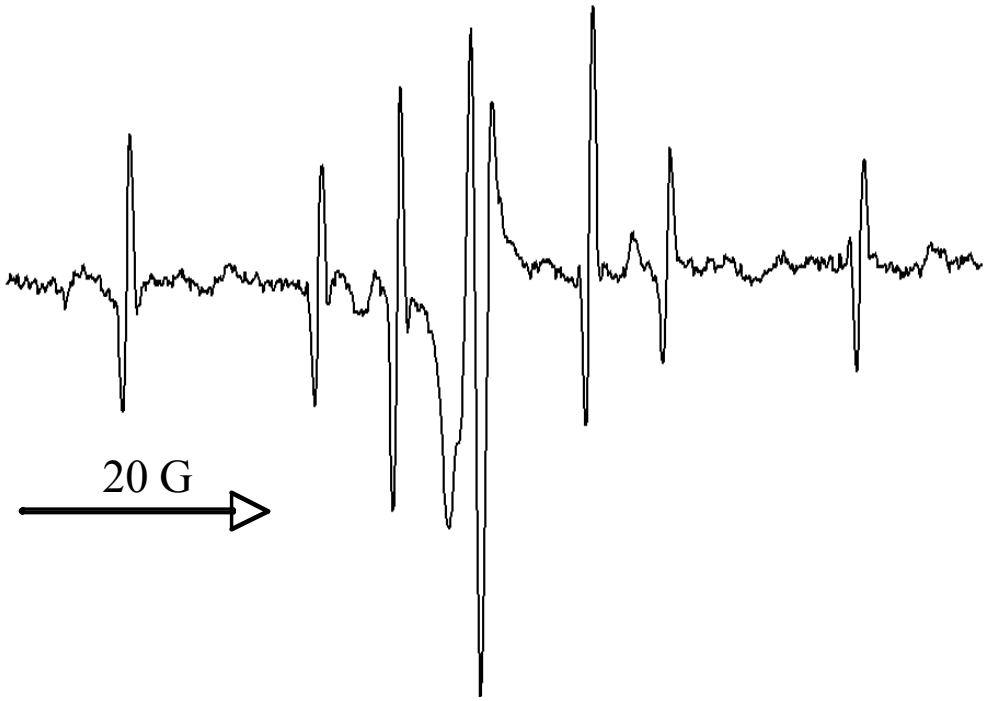

Figure 6.2: X-band TREPR spectrum of the same system as in Figure 6.1, acquired at a slower scan rate and 50 G sweep width. The peripheral transitions in Figure 6.1 are not shown on this scale.

but the centermost signal appears as a superposition of at least two different carriers with different polarization patterns. One strong emissive transition is superimposed on a broader transition that is either SCRP polarized or may be a multiplet radical pair mechanism signal (low field E, high field A). In our earlier experiments using AQDS in AOT reverse micelles, broad E/A central lines were observed and assigned to the AQDS–• radical. Since electron transfer reactions to ^{3}AQDS* are also expected in this system and the g–factor of this signal is the same as that observed previously, we assign this broad central signal to the AQDS radical anion. Further supporting evidence for this assignment will be presented below, as is a more detailed discussion of the spin polarization pattern for this radical.

The g–factor of the net emissive singlet superimposed on the AQDS–• signal is fully consistent with that of the sulfite radical anion, $SO_3^{-\bullet}$. Sodium sulfite is a common residual impurity from the synthesis of AOT, and the anion is known to absorb strongly at 308 nm. The photochemistry of sulfite anion is electron ejection from the triplet state to give the $SO_3^{-\bullet}$ radical and a solvated electron, which has been extensively studied by Jeevarajan and Fessenden. We do not observe the solvated electron signal because its chemical lifetime in solution is quite short unless the solvent is ultra pure water and there no other species are present. This is obviously not the case for our samples. The magnitude of the CIDEP polarization from $SO_3^{-\bullet}$ is very strong and therefore even a small amount of this impurity is likely to be detectable. Turro and Khudyakov added additional sodium sulfite to their AOT solutions and for this reason the $SO_3^{-\bullet}$ radical was the major signal carrier in their spectra. The position of their signal from this species and our match perfectly, and both datasets are in agreement with the g–factor measurement published by Jeevarajan and Fessenden.

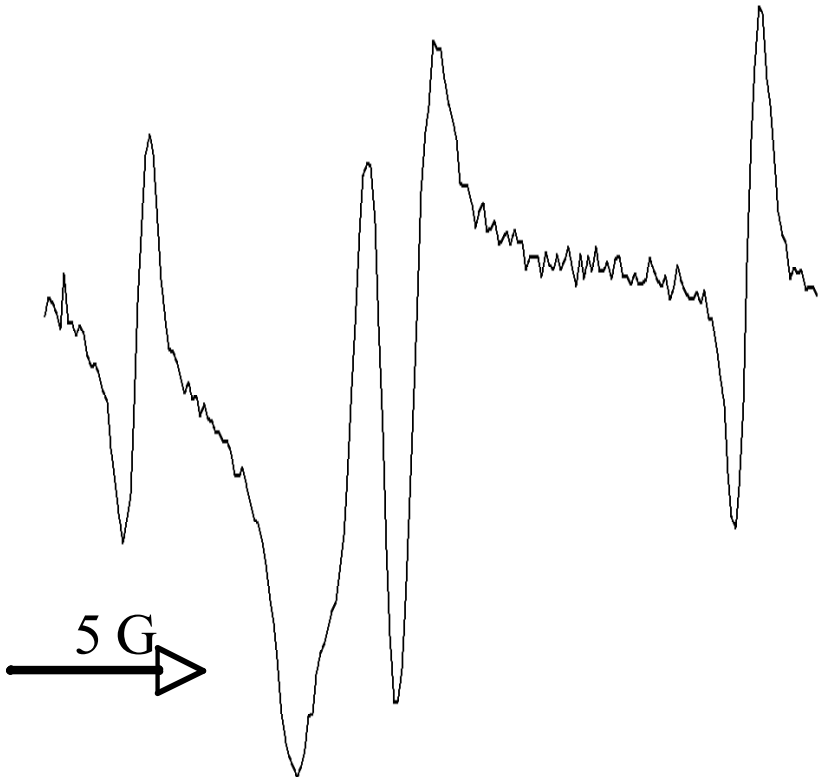

Figure 6.3: Same as Figure 6.2, except again a slower scan rate was used to collect the spectrum and the sweep width is 20 G.

It is possible that, because of the use of a GaAs FET microwave amplifier in the signal arm of our spectrometer system, we are more sensitive to the presence of sulfite radical anions and other radical species than were Turro and Khudyakov. We note here one other large difference between our work and theirs: we have very few RMs containing more than one AQDS molecule. Based on their concentration information, they had multiple AQDS molecules in the same RM for most experiments. The exact manifestation of this large AQDS concentration in the TREPR spectral appearance is not immediately clear, but this may be a possible reason why we observe many other radicals from AOT in our experiments.

The g–factor of AQDS–• in aqueous solution has been accurately determined by Sauberlich et al.[39] and is used in these studies, along with the $SO_3^{-\bullet}$ radical, as references to estimate the g–factors of the other observed radicals. The origin of the AQDS–• radical ion in these spectra provides an important clue as to the identity of one of the other signal carriers. If AQDS is acting as an electron acceptor, there must be a donor species that loses an electron to become paramagnetic. Furthermore, the donor radical must share the same polarization pattern (TM, RPM or SCRP) as the signal from the AQDS–•. Based on the time dependence of the AQDS–• signal, which will be presented and discussed below, we contend that the AQDS–• signal is strongly SCRP polarized, and therefore one of the other SCRP polarized radicals comes from the donor. Because the donor and acceptor radicals are coupled via the spin exchange interaction responsible for the SCRP pattern, they should also share similar line widths. The AQDS–• radical has many hyperfine lines which can eventually be resolved by detecting at later delay times (see time dependence discussion below). The line width of the AQDS–• signal matches well with that observed in the E/A

doublets at the edges of the expanded spectrum in Figure 6.3. For reasons to be presented below, we assign this signal to alkyl radical **6.1**. Table 1 lists all radical structures and simulation parameters.

The hyperfine splitting pattern of radical **6.1** is a triplet of doublets. This is consistent with an unpaired electron split by two sets of inequivalent protons (3 protons total). The only structure with these parameters that can logically be created from this photochemistry is free radical **6.1**. These results suggest that the AOT sulfonate head group is in fact the donor moiety, first forming a neutral RSO_3• structure by electron transfer to ^{3}AQDS*. This species then eliminates a closed shell SO_3 molecule to form radical **6.1**, as outlined in Scheme 6.2. We were not able to find examples of photo–sensitized sulfonate photo–oxidation in the literature, nor of loss of SO_3 to create carbon centered radicals. In pulse radiolysis experiments on AOT RMs, Gebicki and Bednarek reported loss of $SO_3^{-\bullet}$ after electron attachment to the ester group of AOT, but this is not an expected pathway in our oxidative conditions unless there is a source of donor electrons. The only possible source of electrons would be from sulfite photo–oxidation, which we know is minimal. While oxidation of anions such as the AOT head group is a likely pathway in the presence of strong oxidants like ^{3}AQDS*, this reaction appears to have no precedent in the literature. For this reason we sought confirmation of this chemistry through CIDNP experiments.

6.2.2 CIDNP Results

Figure 6.4A shows a dark NMR spectrum of 30 Å RMs made from AOT and n–hexane. The peaks corresponding to the protons nearest the head group of the AOT molecule are clearly seen. In these experiments the AQDS concentration is relatively low (0.1 mM) in

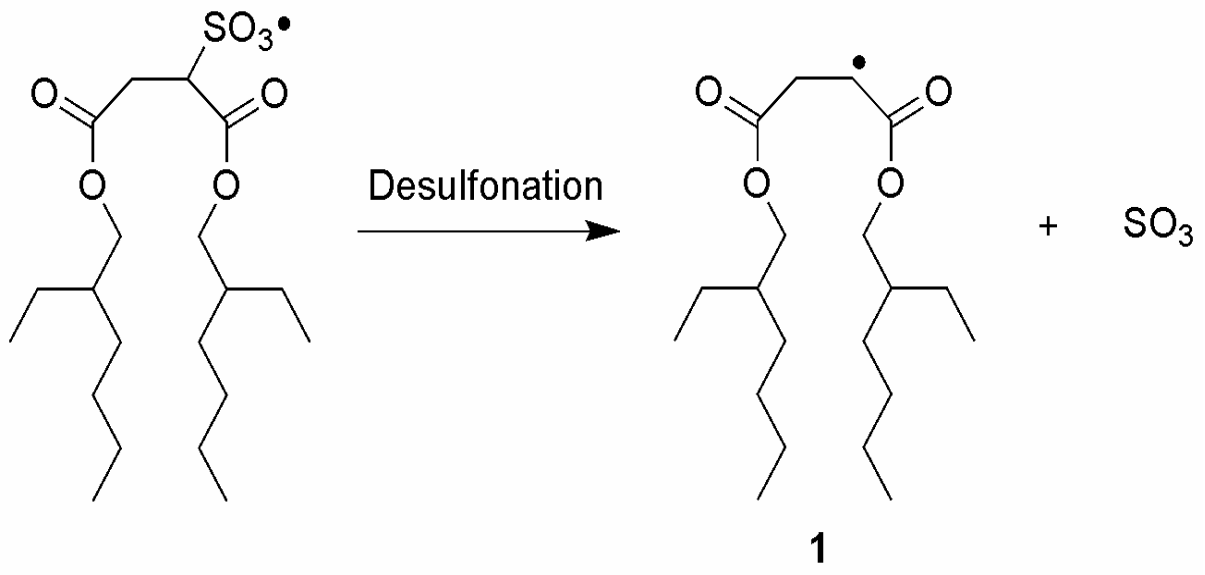

Scheme 6.2: Desulfonation of sulfite radical to form radical **6.1** and SO_3.

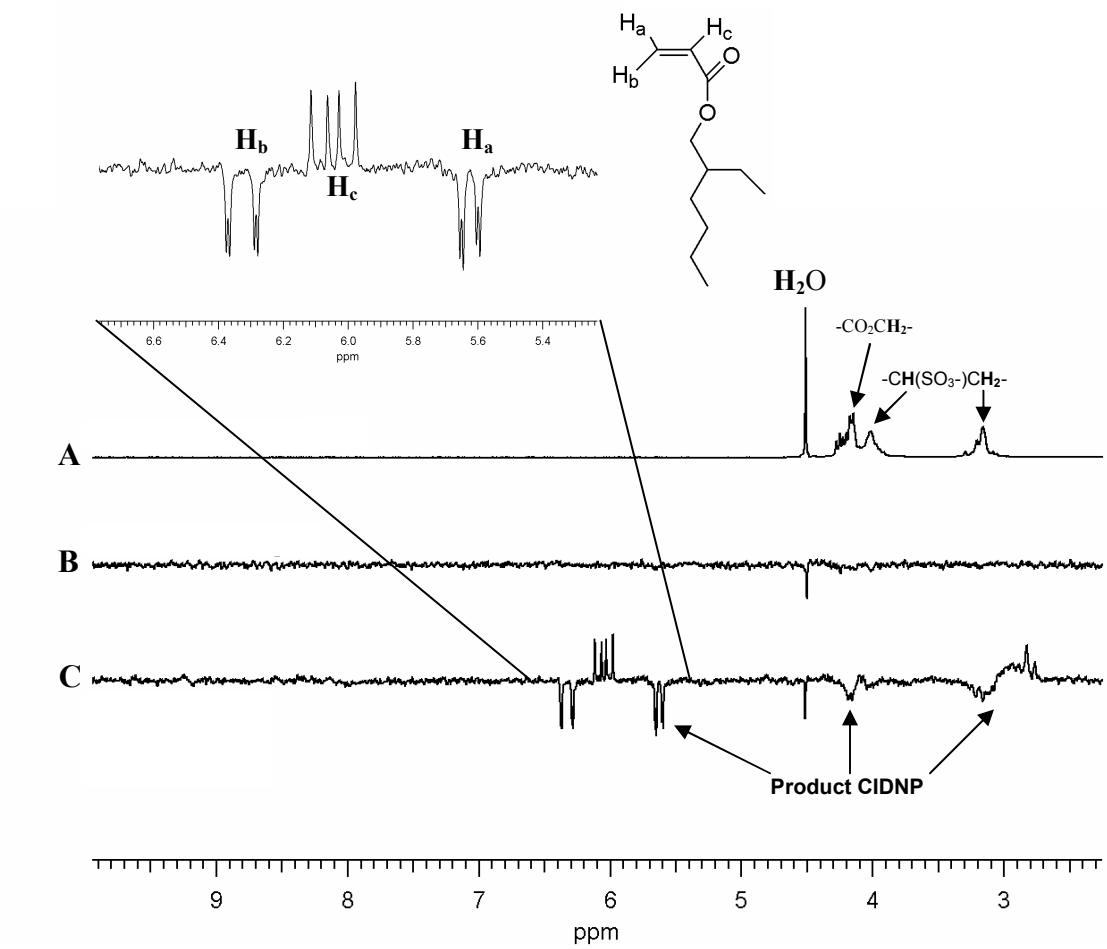

Figure 6.4: ^{1}H NMR spectrum of AQDS in a 30 Å AOT RM a) before laser pulse without pre–saturation pulse sequence, b) before laser pulse with pre–saturation, and c) 10 μs after laser pulse with pre–saturation.

comparison to that of AOT and is not observed. Figure 6.4B shows the same spectrum under pre–saturated conditions, necessary to block unwanted dark signals from the CIDNP spectrum. Figure 6.4C shows a pre–saturated NMR spectrum taken 10 μs after the sample has been irradiated with a 308 nm excimer laser pulse. Strong CIDNP signals can be seen in the 2.5 to 6.5 ppm region. The first set of CIDNP lines at 5.5–6.5 ppm shows three sets of doublets characteristic of a terminal alkene. The doublet at 5.6 ppm corresponds to H_a (see Figure 3 inset spectrum with the alkene structure), the doublet at 6.0 ppm corresponds to H_c, and the signal at 6.1 ppm corresponds to H_b. The chemical shifts as well as the measured J coupling values (H_{ab} (2.1 Hz), H_{ac} (10.2 Hz), H_{bc} (17.3 Hz) match up well with literature values for terminal alkenes with an ester substituent.[102]

The other CIDNP signals shown in Figure 6.4C are less intense than those in the vinyl region, but structural assignments are still possible. The negative peak at 4.2 ppm is attributed to the highlighted methylene protons in the regenerated AOT molecule shown in Scheme 6.3 because it is in the same position as those in the starting material. The E/A multiplet polarization of the transitions from 2.9–3.1 ppm can be attributed to the desulfonated saturated product that can be formed in competition with alkene formation (Scheme 6.3a). The acyl radical that results from the elimination reaction in Scheme 6.2 is not observable in either the TREPR or CIDNP experiments. The reaction is too slow to make it observable within the electron spin relaxation time (known to be short for acyl radicals) by TREPR, and, because the radical does not contain any hyperfine interactions, it will not acquire nuclear spin polarization of any great magnitude in the products it forms. These products are likely to be aldehydes and no signals in this region of the NMR spectrum of the products were observed.

Along with product information obtained by analyzing the chemical shifts of the CIDNP polarized protons, the phases of these transitions support the assigned radical structures. The signs of the alkene proton transitions are dictated by the hyperfine coupling to the radical that forms the alkene product. The signs of CIDNP transitions are dictated by Kaptein's Rules[103] which have been reviewed by Salikhov et al.[104] The elimination reaction creating the alkene product is shown in Scheme 6.3. The signs of β hyperfine interactions are known to be negative, and therefore the NMR transitions for both H_a and H_b are emissive. The signs of α hcc's are known to be positive, and therefore the H_c peak is absorptive. When the alkene product is formed by elimination of an oxyl–acyl radical, the resulting NMR signals have positive and negative phases. These phases are predicted for an escape product produced directly from radical **6.1** (g–factor = 2.00274), which has a lower g–factor than that of AQDS–• (g–factor = 2.00410).

The intensity of the CIDNP polarized signal is directly proportional to the magnitude of the hyperfine interactions, so presumably the AQDS signal is not observed in these spectra because of the small hcc values of its aromatic protons. Figure 6.5 shows the regeneration of starting material by hydrogen abstraction. The product has two protons that are coupled to the radical center. They are β to the tertiary radical **2** center, and therefore have negative hcc values, which will produce negative CIDNP signals if AOT molecule is regenerated via H–abstraction. The chemical shifts of these transitions matches literature values for protons β to ester moieties. Multiplet polarization is common occurrence in reactions that form products with equivalent protons from radicals that have protons that are non–equivalent and have different hyperfine phases and magnitudes. This is exactly the case for radical **1** (see Figure 5A)**.** The β protons have an hcc of –15.7 G, while the α protons have hcc's of 22.1 G**.**

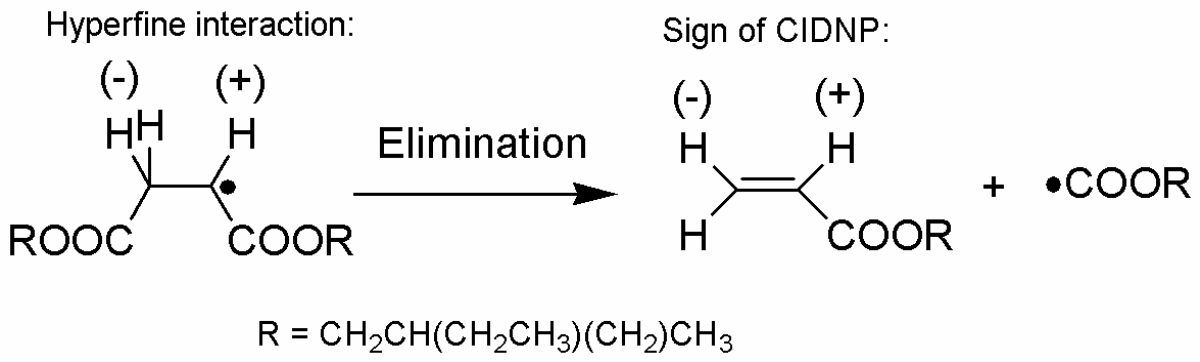

Scheme 6.3: Formation of alkene by radical elimination.

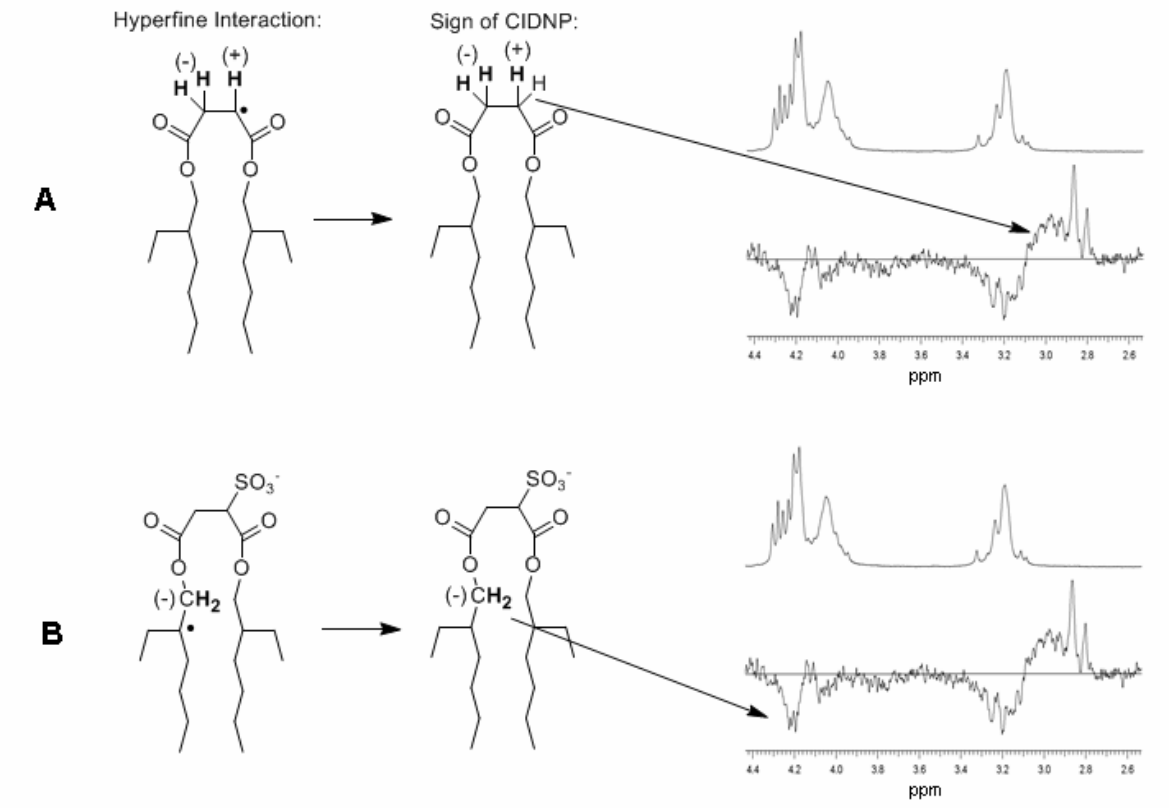

Figure 6.5: Radical termination by H–abstraction A) to form the product from loss of SO_3, and B) to re–form starting material with CIDNP polarized protons. The top spectra shown in A and B are NMRs of the starting material, the bottom ones are the CIDNP spectrum taken after the laser pulse.

Figures 6.1 and 6.2 also show peripheral broader peaks that we attribute to carbon–centered radicals formed via hydrogen atom abstraction by ^{3}AQDS*. These signals are significantly less intense than those from radical **6.1**, AQDS–• or SO_3^-•. The counter radical expected from this photochemistry is of course the ketyl radical of AQDS (AQDSH•), which is the conjugate acid of AQDS–•. The pKa of this radical is 3.9 and the pH of a solution of AQDS is about 5.5, therefore we expect the AQDSH• radical to deprotonate rapidly in our system and not be observed. By spectral simulation with reasonable hyperfine coupling constants we assign the broad perimeter lines in Figures 6.1 and 6.2 to structures **6.2** and **6.3**, which are tertiary and secondary carbon–centered radicals, respectively (see Table 1 for simulation parameters). Radical **6.2** can only be formed from via H–abstraction from the tertiary carbon on the AOT tail. Each transition associated with radical **6.2** is an E/A doublet, which is due to SCRP polarization. The line width used in our simulation of **6.2** is 3.0 G, which is reasonable for a tertiary radical having a lower degree of rotational freedom.

Radical **6.3** is a secondary radical, and a glance at Scheme 6.1 shows ten different H–atom abstraction sites, leading to five different possible secondary radicals that could be formed on the AOT hydrocarbon chain. Interestingly, our simulation shows that radical **6.2** is the only secondary radical giving rise to this signal. We know this because it is the only secondary radical that will give a doublet of quintets from one α hyperfine interaction and four equivalent (or near equivalent) β hyperfine interactions. We note here that the β protons in this radical are diastereotopic, however we do not see any manifestation of this in the simulation, most likely because any differences in coupling constant due to diastereotopicity are small and within the line width (about 1.4 G). It is possible that the reason we observe only radical **6.2** from secondary abstraction sites is that this site is kinetically favored. Also,

Radical	Structure	g-factor	hyperfine coupling constants	Simulation Linewidth	Simulation CIDEP	- J
AQDS-•	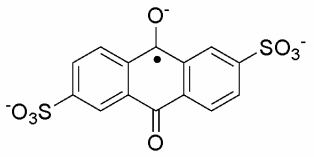	2.0041	$2(H_{3,7})$ = 1.2 G $4(H_{1,4,5,8})$ = 0.4 G	1.1 G	SCRP	0.3 G
SO_3-•	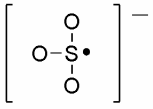	2.0033	—	1.0 G	TM	—
6.1	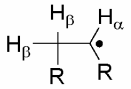	2.0027	H_α = 22.1 G $2(H_\beta)$ = 15.7 G	0.5 G	SCRP	0.3 G
6.2	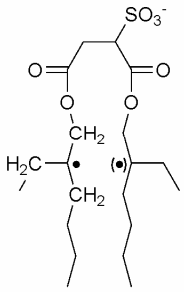	2.0026	$6(H_\beta)$= 22.8 G	3.0 G	SCRP	0.6 G
6.3	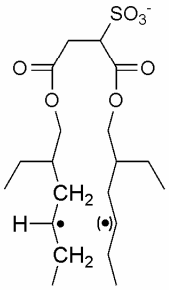	2.0026	H_α = 22.1 G $4(H_\beta)$ = 24.5 G	1.4 G	RPM	—

Table 6.1

it has a different number of coupling constants compared to radical **6.3** and therefore its TREPR transitions do not overlap with any other signals. If H–atom abstraction were to take place at the penultimate carbon atoms of the AOT alkyl chain, the ensuing radicals would have the same number of coupling constants of similar magnitude to radical **6.1** and would most likely be buried under that signal.

The mechanism of formation of radicals **6.2** and **6.3** is worthy of some discussion. It is unlikely that it is formed via the migration of the doubly–charged AQDS into the hydrophobic lamellar region. It is more likely that the singly–charged AOT molecule diffuses into the water pool interior for a short time. Such penetration of single surfactant molecules into the aqueous phase is well documented in the literature for normal micelles and should be expected in reverse micelles as well.

6.2.3 Summary of Radical Structures

Figure 6.6 shows the same expanded spectrum as in Figure 6.2, and below it a computer simulation accounting for radicals **6.1–3**, $AQDS^{-}\bullet$, and $SO_3^{-}\bullet$. All simulation parameters are listed in Table 6.1. The parameters for the $AQDS^{-}\bullet$ and $SO_3^{-}\bullet$ agree with previously published values. Alkyl radicals **6.1–3** are reported here for the first time. Their g–factors, hyperfine coupling constants and line widths are all in line with expectations for secondary and tertiary carbon–centered alkyl radicals. As mentioned above, the values for the exchange interaction J are reported only because they were used to obtain proper simulation of the line shape of SCRP polarized signals. Without micro–reactor model simulations, no significance beyond the fact they are of the correct sign and magnitude for such systems should be inferred. Such simulations are outside the scope this chapter.

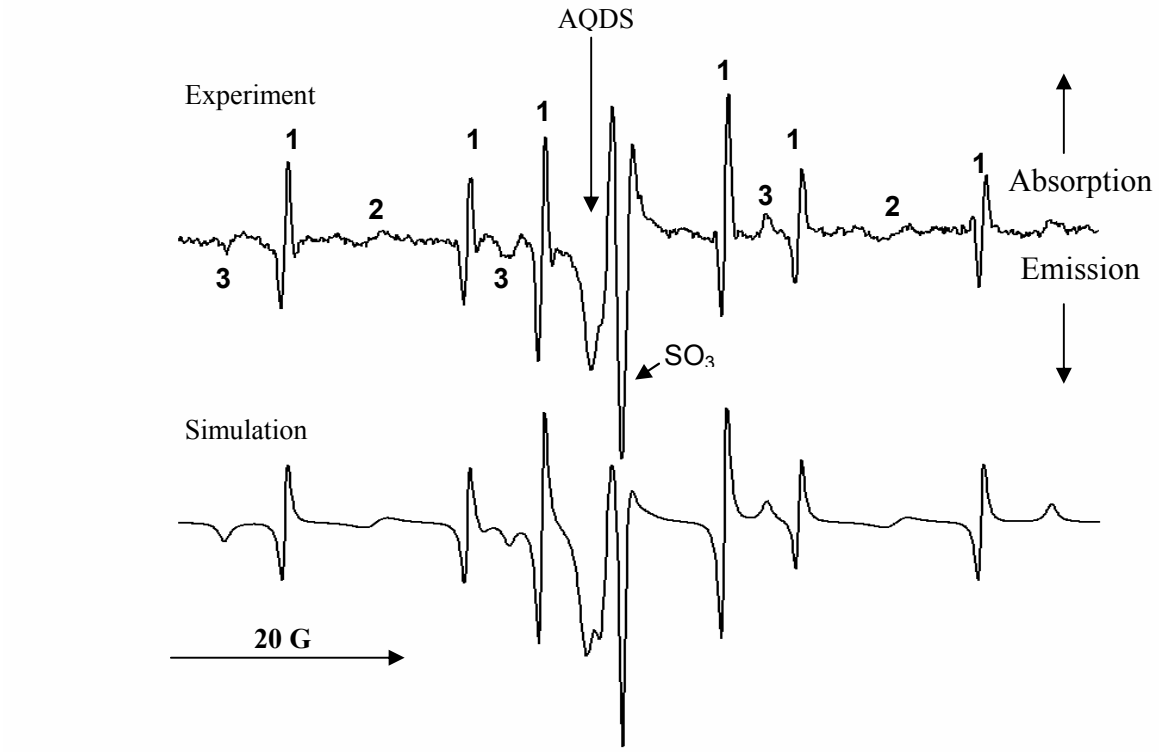

Figure 6.6: TREPR spectrum (top) taken 500 ns after irradiation of AQDS inside of a 30 Å RM. The transitions are labeled by radical number. The magnetic parameters used in the simulation (bottom) of each radial are shown in Table 6.1.

6.2.4 TREPR Time Dependence

Figure 6.7 shows the time dependence of the central part of the TREPR spectrum from the AQDS/AOT system for two different sizes of RM. For large RMs (radius of 56 Å, right side of Figure 6.7), the only radicals observed are $AQDS^{-}\bullet$, and $SO_3^{-}\bullet$. At the earliest delay time (300 ns) after the laser flash, only the $AQDS^{-}\bullet$ ion, spin polarized E/A by the radical pair mechanism, is observed, and it is broad and featureless. At 500 ns the sulfite radical is observed, and as later delay times are probed the $AQDS^{-}\bullet$ signal becomes more highly resolved and more intense. The increase in spectral resolution is normal for TREPR experiments, where uncertainty broadening at early delay times is common. It should be noted that with better resolution, the individual E/A doublets of the SCRP mechanism are easily observed. With smaller RMs (radius 21 Å, left side of Figure 6.7), the surfactant molecules are closer to the AQDS and radical **6.1** from the AOT head group oxidation reaction begins to appear at the perimeter of the spectrum. It is possible that, without significant oxidation of the head group in 56 Å RMs, the $AQDS^{-\bullet}$ is produced along with the $SO_3^{-}\bullet$ as a direct photo–induced electron transfer pathway. A final comment about the time dependence is that for both sizes of RM, TREPR intensities decrease at very long delay times, consistent with T_1 relaxation on the microsecond time scale.

6.2.5 RM Size Dependence

The location and mobility of the radicals can be examined by collecting TREPR spectra as a function of RM size. Figure 6.8A shows the radicals formed inside a relatively large water pool with 56 Å radius. It is clear that the major paramagnetic species observed are $AQDS^{-}\bullet$, and $SO_3^{-}\bullet$. In this spectrum, the peripheral lines attributed to radical **6.1** are

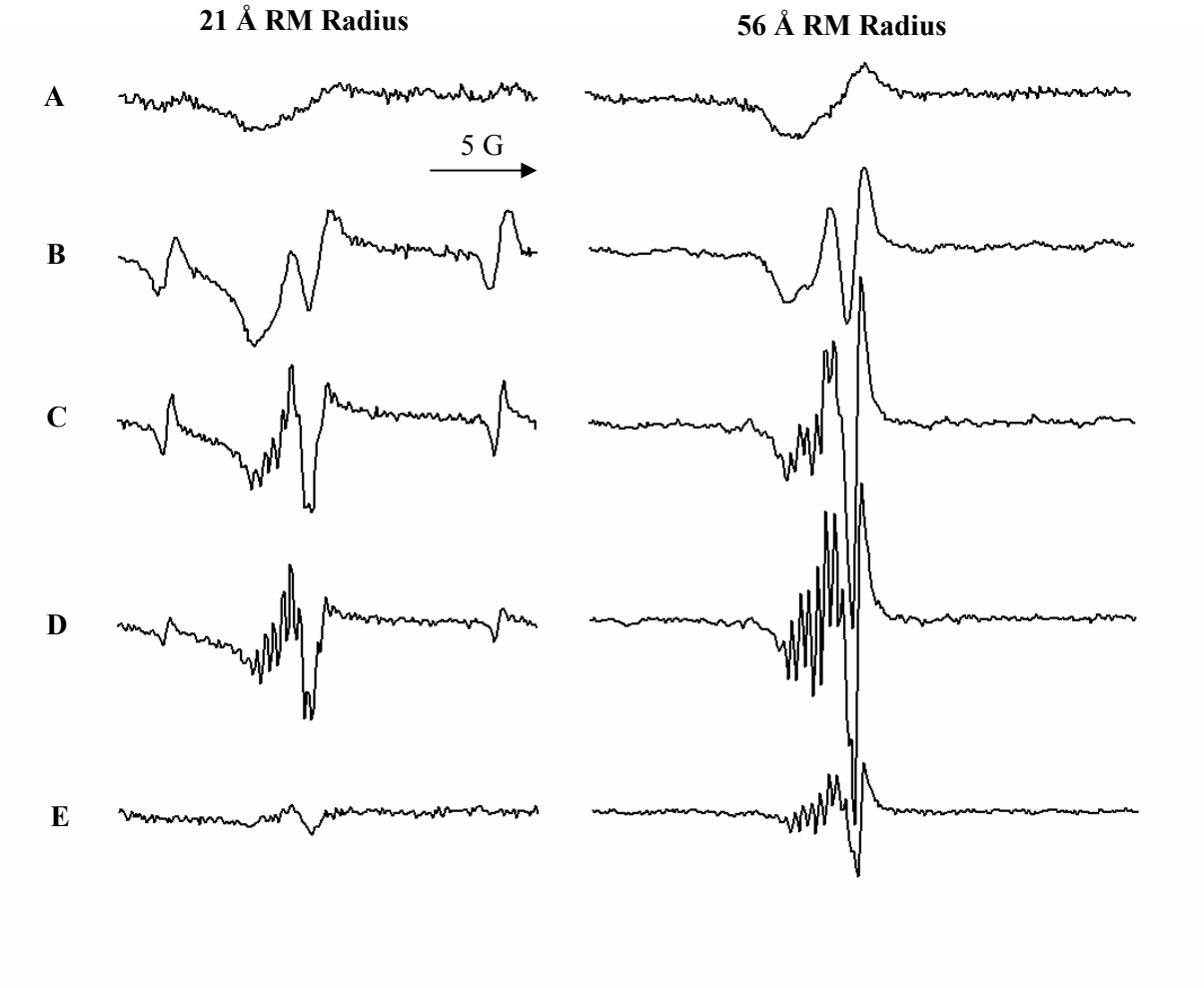

Figure 6.7: TREPR spectra produced upon irradiation of AQDS inside an 21 Å radius and 56Å radius AOT RM's with 355 nm laser pulse (25 mJ/pulse) at A) 300 B) 500 C) 1100 D) 1500 and E) 4000 ns.

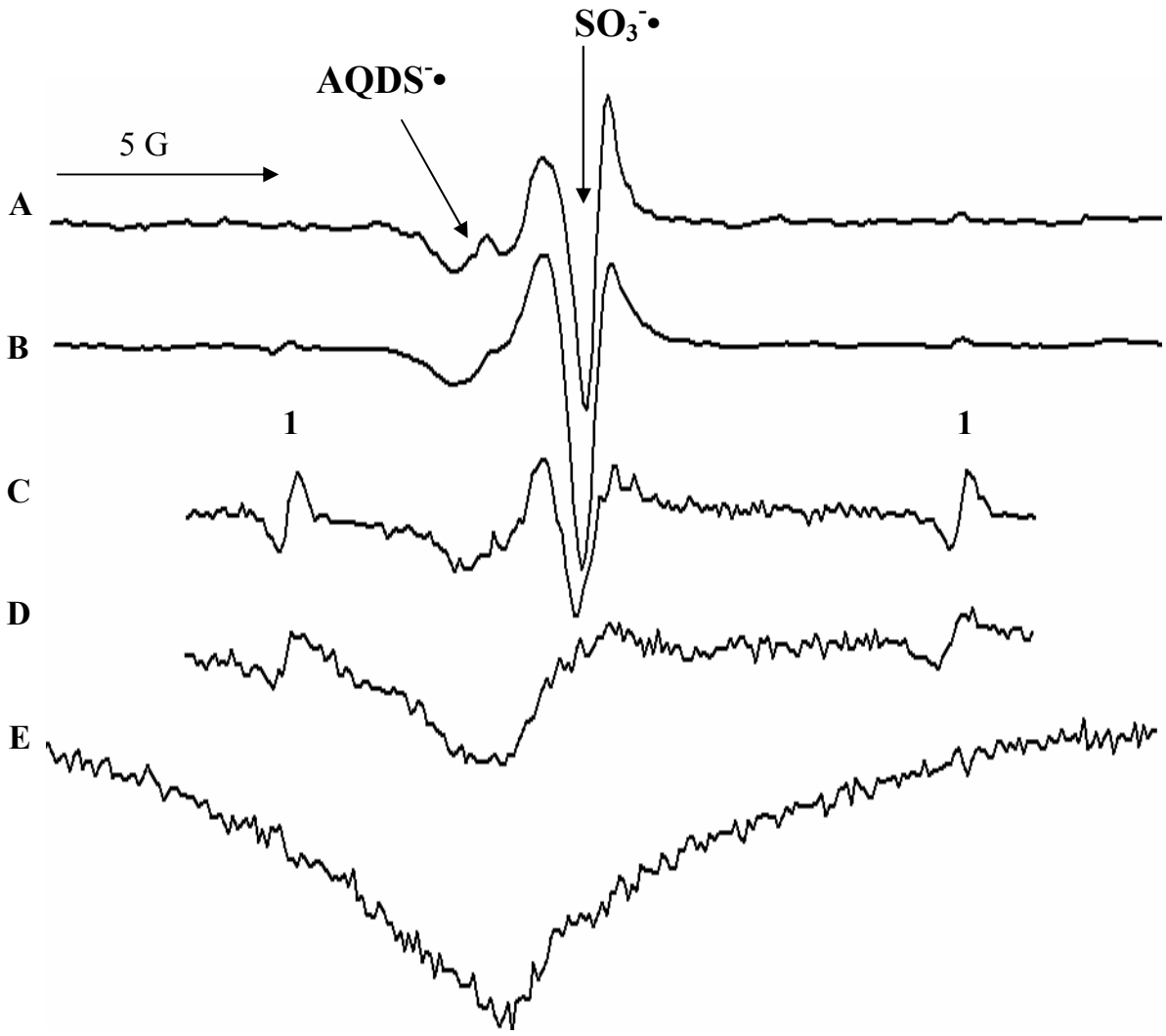

Figure 6.8: TREPR spectra taken 900 ns after irradiation of AQDS with 355 nm laser light (25 mJ/pulse) in reverse microemulsions with water pool radii of A) 56 Å B) 42 Å C) 21 Å D) 14 Å and E) 7 Å.

barely observable. In a slightly smaller RM, represented by Figure 6.8B, the peripheral lines due to radical **6.1** become more apparent. As the size of the RM decreases in Figures 8A–E, the ratio of the signal intensities from SO_3^{-}• and radical **6.1** decreases until SO_3^{-}• is no longer observed (Figure 6.8D). The line widths of each transition also broaden as the RM size decreases until we reach a water pool radius of 7 Å, where only a broad transition due to AQDS–•, polarized by the TM, is observable.

The changes in intensity of the radical **6.1** signal with RM size are a function of its location. Radical **6.1** is a neutral secondary radical that is created at the interface of the water pool with the surfactant. Because it carries no net charge, it can easily diffuse out of the water pool. The doubly charged AQDS–• is restricted to the water pool, and in large RM's (radius > 40 Å) the inter–radical distance between AQDS–• and **6.1** is too far for appreciable spin exchange (and SCRP) to occur. This lowers the overall spin polarization magnitude. As the water pool gets smaller, this situation changes. In RM's with a radius of less than 40 Å, the two radicals are close enough together to acquire strong SCRP polarization and their signals are enhanced.

The signal from $SO_3^{-\bullet}$ shows the opposite trend. Its intensity decreases with RM size and this is because of its location in the interior of the water pool. The SO_3^{-}• is emissively polarized mostly by the TM and is on average closer to $AQDS^{-}$• than radical **6.1**. As the size of the water pool decreases, the SO_3^{-}• signal broadens and decreases in intensity. A similar phenomenon has been observed by Turro et al. in studies with SO_3^{-}• in AOT RM's,[78] and also in our previous studies on the oxidation of diglycine in AOT water pools.[94] It is most likely a consequence of relaxation due to anisotropic zero field splitting of the radical pairs within the micelles.

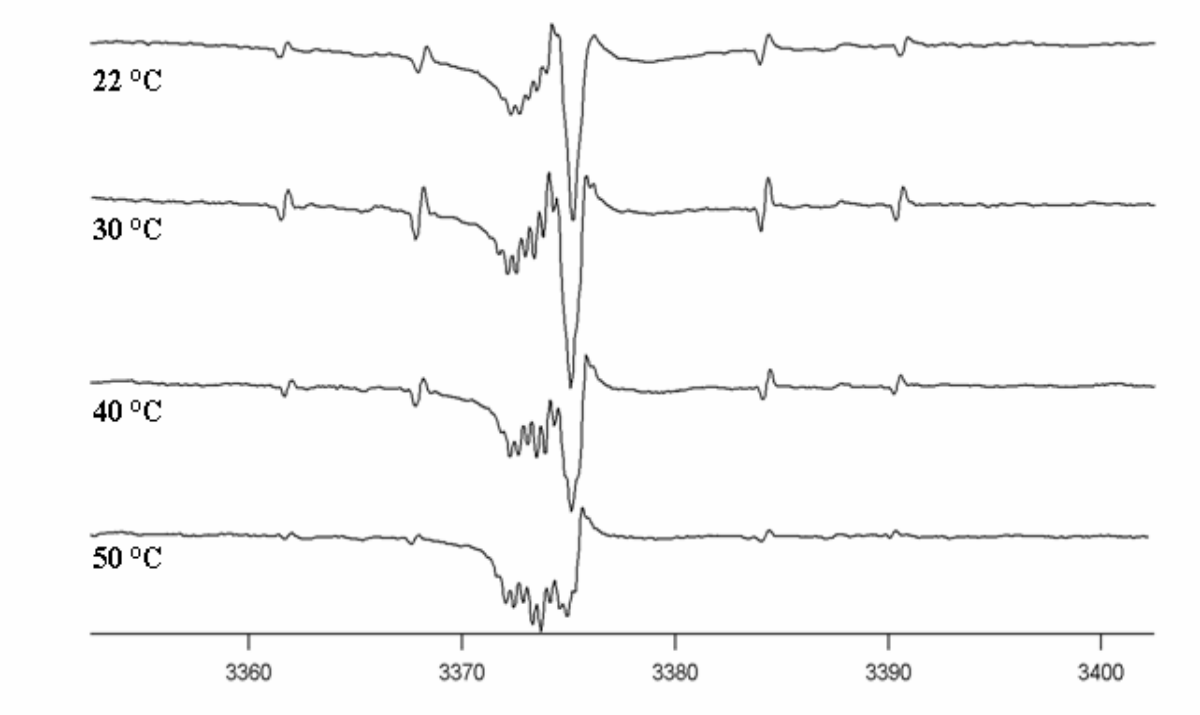

Figure 6.9: X–Band TREPR spectra of AQDS in 30 Å radius AOT RM's at different temperatures.

6.2.6 Temperature Dependence

The J value between members of a radical pair is affected by the rate of re–encounters. In general, by increasing the temperature, radical diffusion will increase, and the average J value should also increase. Figure 6.9 shows TREPR spectra at four different temperatures. There are signals from AQDS^{-}•, SO_3^{-}•, and radical **6.1** present in all spectra. The first two spectra, acquired at room temperature and at 30 °C, are fairly similar with relatively intense APS structure in both AQDS–• and **6.1** signals. The signal from SO_3^{-}•, appears to be completely in emission, polarized by the TM or net RPM. The situation begins to change at 40°C as the AQDS–• peaks become more emissive, while the signals from SO_3^{-}• and radical **6.1** decrease in intensity. At 50 °C, the AQDS^{-}• is emissive while the SO_3^{-}• is absorptive, and the signal from radical **6.1** is diminished.

Radical **6.1** is neutral and resides on the water/surfactant interface. It can be assumed that an increase in temperature would increase the diffusion rate, and its distance from the AQDS–•. This would reduce the SCRP polarization intensity between AQDS–• and **6.1**. At 50 °C, AQDS–• is only polarized by its interaction with SO_3^{-}•. The AQDS–• and SO_3–• signals appear to be polarized by the CIDEP radical pair mechanism (RPM). In net RPM polarization of radicals formed from a triplet precursor, AQDS–• would be in emission due to its higher g–factor, while the partner would be absorptive. The simultaneous decrease in SCRP polarization for both the AQDS–• and radical **6.1** signals is expected as these are the only two radicals in this region of the whole spectrum that are SCRP polarized.

6.3 Conclusions

The AOT surfactant exhibits a rich chemistry in the presence of a strong photo–oxidant. We have presented unambiguous assignments for several radicals arising from both electron transfer and hydrogen atom abstraction reaction pathways. Additionally, we have observed sulfite anion radicals from a separate photo–oxidation process involving residual Na_2SO_3 in the AOT samples. Qualitative analysis of the CIDEP polarization patterns has allowed an estimate of the relative positions of the radicals with regard to hydrophobic vs. hydrophilic regions of the RMs. Future work will include quantification of the exchange interaction and diffusion parameters of these radicals, as well as an exploration of AOT water–based micelles in comparison to RMs.

6.4 Experimental

TREPR Experiments. All experiments were performed on a JEOL EPR console and bridge modified with a fast preamplifier and a low noise GaAs FET microwave amplifier (25 dB gain). The sample in experiments performed on the JEOL spectrometer were irradiated by a 308 nm laser pulse (20ns width, ~40 mJ, repetition rate: 60 Hz) from an excimer laser (Lambda Physik LPX100i). Spectra were collected at a fixed delay time after the laser flash using a Stanford Research Systems boxcar integrator (100 ns gates), and the external field was swept over 2 or 4 minutes. The microwave power incident on the samples was 10 mW for all experiments. The isooctane solutions containing the reverse micelles were bubbled with N_2 for 30 minutes before and during circulation through a quartz flow cell of path length 1.0 mm centered in a rectangular brass TE_{103} cavity. Spectra were created using both 308 nm and 355 nm excitation and were found to be identical. The 355 nm TREPR experiments

were performed on a Bruker ER046 spectrometer. Spectra were collected in the time domain with a Lecroy oscilloscope. The 355 nm irradiation was generated from a Continuum Nd:YAG Spectra Physik Quantum Ray GCR–18 pulsed at 10 Hz (8 ns pulse length).

TR–CIDNP Experiments. All CIDNP experiments were performed in hexane on a Bruker 200 MHz NMR spectrometer equipped with a special probe and quartz light guide. The sample was irradiated with 308 nm laser pulses from an LPX100 excimer laser. The samples were irradiated with a radio frequency pulse sequence to pre–saturate the dark NMR transitions from the starting material.

BIBLIOGRAPHY

(1) Davies, M. J. *Biochim. Biophys. Acta* **2005**, *1703*, 93.

(2) Butterfield, D. A.; Boyd-Kimball, D. *Biochim. Biophys. Acta* **2005**, *1703*, 149.

(3) Clementi, M. E.; Martorana, G. E.; Pezzotti, M.; Giardina, B.; Misiti, F. *Int. J. Biochem. Cell Biol.* **2004**, *36*, 2066.

(4) Hou, L.; Shao, H.; Zhang, Y.; Li, H.; Menon, N. K.; Neuhaus, E. B.; Brewer, J. M.; Byeon, I.-J. L.; Ray, D. G.; Vitek, M. P.; Iwashita, T.; Makula, R. A.; Przybyla, A. B.; Zagorski, M. G. *J. Am. Chem. Soc.* **2004**, *126*, 1992.

(5) Davies, M. J.; Truscott, R. J. W. *J. Photochem. Photobiol. B: Biology* **2001**, *63*, 114.

(6) Kantorow, M.; Hawse, J. R.; Cowell, T. L.; Benhamed, S.; Pizarro, G. O.; Reddy, V. N.; Hejtmancik, J. F. *Proc. Nat. Acad. Sci.* **2004**, *101*, 9654.

(7) Varadarajan, S.; Yatin, S.; Kanski, J.; Jahanshahi, F.; Butterfield, D. A. *Brain Research Bulletin* **1999**, *50*, 133.

(8) Davies, K. J. A. *J. Biol. Chem.* **1987**, *262*, 9895.

(9) Chao, C.; Ma, Y.; Stadtman, E. R. *Proc. Nat. Acad. Sci.* **1997**, *94*.

(10) Forbes, M. D. E. *Photochem. Photobiol.* **1997**, *65*, 73.

(11) Atkins, P. W.; Evans, G. T. *Mol. Phys.* **1974**, *27*, 1633.

(12) Salikhov, K. M.; Molin, R. Z.; Sagdeev, R. Z.; Buchachenko, A. L. Magnetic Spin Effects in Chemical Reactions. In *Magnetic Spin Effects in Chemical Reactions*; Elsevier: Amsterdam, 1984; pp 57.

(13) Closs, G. L.; Forbes, M. D. E.; Norris, J. R. *J. Phys. Chem.* **1987**, *91*, 3592.

(14) Vuolle, M.; Makela, R. J. *J. Chem. Soc., Faraday Trans. 1* **1987**, *83*, 51.

(15) Muus, L. T.; Atkins, P. W.; McClaughlan, K. A.; Pedersen, J. B. *Chemically Induced Magnetic Polarization*; Reidel: Dordrecht, **1977**.

(16) Hayon, E.; Ibata, T.; Lictin, N. N.; Simic, M. J. *J. Phys. Chem.* **1972**, *76*, 2072.

(17) Loeff, I.; Treinin, A.; Linschitz, H. *J. Phys. Chem.* **1983**, *87*, 2536.

(18) Buxton, G. V.; Greenstock, C. L.; Helman, W. P.; Ross, A. B. *J. Phys. Chem. Ref. Data* **1988**, *17*, 513.

(19) Clancy, C. M. R.; Forbes, M. D. E. *Photochemistry and Photobiology* **1999**, *69*, 16.

(20) Burns, C. S.; Rochelle, L.; Forbes, M. D. E. *Organic Letters* **2001**, *3*, 2197.

(21) Morozova, O. B.; Yurkovskaya, A. V.; Tsentalovich, Y. P.; Forbes, M. D. E.; Sagdeev, R. Z. *J. Phys. Chem. B* **2002**, *106*.

(22) Kominami, S. *J. Phys. Chem.* **1972**, *76*, 1729.

(23) Kawatsura, K.; Ozawa, K.; Kominami, S.; Akasaka, K.; Hatano. *Radiat. Eff. Defects Solids* **1974**, *22*, 267.

(24) Naito, A.; Kominami, S.; Akasaka, K.; Hatano, H. *Chem. Phys. Lett.* **1977**, *47*, 171.

(25) Asmus, K. D.; Goebl, M.; Hiller, K. O.; Mahling, S.; Moenig, J. *J. Chem. Soc., Perkin Trans. 2* **1985**, *5*, 641.

(26) Naito, A.; Akasaka, K.; Hatano, H. *Mol. Phys.* **1981**, *44*, 427.

(27) Bobrowski, K.; Hug, G. L.; Marciniak, B.; Kozubek, H. *J. Phys. Chem.* **1994**, *98*, 537.

(28) Bobrowski, K.; Schoeneich, C.; Holcman, J.; Asmus, K. D. *J. Chem. Soc., Perkin Trans. 2* **1991**, *3*, 353.

(29) Bobrowski, K.; Schoeneich, C. *Radiat. Phys. Chem.* **1996**, *47*, 507.

(30) Champagne, M. H.; Mullins, M. W.; Colson, A. O.; Sevilla, M. D. *J. Phys. Chem. A* **1991**, *95*, 6487.

(31) Tripathi, G. N. R.; Tobien, T. J. *J. Phys. Chem. A* **2001**, *105*, 3498.

(32) Schoeneich, C.; Pogocki, D.; Hug, G. L.; Bobrowski, K. *J. Am. Chem. Soc.* **2003**, *125*, 13700.

(33) Schoneich, C.; Pogocki, D.; Wisniowski, P.; Hug, G. L.; Bobrowski, K. *J. Am. Chem. Soc.* **2000**, *122*, 10224.

(34) Pogocki, D.; Serdiuk, K.; Schoeneich, C. *J Phys. Chem. A* **2003**, *107*, 7032.

(35) Huang, M.; Rauk, A. J. *J. Phys. Chem. A* **2004**, *108*, 6222.

(36) Goez, M.; Rozwadowski, J.; Marciniak, B. *Angew. Chem., Int. Ed.* **1998**, *37*, 628.

(37) Goez, M.; Rozwadowski, J. *J. Phys. Chem. A* **1998**, *102*, 7945.

(38) Korchak, S. E.; Ivanov, K. L.; Yurkovskaya, A. V.; Vieth, H. *Archivok* **2004**, *viii*, 121.

(39) Sauberlich, J.; Brede, O.; Beckert, D. *J. Phys. Chem. A* **1997**, *101*, 5659.

(40) Gilbert, B. C.; Hodgeman, D. K. C.; Norman, R. O. C. *J. Chem. Soc., Perkin Trans. 2* **1973**, *13*, 1748.

(41) Hug, G. L.; Bobrowski, K.; Kozubek, H.; Marciniak, B. *Photochem. Photobiol.* **1998**, *68*, 785.

(42) Kaba, R. A.; Ingold, K. U. *J. Am. Chem. Soc.* **1976**, *98*, 7375.

(43) Neta, P.; Fessenden, R. W. *J. Phys. Chem.* **1971**, *75*, 738.

(44) Tarabek, P.; Bonifacic, M.; Naumov, S.; Beckert, D. *J. Phys. Chem. A* **2004**, *108*, 929.

(45) Kandrashkin, Y. E.; Vollmann, W.; Stehlik, D.; Salikhov, K. M.; van der Est, A. *Mol. Phys.* **2002**, *100*, 1443.

(46) Lakshmi, K. V.; Brudvig, G. W. *Curr. Opin. Struct. Biol.* **2001**, *11*, 523.

(47) Zech, S. G.; Kurreck, J.; Renger, G.; Lubitz, W.; Bittl, R. *FEBS Lett.* **199**, *442*, 79.

(48) Akiyama, K.; Tero-Kubota, S. *J. Phys. Chem. B* **2002**, *106*, 2398.

(49) Bordwell, F. G. *Acc. Chem. Res.* **1988**, *21*, 456.

(50) Gilbert, B. C.; Trenwith, M. J. *J. Chem. Soc., Perkin Trans. 1* **1975**, *10*, 1083.

(51) Kaptein, R. *J. Chem. Soc., Chem. Commun.* **1971**, 732.

(52) Goez, M.; Sartorius, I. *J. Am. Chem. Soc.* **1993**, *115*, 11123.

(53) Roth, H. D.; Lamola, A. A. *J. Am. Chem. Soc.* **1975**, *97*, 6270.

(54) Closs, G. L.; Forbes, M. D. E.; Piotrowiak, P. *J. Am. Chem. Soc.* **1992**, *114*, 3285.

(55) Korth, H. G.; Sustmann, R.; Dupuis, J.; Groeninger, K. S.; Witzel, T.; Giese, B. *NATO ASI Series, Series C: Mathematical and Physical Sciences* **1986**, *189*, 297.

(56) Miura, Y.; Asada, H.; Kinoshita, M. *Chem. Lett.* **1978**, 1085.

(57) Rowlands, J. R.; Whiffen, D. H. *Nature* **1969**, *193*, 61.

(58) Iacona, C.; Michaut, J. P.; Roncin, J. *J. Chem. Phys.* **1977**, *67*, 5658.

(59) Mujika, J. I.; Matxain, J. M.; Eriksson, L. A.; Lopez, X. *Chemistry: Eur. J.* **2006**, *12*, 7215.

(60) Tarabek, P.; Bonifacic, M.; Naumov, S.; Beckert, D. *J. Phys. Chem. A* **2004**, *108*, 929.

(61) Kraeutler; Jaeger; Bard. *J. Am. Chem. Soc.* **1978**, *100*, 4903.

(62) Davies, K. J. A.; Lin, S. W.; Pacifici, R. E. *J. Biol. Chem.* **1987**, *262*, 9914.

(63) Behrens, G.; Koltzenburg, G. *Z. Naturforschung* **1985**, *40c*, 785.

(64) Garrison, W. M. *Chem. Rev.* **1987**, *87*, 381.

(65) Hawkins, C. L.; Davies, M. J. *Biochim. Biophys. Acta* **2001**, *1504*, 196.

(66) Headlam, H. A.; Davies, M. J. *Free Rad. Biol. Med.* **2002**, *32*, 1171.

(67) Neta, P.; Huie, R. E.; Ross, A. B. *J. Phys. Chem. Ref. Data* **1990**, *19*, 413.

(68) Davies, M. J.; Fu, S.; Dean, R. T. *Biochem. J.* **1995**, *305*, 643.

(69) Kaptein, R.; Oosterhoff, L. J. *Chem. Phys. Lett.* **1969**, *4*, 195.

(70) Paul, H.; Fischer, H. *Z. Naturforschung, Teil A* **1970**, *25*, 443.

(71) Hawkins, C. L. *J. Chem. Soc., Perkin Trans. 2* **1998**, 2617.

(72) Kitaguchi, H.; Ohkubo, K.; Ogo, S.; Fukuzumi, S. *J. Am. Chem. Soc.* **2005**, *127*, 6605.

(73) Miyamoto, S.; Martinez, G. R.; Rettori, D.; Augusto, O.; Medeiros, M. H. G.; Di Mascio, P. *Proc. Nat. Acad. Sci.* **2005**, *103*, 293.

(74) Sevilla, M. D.; Becker, D.; Yan, M. *Int. J. Radiat. Biol.* **1990**, *57*, 65.

(75) Tarasov, V. F.; Forbes, M. D. E. *Spectrochimica Acta Part A* **2000**, *56*, 245.

(76) Shushin, A. I. *Chem. Phys. Lett.* **1995**, *245*, 183.

(77) Freed, J. H.; Pedersen, J. B. *Advan. Magn. Reson.* **1976**, *8*, 1.

(78) Turro, N. J.; Khudyakov, I. V. *J. Phys. Chem.* **1995**, *99*, 7654.

(79) Buckley, C. D.; Hunter, D. A.; Hore, P. J.; McLauchlan, K. A. *Chem. Phys. Lett.* **1987**, *135*, 307.

(80) Forbes, M. D. E.; Schulz, G. R.; Avdievich, N. I. *J. Am. Chem. Soc.* **1996**, *118*, 10652.

(81) Tarasov, V. F.; Ghatlia, N. D.; Buchachenko, A. L.; Turro, N. J. *J. Am. Chem. Soc.* **1992**, *114*, 9517.

(82) Noggle, J. Viscosity. In *Physical Chemistry*; HarperCollins: New York, 1996; pp. 480.

(83) Terazima, M. *Acc. Chem. Res.* **2000**, *33*, 687.

(84) Wong, M.; Thomas, J. K.; Gratzel, M. *J. Am. Chem. Soc.* **1976**, *98*, 2391.

(85) Pileni, M. P. Hydrated Electrons in Reverse Micelles. In *Structure and Reactivity in Reverse Micelles*; Pileni, M. P., Ed.; Elsevier Science Publishing: New York, **1989**; pp. 176.

(86) Adeleke, B. B.; Wan, J. K. S. *J. Chem. Soc., Faraday Trans. 1* **1976**, *72*, 1799.

(87) Kausche, T.; Sauberlich, J.; E., T.; Beckert, D. *Chemical Physics* **1996**, *208*, 375.

(88) Eicke, H.-F.; Kvitna, P. Reverse Micelles and Aqueous Microphases. In *Reverse Micelles: Biological and Technological Relevance of Amphilic Structures in Apolar Media*; Luisi, P. L., Straub, B. E., Eds.; Plenum Press: New York and London, **1984**.

(89) Johannson, K. P.; Marchetti, A. P.; McLendon, G. L. *J. Phys. Chem.* **1992**, *96*, 2873.

(90) Monnoyer, P.; Fonseca, A.; Nagy, J. B. *Colloids Surf. A* **1995**, *100*, 233.

(91) Xu, W.; Akins, D. L. *Materials Letters* **2004**, *58*, 2623.

(92) Maruyama, K.; Osuka, A. The Chemistry of Quinonoid Compounds; Patai, S., Rappoport, Z., Eds.; Wiley: London, **1988**; Vol. 2; pp. 760.

(93) Rontani, J.-F. *Trends in Photochemistry & Photobiology* **1997**, *4*, 125.

(94) White, R. C.; Tarasov, V. F.; Forbes, M. D. E. *Langmuir* **2005**, *21*.

(95) Harbron, E. J. M., Vanessa P.; Xu, Ruixin; Forbes, Malcolm D. E. *J. Am. Chem. Soc.* **2000**, *122*, 9182.

(96) Rao, D. N. R.; Rideout, J.; Symons, M. C. R. *J. Chem. Soc., Perkin Trans. 2* **1984**, 1221.

(97) Behar, D.; Fessenden, R. W.; Hornak, J. P. *Radiation and Physical Chemistry* **1982**, *20*, 267.

(98) Zubarev, V.; Goez, M. *Angewandte Chemie Int. Ed.* **2003**, *36*, 2664.

(99) Tarasov, V. F. *Spectrochim. Acta. A* **2006**, *63*, 776.

(100) Lu, J.-M.; Wu, L. M.; Geimer, J.; Beckert, D. *Phys. Chem. Chem. Phys* **2001**, *3*, 2053.

(101) Yashiro, H.; White, R. C.; Yurkovskaya, A. V.; Forbes, M. D. E. *J. Phys. Chem. A* **2005**, *109*, 5855.

(102) Silverstein, R. M.; Webster, F. X. *Spectrometric Identification of Organic Compounds*; John Wiley and Sons: New York, **1998**.

(103) Kaptein, R. Chemically Induced Dynamic Nuclear Polarization. Ph. D. Thesis, Leiden, **1971**.

(104) Salikhov, K. M.; Molin, Y. N.; Sagdeev, R. Z.; Buchachenko, A. L. *Spin Polarization and Magnetic Effects in Radical Reactions*; Elsevier: Amsterdam, 1984; Vol. 22.